JOURNAL OF
EMERGING INVESTIGATORS

VOLUME 4, ISSUE 2 | FEBRUARY 2021
emerginginvestigators.org

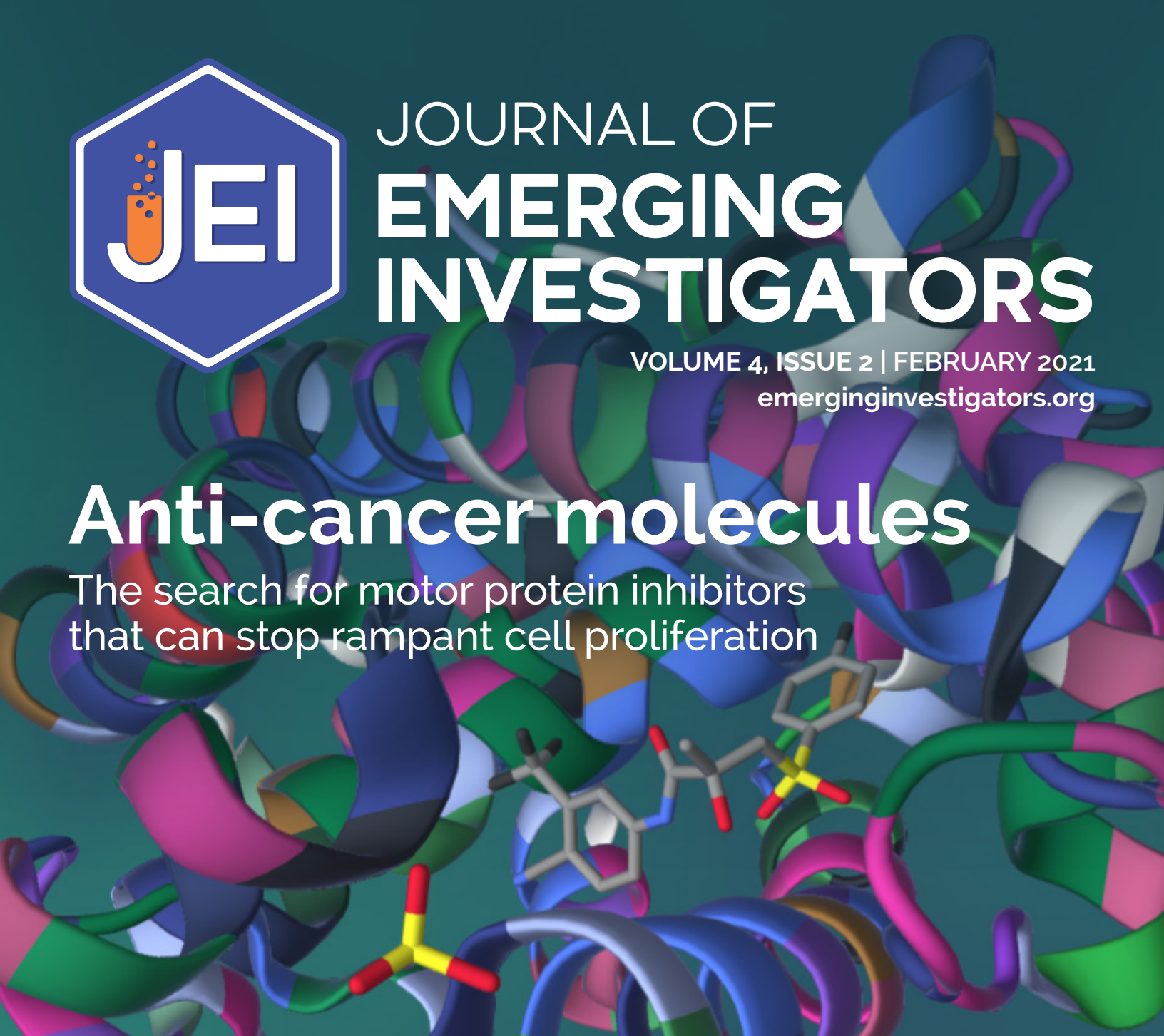

Anti-cancer molecules
The search for motor protein inhibitors that can stop rampant cell proliferation

Ultra-waterproofing
The development of a super-hydrophobic surface

Microplastics and marine life
How plastic pollution affects both fish and humans

Asteroid analysis
How gravity and temperature can affect an asteroid's orbit

A harmonic hypothesis
Examining the higher harmonics in an oscillating string

JOURNAL OF EMERGING INVESTIGATORS

The Journal of Emerging Investigators is an open-access journal that publishes original research in the biological and physical sciences that is written by middle and high school students. JEI provides students, under the guidance of a teacher or advisor, the opportunity to submit and gain feedback on original research and to publish their findings in a peer-reviewed scientific journal. Because grade-school students often lack access to formal research institutions, we expect that the work submitted by students may come from classroom-based projects, science fair projects, or other forms of mentor-supervised research.

JEI is a non-profit group run and operated by graduate students, postdoctoral fellows, and professors across the United States.

Contents

VOLUME 4, ISSUE 2 | FEBRUARY 2021

JOURNAL OF
EMERGING INVESTIGATORS

Article

Comparison of Perception of 2020 Election Security Threats Between Young and Old Voters

Thomas Rafacz[1] & Jason Campbell[1]
[1] Schaumburg High School, Schaumburg IL

SUMMARY

Elections constitute the bedrock of a democratically governed society. Due to the long time it has historically taken to ensure equal social participation, the integrity of elections needs to be particularly protected to make every vote count. The democratic process itself has been subject to manipulation through widespread illegal practices in many municipal areas like New York or Chicago that have earned in the past a notoriety for ballot stuffing or stealing votes through impersonation. In the current American social climate of the 2020 presidential election, the same concerns come up to the forefront, compounded by threats of cybersecurity. Our research gauged types and extent of concernment among two age groups of voters: college students and senior citizens. We explored the correlations using the baseline survey and re-examined them after applying information frames through a paired comparison. We found that opinions about voter ID laws and cybersecurity have a strong association to age. Our original hypothesis was that seniors will unchangeably perceive voter identification as essential to election safety while young people will emphasize cybersecurity but will be open-minded. Contrary to that hypothesis, seniors expressed an equal concern over voter ID and cybersecurity and seemed to be more susceptible to the influence of new information. Comparably, college students overwhelmingly confirmed their preoccupation with cybersecurity, marginalizing voter ID, but unexpectedly did not show inclination to easily change their views. The age of voters plays a role in how they perceive the concerns and how they react to information about them.

INTRODUCTION

According to the 2019 report from the Electoral Integrity Project (EIP) conducted by the Department of Government and International Relations, in the years 2012 to 2018, the United States scored 61 points on a 100-point scale of electoral integrity in the assessments of the cumulative study of 337 presidential and parliamentary elections in 166 countries around the world (1). The scale measures 49 core items in expert political surveys, discerning a moderate range (50-59), high (60-69), and very high (70+). Among global complex electoral concerns were inconsistent voter registration processes and vulnerability to cybersecurity attacks. While not fraudulent in essence, electoral laws and procedures, when manipulated, can lead to voter fraud, which is not a new phenomenon. Going back to 1982, a large-scale scheme was unveiled in the Chicago and Illinois general elections where 63 individuals were charged and convicted of tampering with registration, including forging signatures and impersonation (2). In the recent two decades, despite a low number of proven instances of voter fraud, only 1,088 cases nationwide since 2002 (3), the perception of fraud seemed to linger among American public, with a tendency to become subjectified. To illustrate, a study conducted in 2008 at Columbia Law School that involved a survey of a 36,500-person sample over a period of three years revealed that 41% of respondents held the belief of a high occurrence of fraud (4). In 2015, Sances and Stewart demonstrated the subjectivity of voter confidence through a strong pattern of voters reporting a high level of confidence (61%) in their own votes being counted as cast and a low level of trust (22%) in the accuracy of other voters' ballots (5). At the same time, this distrust seems to have recently fluctuated and diminished as reported by the Gallup Newspoll from September of 2019 in which 70% of the public expressed a comfortable level of confidence in the upcoming 2020 election's accuracy (6).

Attempting to understand the changing trends and impacts on this conflicting perception is crucial in taking steps to further increase voter confidence. The sources of concern over election integrity stem from two kinds of threats: historically founded voter fraud, mostly through impersonation (7), and a recent phenomenon of threat to cybersecurity (8). There were attempts to address the first problem through the introduction of voter ID laws that have become a highly contentious subject, opening the stage for some studies on their effectiveness, especially following a momentous challenge of these laws in *Crawford v. Marion County Election Board* case in 2008 (9). After the 2013 Supreme Court decision to strike down Justice Department oversight of state election procedures, thirty-four states responded by introducing varying degrees of voter identification requirements (7). Public discourse demonstrates that opinion on voter ID laws is very divided: either they are a valuable tool for preventing voter fraud and assuring public confidence or they are a tool for disenfranchising voters. The existing research therefore has focused on examining the relationships between the laws and election turnout as well as public support for them based on rates of access to IDs by social groups. For example, a study conducted in Texas in

2011 found that 4.5% of their registered voters lacked proper identification (10). At the same time, the 2014 survey among New Mexico voters with a large Hispanic population who bear the brunt of the laws concluded that 51% of them do not see the laws as a barrier to voting and 70% accept them as a safeguard against fraud (11).

Along with the implementation of voter ID laws, American society has become increasingly dependent on technology such as electronic voting and automated voter registration systems. The breach of the electronic books in North Carolina, Florida, and Illinois by Russian government agents in 2016 (12) raised the possibility of votes being altered and thus compounded a threat to public confidence in the 2020 election results. In contrast to many known studies on the effects of voter ID laws, the existing literature on the subject of cybersecurity is scarce due to it being a relatively new domain. However, this seems to emphasize the inadequate communication of threats to public and state election officials. In a report prepared by the Cyber Law Program at the Hebrew University in Jerusalem, the findings point to secrecy in American cyber policies that tend to be limited to solely detecting and containing security breaches (13). Consequently, public knowledge of the attacks is limited to what is leaked to the press, which is enshrouded in sensationalism. For example, according to one account published in the *Washington Post* in June 2019, twenty-one states were targeted by the Russian agents in 2016 (12) while its July publication included the Senate panel's report alleging all fifty states becoming the subject of interference (14).

Most information about cybersecurity comes from government and corporate reports that assess states' preparedness for the 2020 election in an effort to substantiate federal funding for security upgrades. The most comprehensive report concerning levels of vulnerability in all fifty states was prepared by the Center for American Progress in cooperation with the U.S. Election Assistance Commission and top election officials. Based on their assessment of a given state's compliance with baseline security standards mandated by federal regulations, the authors found that five states are failing the expectations, twelve receive a "D" grade, and twenty-three states rate at a "C", which poses high risks for cyberattacks (15). Moreover, similar reports analyzing the threats to the voting process that have been prepared by the Brennan Center for Justice (BCJ) focus predominantly on electronic vulnerabilities such as outdated machines susceptible to hacking, states' use of electronic touch screen machines without a verifiable paper trail, or the scarcity of post-election paper audits (16).

These findings are crucial in leading to our research. In our study, we aimed to determine how many voters are aware of the vulnerability of electronic voting infrastructures to foreign interference compared with how many just express a basic concern about the identity of voters. The goal of our study was to examine which threat is more significant to the public, physical impersonation or compromised cybersecurity, and subsequently, if the perception concerning the type of threat tends to align with a respondent's age. We posed a hypothesis that senior voters will focus on voter ID while students will latch onto cybersecurity. Besides gauging the correlation between voters' ages and the perceived security threat, we were also interested in the impact of information on shaping that perception. In a 2014 New Mexico survey (11), depending on how the questions were framed, the respondents valued ensuring access more than prevention of fraud, a finding that was later corroborated by a 2016 study that demonstrated that information campaigns and their framing have a significant influence on public perception of the laws. It concluded that when the manipulated words in questions emphasized a possible harm to African-Americans or the elderly, public support for the laws decreased from 79 to 61% (17).

The implication of this finding was significant in the formulation of our second hypothesis concerning "open-mindedness": We wanted to find out if increased public knowledge about types of threats leads to a changed perception of election security between young and old registered voters. In other words, extrapolating from our original hypothesis proposing that the older generation might be inclined to be concerned about ID laws while the younger generation growing up with a constant presence of technology might perceive existing vulnerabilities in cybersecurity, our research aimed to address if each generation is locked into a discernible way of thinking or open to acquiring new information and modifying the existing beliefs about them. Using a baseline survey to correlate age and a type of concern and then examining the impact of information frames through a paired comparison, our study confirmed that a strong positive association existed between age and concern about meeting proper identification standards at the polls and a strong negative association between age and cybersecurity concerns, even though seniors expressed an equally strong worry about electronic voting. We could not obtain validation for an influence of information on both age groups. We could only infer that the small margin of 10% out of 102 seniors seemed to be impacted by information framing.

RESULTS

Base Survey

Paper surveys were distributed to senior respondents (over the age of 70) and college students (ages 18 to 22) to determine generational differences in types of election security concerns and preferences. The questionnaire consisted of six questions. The first three questions collected demographic information such as voter registration status, gender, and political affiliation. The remaining three questions asked respectively how concerned a respondent was about voters meeting identification standards at the poll (People who vote are the people who they say they are), how concerned a respondent was about security of electronic machines when casting a vote (A vote will not be altered), and which is a greater threat to the 2020 election between identity fraud

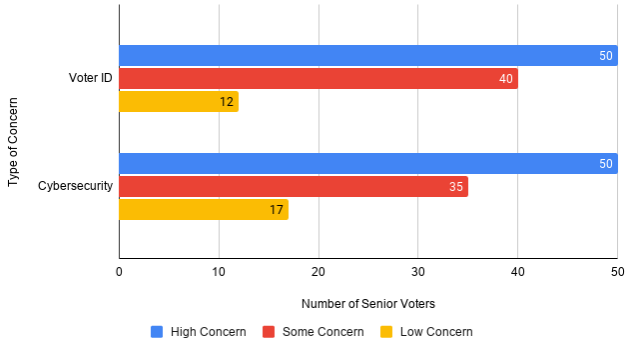

Figure 1: Comparison of Results for Election Concern Types in the Base Survey Among Senior Voters. Seniors (N = 102) expressed equally high concern over voter ID and cybersecurity.

(bloated registration lists or impersonation) and cyberattacks on the electronic systems. The former two questions included three options in responses: high, some, and low concern. The senior respondents included 71 females and 31 males. Among college students who participated in the study, 53 were females and 45 were males. Two students chose not to disclose their preference for gender. Data sets revealed a strong positive association between age and perception of high concern for the voter ID standards. In a chi-squared test, the relation between the variables of age and high and low concern for voter ID was significant, $X^2(1, N=109)= 16.8819$, $p = 0.00004$. Significant at $p < 0.05$. One in five young people (20%) expressed high concern while that number rose to 50% among older subjects. Likewise, a strong negative association was found between "low concern" for voter ID and age. Only 12% of older respondents thought that voter ID concern was insignificant whereas over double that number (27%) of young people dismissed the problem (**Figures 1 & 2**). There was no association found between the "some concern" answer for voter ID and age because a smaller difference existed between both age groups. Half of the young respondents (53%) expressed "some concern" compared with 40% of the seniors in the same category (**Figures 1 & 2**). The chi-squared relationship between age and "some" levels of concern was not significant, $X^2(1, N= 132)= 1.7246$, $p = 0.189097$. Not significant at $p < 0.05$. Of those seniors who thought that voter

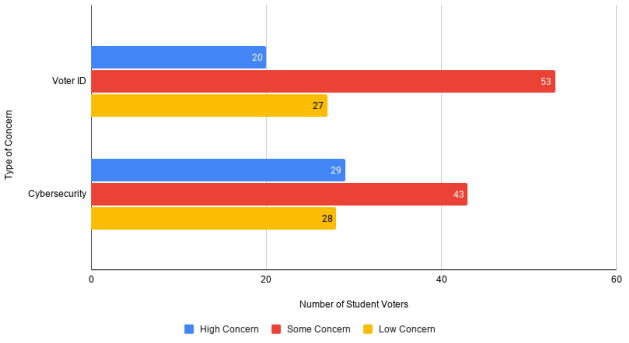

Figure 2: Comparison of Results for Election Concern Types in the Base Survey Among College Students. Only about half as many students (N = 100) as seniors (N = 102) had high concerns, overall keeping low levels of concerns over both threats.

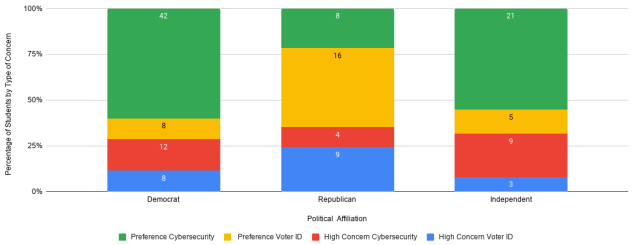

FIgure 3: Comparison of Perception of Election Threats Among College Students Given Political Affiliations. 77.1% of college students who either expressed the preference for cybersecurity as a bigger threat or were highly concerned about it were Democrats.

ID was of "high concern", 43% were Democrats and 53% were Republicans. In parallel, only 16% of young Democrats and twice as many Republicans (37%) viewed voter ID as a "high concern" (**Figure 3**).

Data sets with respect to "high concern" for cybersecurity pointed to a strong positive association between the responses and age: 29% of young respondents expressed high concern and the number rose to 50% in the older population (**Figures 1 & 2**). In a chi-squared test, the relation between the variables of age and concern for cybersecurity was significant, $X^2(1, N=124) = 7.5136$, $p = 0.006124$. Significant at $p < 0.05$. Our research revealed that older people expressed equally high concern for both voter ID and cybersecurity. There was a strong negative association between age and "low concern" for cybersecurity, with a decrease from 28% in young people to 17% in the older population (**Figures 1 & 2**). No association was found between age and "some concern" for cybersecurity: 43% of young students gave a neutral answer and this number decreased to 35% among seniors. The chi-squared relationship between age and "some" levels of concern was not significant, $X^2(1, N= 132) = 0.5885$, $p = 0.443006$. Not significant at $p < 0.05$. When comparing the values for the "some concern" category across voter ID and cybersecurity among old people, the difference of 5% was minimal (40% of "some concern" for voter ID and 35% of "some concern" for cybersecurity), indicating that about the same percentage did not care about both (**Figure 1**). When comparing "low concern" for voter ID and cybersecurity in young people, the numbers were almost equal: 27% for ID and 28% for cybersecurity (**Figure 2**). Similarly, the low percentage for "low concern" among old people was closely dispersed between 12% for voter ID and 17% for cybersecurity.

Young people typically did not express high concerns about cybersecurity: only three in ten (29%). The highest number (43%) was for those expressing "some concern" or the neutral position about cybersecurity. The same trend could be observed in the college students' responses of "high" and "low concern" for voter ID, with 20% and 27% respectively, and the middle answer ("some concern") taking up the highest percentage of 53% (**Figure 2**). This is, however, different for the old-age group which clearly displayed a disproportion between the "high concern" answer of 50% for voter ID and its "low concern" of 12%. Likewise, five in ten

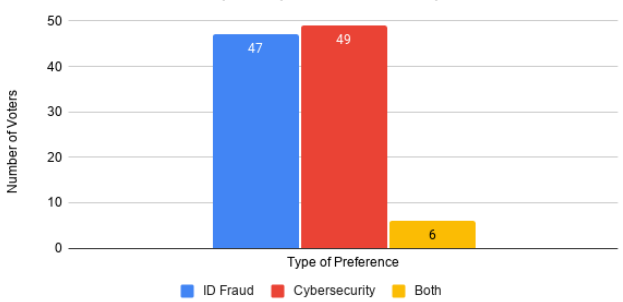

Figure 4: Comparison of Type of Election Security Preference in the Base Survey Among Senior Voters (N = 102). Almost 50% of the seniors kept their preference for the importance of cybersecurity.

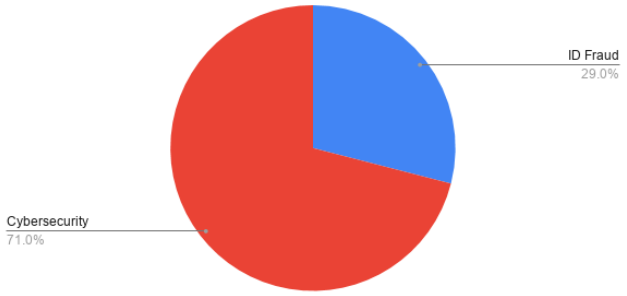

Figure 5: Comparison of Type of Election Security Preference in the Base Survey Among College Students. 71% of young voters chose cybersecurity as their primary election concern.

older respondents chose ”high concern” for cybersecurity and only 17% selected “low concern” (**Figure 1**). In theory, higher concern about voter ID fraud should correlate with a perception that voter ID fraud is a greater threat than cybersecurity (as measured in the base survey); however, no such association was found. The chi-squared relation between these survey answers was not significant, $X^2(1, N= 146) = 1.5018$, $p = 0.220394$. Not significant at $p < 0.05$. Older people were quite consistent, only slightly leaning towards cybersecurity (48%) and retaining their support for voter ID at 46% (**Figure 4**). In contrast, the majority of young people (71%) were leaning towards cybersecurity as opposed to 29% choosing earlier voter ID as a high concern (**Figure 5**). The correlation between age and choice for cybersecurity was significant, $X^2(1, N= 199) = 9.6018$, $p = 0.001934$. Significant at $p < 0.05$.

Paired Comparison Survey

The second phase of paper surveys was distributed to the same groups of respondents. It was meant to measure the impact of information framing on their perceptions of the same two election threats, voter identification and cybersecurity. Each respondent was asked to read a side-by-side short comparison of the alarming incidents, procedures, or regulations that had recently opened the ID laws and electronic voting to abuse. Then, the subjects were asked to rate on a scale of one to nine which of the two security vulnerabilities they would prefer to be addressed in the 2020 election. Three in ten seniors (30%) recorded strong (9 on the scale) concern for cybersecurity while 31% reported equal (5) concern for cybersecurity and voter ID standards (**Figure 6**). There were nine senior responses (1 on the scale) of strong concern about voter ID standards. Twenty-seven percent of young people chose a value of 5, indicating equal concern for both issues, while 7% still perceived voter ID as the strong concern (1), for a total of 34%—still a 5% increase from the original 29% (**Figure 7**). Young people’s concern for cyberattacks seemed to be now more dispersed on the scale, with 12% perceiving it as strong (9), 6% choosing a value of 8, 23% opting for 7 on the scale, and 13% for a value of 6. We performed two-tailed tests for the differences in the ratings between seniors and students: one for voter ID and one for cybersecurity. H_o: Mean (u) = 0 (No difference) H_a: Mean (u) does not equal 0 (Two-tailed). For voter ID, there was no statistically significant evidence to support the claim that the seniors’ answers were different from students’, $t = 1.1209$, $p = 0.3251$. The same was true about the test for cybersecurity: $t = -0.1589$, $p = 0.8839$ at $p < 0.05$.

DISCUSSION

The aim of our research was to determine if there was an association between older age and concern about voter ID fraud as well as between younger age and cybersecurity. Additionally, we wanted to find out if there was a significant difference between both age groups and their reaction to new information about these threats.

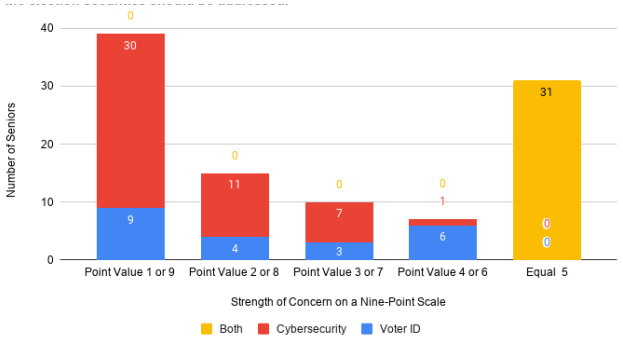

Figure 6: Results of Preference for Security Vulnerability Among Seniors (N = 102) in a Paired Comparison Survey. Given side-by-side information, almost 40% of seniors strongly felt that the election securities should be addressed.

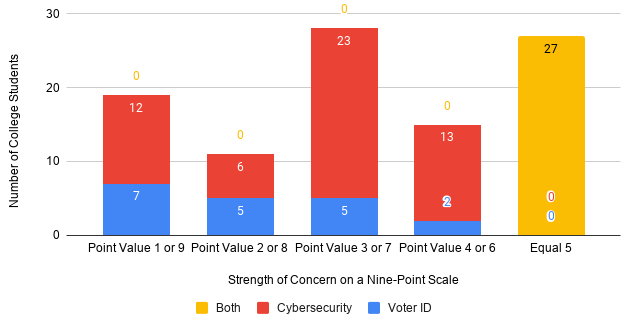

Figure 7: Results of Preference for Security Vulnerability Among Students (N = 100) in a Paired Comparison Survey. The distribution of concerns was more evenly dispersed, with less than 20% of students expressing strong feelings.

Phase One

Data sets on the base survey showed an overall lower rate of "high concern" for voter ID and cybersecurity in young people when compared with seniors. The older generation came out equally troubled by both concerns. Senior citizens tended to be more concerned and worrisome in general. Since Krosnick (18) suggests that the "some concern" answer" reflects neutrality, the drop in percentage with age for that type of answer might indicate more crystallized fears and worries about the electoral process among older people. The findings for the young group were consistent with our original hypothesis: the young generation predominantly expressed concern about cybersecurity even though the "high concern" answer gauging the level of worry about security of electronic machines when casting a vote did not exactly match their preference of "cyberattacks on the electronic systems" when asked to choose a greater threat. However, the discrepancies between overall concerns and preferences are not entirely surprising. According to a study conducted by Ansolabehere *et al*., what the public professes is not a reliable source of determination about the actual public concern. For example, in his study of the election turnout contingent upon beliefs about the frequency of voter fraud, he found that there was no significant difference in the number of validated votes in the 2006 general election between those who believed that fraud is a "very common" occurrence and those who reported fraud to be "infrequent" (4).

The lower numbers of Democrats in both age groups who expressed "high concern" about voter ID fraud were consistent with the partisan difference concerning the support for voter ID laws found in earlier studies which concluded that citizens support or oppose the ID laws based on their party loyalty, with Republicans increasing their support for the laws if there is even a "minuscule amount of in-person voter fraud" (19). We found that 16% of Republicans and 24% of Democrats chose the "high concern" option in response to the question about cybersecurity (**Figure 3**). We also noticed a similar frequency of partisan concern about cybersecurity among old voters: 56% of Democrats and only 32% of Republicans saw it as a "high concern". While a political party was not a focus of our research, we decided to collect the data on party affiliation to observe if Democrats, regardless of age, are more concerned about cybersecurity than Republicans in our results.

Phase Two

Another finding was that the information framing had no effect on either of the age groups. The choice of scaled paired comparison as an optimal design came from our intention to make response options exhaustive and yet mutually exclusive. Therefore, we chose a dichotomy to allow for the reporting of extreme attitudes and still be able to select a midpoint with a neutral attitude. Its simplicity and ease of administration in a short period of time were also our considerations. After reading information about voter identification and cybersecurity, the group of seniors seemed to be more impacted by them than the young respondents. While 30% of concern for cybersecurity seems lower than the original 50%, a closer analysis might reveal a different conclusion. To clarify, even though the original design of the nine-point scale suggested the midpoint to be neutral, by observing the reactions of the participants and inferring from their clarifying questions, it is more plausible to consider a score of 5 (Equal) on the scale as the indicator of equally strong concern for both types of threats. Therefore, when combined, both responses for cyber concern were at 61% while merging strong concern for voter ID (9 responses that chose 1) with 31 responses with the middle value of 5 yielded 41% of high concern for voter ID among seniors. Overall, the information shifted the perception by about 10% on both sides, lowering the concern for voter ID by about 10% and increasing the concern for cybersecurity by 10%. When using a single sample t-test, this conclusion is significant for the population mean (u)=50, $t(102) = -4.3203$, at $p < 0.05$. Now, looking at the raw data of high concern responses about voter ID and cybersecurity, 9 and 30 respectively, there was no significant effect for age when performing two-tailed tests for the differences in the ratings.

When it comes to college students, information framing seemed to have an even less discernible impact. The information did not change their opinion about voter ID. Considering that originally 71% of young people chose the preference for cybersecurity, that 39% chose the strong preference in this phase (27% of responses consisted of 5 and 12% of 9) constituted a big drop. This might indicate that they were considering the received information and it decreased the strength of their perception, but a different explanation is also plausible. Since the frames did not shift their preference towards voter ID, it is also possible that the information had little impact in view of the fact that in the first survey, the participants only had a choice between voter ID and cybersecurity while the scale allowed for different degrees of concern, thus better reflecting subtleties in perception in the first place. Overall, the findings did not seem to support our second hypothesis that young people's perceptions have higher susceptibility to the impact of information. There are a few explanations for such results. Firstly, a major confounder that has become more prevalent recently are misinformation campaigns and the rise of "alternative facts" or "fake news." Even though we cited information from credible sources, it was difficult to earn enough trust from the respondents for them to be willing to accept new information. Secondly, the Stanford study from 2016 already established that the passage of strict voter ID laws made a marginal difference in the voters' knowledge about their existence (5). When asked about their states' legal voting requirements, 68% of the American public in nineteen states that lacked them in 2015 nevertheless reported either absence of knowledge or a misguided belief about the required documentation (5). This seemed to be particularly true for the younger generation.

Limitations and Implications

The small sample of respondents posed the largest limitation. Additionally, in order to measure an actual significant change in the views of both age groups, a repeated longitudinal study is needed. Due to the convenience of administering the surveys at nursing homes that aggregate senior citizens, the respondents' age tended to be on average over 70 years. To increase reliability of the results, future surveys could use a more diverse and larger sample, ideally with some smaller gradation of age (a decade or two). To enhance the research and even potentially point it to a new direction of psychological study, additional questions could be added to the surveys. In her book *Political Persuasion and Attitude Change*, Diana Mutz, Professor at Stanford University, argues that "there is tremendous variability from one election to another, from one kind of issue to another, and from one social environment to another" (20). Thus, repeating the study for another election, identifying the influence of mass media, preferences for political elites, or even personality traits of the participants can play a role in determining the impact of information.

Still another limitation of the study was the unforeseen gender imbalance. Three times more females than males participated in the senior sample. Moreover, 79 college students who participated in the study were enrolled in a Political Science class, which could potentially create a bias since they already had some knowledge about the topic. Despite inherent limitations, polls and surveys seem to dominate our news and inform politicians about the public perceptions that later drive local and state decisions. For example, voter ID laws were first justified in 2000 by Republican-led majority elections in Georgia and Indiana by the widespread public concern about voter fraud (21). Moreover, states often cite public interest as sufficient to implement such laws (22). Similarly, with the widespread concern about cybersecurity among voters of all ages, a public-private partnership to administer elections or even ceding their control to an impartial judiciary rather than politicians (23) may merit more attention in the future.

MATERIALS AND METHODS

The study design was conducted in two contiguous phases that received IRB approval from my school. In order to establish an association between age and perceived election security threat, quantitative data was first collected from a survey administered to two groups, one consisting of 102 senior citizens and the other of 100 college students. The first selected sample included a heterogenous group of 79 students at a community college who were enrolled in five sections of Political Science 101 meeting face-to-face. A further sample was drawn from 21 randomly selected students on the same college campus. The survey was distributed during an in-person class and administered by the faculty with the permission of their Director for Institutional Research. Participation was voluntary and the students were invited to partake in a study about the upcoming election. The completed surveys were anonymously placed in an envelope. The other sample of senior respondents was collected at three retirement homes in the north-west suburbs of Chicago with the help of the activities coordinators who advertised the event in the local bulletin and permitted us to set up the tables on site during specific times in late December 2019 and January 2020. The reason for choosing three different settings was related to the availability of the respondents as participation was anonymous and voluntary. The three venues included a wide representation of socio-economic status of the respondents, from affluent residents living on site to non-residents who come for social interaction and community outreach programs.

Base Survey

The first survey measured perceptions of three issues related to potential 2020 election security threats: voter ID fraud, cybersecurity breaches, and which of these two should be addressed. The demographic variables that were collected included gender and political affiliation. The survey design used the scale of bipolar construct described by Krosnick (18) that consists of two opposing alternatives (slight and substantial) and a midpoint (moderate) with regard to concerns framed as two questions: "How concerned are you about voters meeting identification standards at the polls?" and "How concerned are you about the security of electronic machines when casting a vote?" Krosnick recommends using a bipolar construct for measurement of public attitudes arguing that a choice of a neutral midpoint tends to represent the status quo, the respondent's agreement with the existing state of affairs, thus yielding a collection of additional useful data. To improve data quality, the survey included verbal labeling of answer choices. The third question on the survey directly asked for the respondent's perception of a greater threat phrased as a choice between inaccurate identification or cyberattacks (**Figures 4 & 5**). Establishing this correlation was meant to test the proposed hypothesis that older voters might be more concerned about ID laws while younger respondents who are more accustomed to technology tend to be preoccupied with cybersecurity. The associations between age of the two groups (seniors and students) and levels of cybersecurity concerns as well as levels of voter identification concerns were assessed using a chi-squared test.

Paired Comparison Survey

The second questionnaire in the design approach involved the quasi-experimental study aimed to examine the effectiveness of information in changing the perception of election security threat. It involved the same two samples of young and old voters. The second questionnaire used a design which was based on a paired comparison of two types of threats, voter ID and cybersecurity, modeled on the original experiment conducted by Magat who assessed values attached by consumers to risks associated with commercial chemical products (24). In our design, two informational

frames that pointed to current risks and vulnerabilities involved in the potential breach of the integrity of the 2020 election were posted side-by-side. Particular attention was given to a balanced length and wording between both concerns and strong wording such as "fraud" or "breach" was used. The following question was posed at the bottom of the survey, "Which security vulnerability would you prefer to be addressed in the 2020 election?" Respondents rated their preference on a nine-point scale where 1 is for "strongly concerned for voter ID", 9 is "strongly concerned for cybersecurity", and 5 represented indifference between them in order to test if the provided information had an influence on their perception of threats. A multi-point rating scale allows for a more precise detection of subtle differences in perception and attitudes (18). The scale of a paired comparison has been originally pioneered by Thurstone who argued that by removing verbal description in judgement, the subject can discriminate between given values with a reliability equal to discriminating between physical objects (25). Applying this design was meant to help investigate a concurrent hypothesis that older voters might be less susceptible to the influence of information and more set in their ways of thinking. The results of the second survey were then compared with the correlational data obtained through the first survey for both groups. Hypotheses about the impact were then statistically assessed through a two-tailed t-test for the differences in the ratings for voter ID and cybersecurity between seniors and students, using TI-84 Plus graphing calculator. The null hypothesis was that the Mean Difference = 0.

Received: August 6, 2020
Accepted: November 13, 2020
Published: January 5, 2021

REFERENCES

1. Norris, Pippa and Max Gromping. "Electoral Integrity Worldwide." Electoral Integrity Project, May 2019, University of Sydney, www.electoralintegrityproject.com Accessed 20 Aug. 2019.
2. Berry, Mary Frances. Five Dollars and a Pork Chop Sandwich: Vote Buying and the Corruption of Democracy. Beacon Press, 2017.
3. "Election Fraud Cases." The Heritage Foundation, 2019, www.heritage.org/voterfraud/search?state=IL&combine=&year=&case_type=All&fraud_type=All&page=2.
4. Ansolabehere, Stephen, and Nathaniel Persily. "Vote Fraud in the Eye of the Beholder: The Role of Public Opinion in the Challenge to Voter Identification Requirements," *Harvard Law Review.* vol.121, no.7, 2008, pp.1738-1774. EBSCOhost, searchebscohost.com
5. Stewart, Charles, III, *et al*. "Revising Public Opinion on Voter Identification and Voter Fraud in an Era of Increasing Partisan Polarization." *Stanford Law Review*, June 2016, p. 1455+. Gale in Context: High School, Accessed 22 Aug. 2019.
6. McCarthy, Justin. "Most Americans Confident in Accuracy of Upcoming Elections." Gallup.com, Gallup, 4 Sept. 2019.
7. Price, Tom. "Election Security and Voting Rights." *CQ Researcher*, 12 Oct. 2018, Vol. 28, no.36. pp.851-871. www.cqresearcher.com. CQPress. Accessed 5 Oct. 2019.
8. Rush, Jacob. "Hacking the Right to Vote." *Virginia Law Review Association*, 18 Feb. 2019, www.virginialawreview.org/volumes/content/hacking-right-vote#_ftnref58.
9. Barreto, Matt A., *et al*. "The Disproportionate Impact of Photo Identification Requirements on the Indiana Electorate." Conference Papers -- American Political Science Association, 2008 Annual Meeting 2008, pp. 1–32. EBSCOhost.
10. Ansolabehere, Stephen, and Eitan D. Hersh. "ADGN: An Algorithm for Record Linkage Using Address, Date of Birth, Gender, and Name." *Statistics and Public Policy*, vol. 4, no. 1, 2017, pp. 1–10., doi:10.1080/2330443x.2017.1389620\
11. Atkeson, Lonna Rae, *et al* "Balancing Fraud Prevention and Electoral Participating: Attitudes Toward Voter Identification." *Social Science Quarterly* (Wiley-Blackwell), vol. 95, no.5, Dec. 2014, pp. 1381-1398. EBSCOhost, search.ebscohost.com
12. "Federal Investigators to Examine Equipment from 2016 N.C. Election Amid Renewed Fears of Russian Hacking." washingtonpost.com, 5 June 2019. Gale in Context: Opposing Viewpoints, http://link.gale.com/apps Accessed 12 Sept. 2019.
13. Efrony, Dan, and Yuval Shany. "A Rule Book on the Shelf? Tallinn Manual 2.0 on Cyberoperations and Subsequent State Practice." *American Journal of International Law*, vol. 112, no. 4, Oct. 2018, pp. 583–657. EBSCOhost, doi:10.1017/ajil.2018.86.
14. Demirjian, Karoun & Colby Itkowitz. "Russians probably targeted election systems in all 50 states, Senate panel's report says." *The Washington Post*. 30 July 2019. WP Company. 02 Oct. 2019.
15. Root, Danielle, *et al*. "Election Security in All 50 States." Center for American Progress, 12 Feb. 2018, www.americanprogress.org/issues/democracy/reports/2018/02/12/446336/election-security-50-states/.
16. Weiser, Wendy, and Max Feldman. "The State of Voting 2018: Brennan Center for Justice." The State of Voting 2018 | Brennan Center for Justice, 5 June 2018, www.brennancenter.org/publication/state-voting-2018.
17. Wilson, David C., and Paul R. Brewer. "Do Frames Emphasizing Harm to Age and Racial-Ethnic Groups Reduce Support for Voter ID Laws?" *Social Science Quarterly* (Wiley-Blackwell), vol.97, no.2, June 2016, pp.391-406 EBSCOhost, doi:10.1111/ssqu.12234.
18. Krosnick, Jon A., and Leandre R. Fabrigar. "Designing Rating Scales for Effective Measurement in Surveys." Survey Measurement and Process Quality, by John

Wiley, Wiley, 1997, pp. 141–159.
19. Kane, John V. "Why Can't We Agree on ID? Partisanship of Fraud, and Public Support for Voter Identification Laws." *Public Opinion Quarterly*, vol. 81, no. 4, Winter 2017, pp. 943-955.
20. "Political Persuasion: The Birth of a Field of Study." Political Persuasion and Attitude Change, edited by Diana C. Mutz, Paul M. Sniderman, Richard A. Brody, University of Michigan Press, 2007, pp. 1–10.
21. Parker, Keith P., *et al*. "Using Microaggression Theory to Examine U.S. Voter Suppression Tactics." *Negro Educational Review*, vol.69, no. 1-4, Jan.2018, pp.101-123.
22. Gilbert, Michael D. "The Problem of Voter Fraud." *Columbia Law Review*, vol.115, no.3, Apr.2015,pp.739-775.
23. "Talking Policy: Pippa Norris on Electoral Integrity." World Policy. April 21, 2017, tinyurl.com/yc6u58q4.
24. Magat, Wesley A, *et al*. "Paired Comparison and Contingent Valuation Approaches to Morbidity Risk Valuation." *Journal of Environmental Economics and Management*, vol. 15, no. 4, 1988, pp. 395–411.,doi:10.1016/0095-0696(88) 900
25. Thurstone, Louis L. "The Measurement of Value." *Psychological Review* 61 (1954): 47 - 58.

JOURNAL OF
EMERGING INVESTIGATORS

Article

The Development of a Superhydrophobic Surface Using Electrolytic Deposition & Polymer Chains Precipitation

Heeyun Kim*[1], Katelyn Woo*[1], MacRae Maxfield[1]
[1] Brooklyn Technical High School, Brooklyn, NY
* Equal contribution was made during this research

SUMMARY

The useful life of infrastructure metals is limited by prolonged exposure to water and deposition of insoluble minerals. Advances in surface treatment suggest that both problems can be alleviated through the formation of surfaces that are hydrophobic and therefore self-cleaning. In nature, the surface of a lotus leaf displays superhydrophobicity, containing microbumps on the surface with non-polar nanofibers on the bumps. Here, we describe a process that mimics this topography. The process includes brief electrodeposition of zinc from aqueous $Zn(NO_3)_2$ followed by drying and spray-coating of a xylene silicone solution. Our results indicate that zinc coated steel has a contact angle of 130° and a sliding angle of 16°, displaying it has high hydrophobicity and self-cleaning properties. Copper yielded similar results, indicating that this method can be applied to other metals. These results suggest that a Cassie-Baxter state, the ideal droplet to surface interaction, was formed on these metal surfaces. However, further development should be done regarding the precipitation of nanofibers to maintain the created topography. Such hydrophobic surfaces would improve the longevity of metal infrastructure since its anti-rusting characteristics limits the surface's exposure to water.

INTRODUCTION

In this era, there are many complications regarding infrastructure. This includes the maintenance of pipes and scaffolding. Within 20 years of construction, mineral deposits collect in a pipe system, preventing water flow through the pipes efficiently (1) and result in frequent cleansing or replacements of pipes. Another problem is the maintenance of scaffolding. During construction projects, scaffolding is exposed to water which leads to corrosion. However, a durable, self-cleaning surface can reduce the deposits in pipes (2) and corrosion of scaffolding (3).

Hydrophobicity is defined as the surface's chemical and physical ability to repel water. There are two measurements that quantify the surface's hydrophobicity: contact angle and sliding angle of water droplets (13). The contact angle is the angle between the tangent line of the water droplet to the surface (**Figure 1A**). The sliding angle is the angle of the surface in which the water droplet begins to roll off (**Figure 1B**) (13, 14). The higher the contact angle and the lower the sliding angle, the more hydrophobic the surface is. For example, the surface with contact angle of > 90° and sliding angle of < 45° is classified as hydrophobic, and the surface with contact angle of > 150° and sliding angle of < 10° is classified as superhydrophobic (13).

In nature, lotus leaves have superhydrophobic properties where their contact angles are greater than 150° and sliding angles are less than 5° (13). Since sliding and contact angles do not depend on each other, measuring both is needed to successfully determine the hydrophobicity of a surface.

Superhydrophobicity of a lotus leaf has been attributed to its microbumps on the surface of the leaf and the nanofibers coating the microbumps with dimensions of 10–15 μm apart, 5–10 μm in height, and 5 μm in diameter (17). These components enable the lotus leaf to achieve a Cassie-Baxter State rather than a Wenzel State (**Figure 2**). In the Cassie-Baxter State, the water droplet sits only on the tips of the bumps, creating a layer of air between the surface and the water droplet (13, 18). In the Wenzel State, the water droplet seeps through the crevices of the surface, wetting the whole surface area (16, 18).

The Cassie-Baxter state is achieved in lotus leaves not only by the size and space of the microbumps, but also by its nanofibers- the outermost fibers that create low surface energy. Surface energy is the amount of energy that attracts a liquid to its solid surface (**Figure 3**). If the attraction from

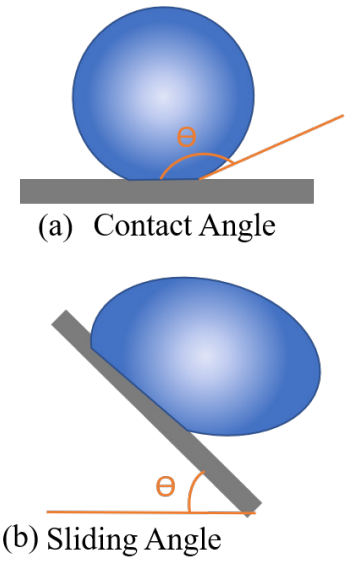

Figure 1: Illustration of water droplets (blue circle) on a surface (grey rectangle). The top orange angle represents the contact angle (the angle between the tangent line of the water droplet to the surface) and the bottom orange angle represents the sliding angle (the angle of the surface in which the water droplet begins to roll off). The higher the contact angle and lower the sliding angle, the more hydrophobic the surface is.

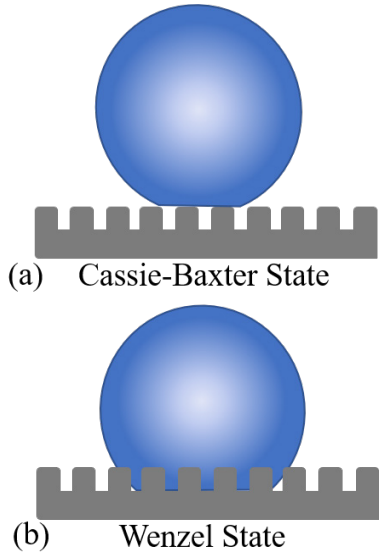

Figure 2: Diagram comparing water droplets in the Cassie-Baxter state and Wenzel state respectively. In the Cassie Baxter state, the water droplet sits on top of the microbumps, making the surface more hydrophobic than the Wenzel state where the water droplet encompasses the whole surface area.

the surface to the water droplet is less than the inward force of surface tension to the water, the water droplet will tend to keep a spherical shape, creating a high contact angle. When a surface has lower surface energy, the surface is considered more hydrophobic. This is summarized in Young's Equation, which shows the relationship between surface energy, surface tension of the water, and the water's contact angle (**Figure 4**) (13, 15, 16).

We hypothesized that hydrophobicity can be imparted on industrial metal surfaces including zinc and copper by electrodeposition (**Figure 5**) and can be further enhanced through the precipitation of hydrophobic polymer chains (**Figures 6 & 7**). Due to zinc and copper's various uses in the industrial market, we examined the different electrodeposition conditions of zinc on zinc and copper on copper sheets with and without a silicone coating and evaluated the resulting metals through their contact angle and sliding angles at room temperature. From our results, electrodeposition alone achieved a contact angle of 129° and a sliding angle of 23°.

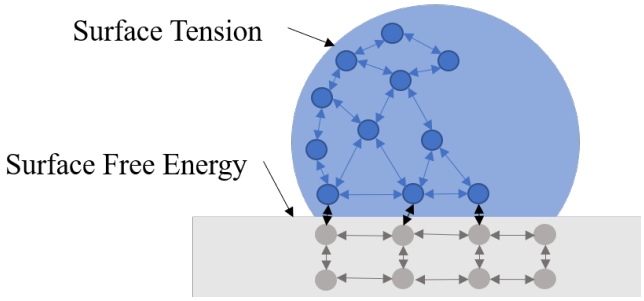

Figure 3: Illustration of intermolecular forces of a water droplet to its surface. Water molecules (dark blue circles) are held together through hydrogen bonding, creating surface tension. When surface tension is much greater than surface free energy, the water molecule displays a round shape that makes the surface hydrophobic. Surface free energy provides a quantitative measure to the intermolecular strength.

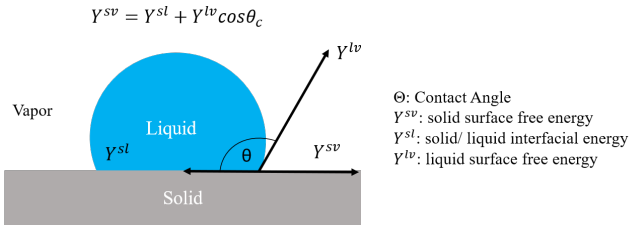

Figure 4: Young's Equation explains the attraction between the water droplets to its surface and surroundings. Young's Equation can be used to derive the contact angle of the droplet. .

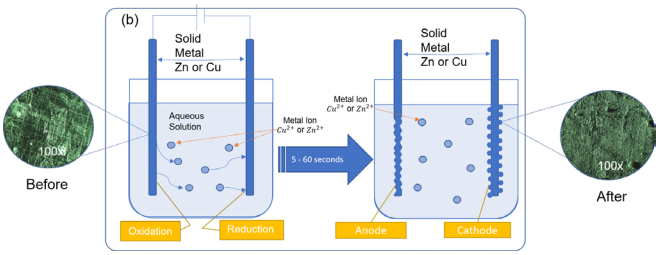

Figure 5: Illustration of electroplated microparticles (zinc or copper) on a metal surface (zinc or copper). For zinc surfaces, $Zn(NO_3)_2$(aq) was used to develop the zinc microbumps on the zinc surface. Likewise, $CuSO_4$(aq) was used to develop the microbumps on copper surfaces. Each surface was plated for a given time period between 5 and 60 seconds. This illustration depicts the before and after of a zinc plated surface under a microscope to present the created microbumps.

The sliding angle was further enhanced by the silicone coating which reached 15°. Since the hydrophobicity of zinc and copper was improved by this treatment, we concluded that this method could be applied in industry such as developing anti-corroding bridges, pipes, and scaffolding.

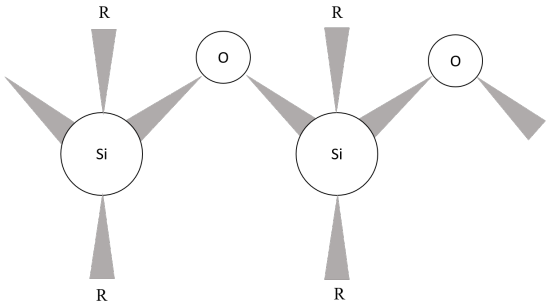

Figure 6: Illustration of the atomic structure of silicone. In this experiment, silicone was used to mimic the nanofiber hairs of the lotus leaf. In this structure, the repeating R groups of silicone makes it an ideal polymer chain for hydrophobic surfaces.

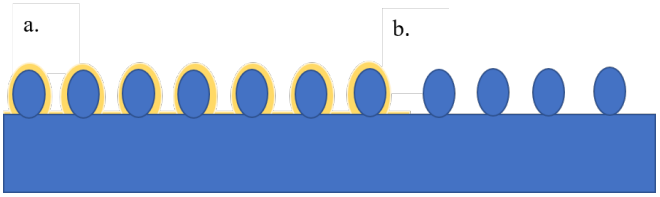

Figure 7: Illustration of a before and after image of silicone sprayed on a microbump surface. A thin layer of silicone is ideal for this surface as too much silicone will heavily cover the created microbumps.

	Contact Angles for Droplets (°)						
Time (s)	1	2	3	4	5	Average (°)	Standard Dev
Control:	71	52	68	67	63	64	7.4
5	110	115	104	123	106	112	6.8
10	118	115	125	128	119	121	4.8
15	119	113	107	123	97	112	9.1
20	125	112	104	131	117	118	9.6
25	115	116	131	117	128	121	6.9
30	125	118	121	118	121	120	2.3
35	115	112	123	125	124	120	5.5
40	130	121	128	136	131	129	5.1
45	139	134	134	127	113	129	8.8
50	130	130	121	126	129	127	3.3
55	118	101	103	102	102	105	6.5
60	113	95	93	101	91	99	8.0

Table 1: Zinc Contact Angle over Plating Time without Silicone Layer.

	Contact Angle for Droplets (°)						
Time(s)	1	2	3	4	5	Average (°)	Standard Dev
Control:	125	111	95	94	102	106	13.1
5	125	123	113	121	118	120	4.4
10	133	132	139	118	130	130	6.9
15	97	105	101	96	91	98	4.9
20	119	129	113	125	120	121	5.4
25	132	127	120	116	117	122	6.1
30	129	121	128	122	110	122	6.6
35	121	129	103	117	117	117	8.4
40	132	117	119	140	123	126	8.5
45	123	123	133	128	144	130	7.8
50	133	126	113	109	135	123	10.5
55	127	121	134	124	113	124	6.8
60	138	127	100	133	119	132	13.4

Table 2: Zince Contact Angle over Plating Time after Spraying Silicone Layer.

RESULTS

In this experiment, we cleaned flat metal sheets (zinc and copper), which then underwent an electrodeposition treatment. After drying, the surface was sprayed with a silicone layer to enhance its hydrophobicity. Contact angle and sliding angle were recorded in five second intervals. The size of the metal sheet, amount of silicone sprayed on the sheet, and the concentrations of the aqueous solutions ($CuSO_4$ and $Zn(NO_3)_2$) used for the electrodeposition process were kept constant.

Contact angles

Here, zinc contact angles were collected and examined to determine the effectiveness of electroplating methods in surface hydrophobicity. Over time, the contact angle generally increased until it peaked at 45 s. After, the contact angles began to decrease.

After creating microbumps with electrodeposition, a layer of silicone was sprayed to mimic the long chains of hydrocarbons on a lotus leaf. From the data, the contact angles with silicone generally stayed within the same range of values.

In order to examine the extent of the electrodeposition method, we also applied this method to copper. The contact angle increased until 15 s then showed slight decrease after its optimal time.

The contact angle of zinc with electroplating treatment only peaked at 45 s (**Figure 8, Tables 1 & 2**). Both plating with and without silicone generally followed a similar trend, where plating with silicone slightly enhanced the contact angle. As a result, electroplating microbumps greatly enhanced the hydrophobicity of the metal surface compared to the surface with only the silicone layer and control. However, the hydrophobicity before 45 s was not enhanced by the silicone possibly because the hydrophobicity from silicone was negligible compared to the hydrophobicity from the microbumps.

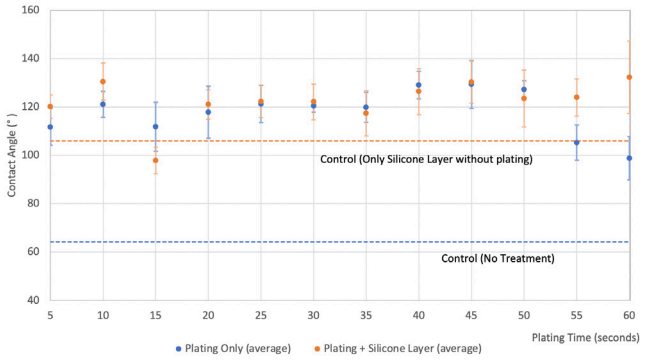

Figure 8: Zinc Contact Angle vs. Time of plating. A zinc surface was electroplated for different lengths of time (5–60 s) and the resulting contact angle was measured for each time point, with and without a silicone layer. Measurements were taken for four conditions: no treatment control (blue dashed line), silicone control (orange dashed line), electroplated only (blue), and electroplated with a silicone layer (orange) (n = 5 for each condition). Error bars represent one standard deviation.

The general trend of zinc (increase in the beginning and decrease after peak) was also present in copper (**Figure 9, Table 3**). Therefore, electroplating methods can be applied to different metals. However, since the peak of copper is at 15 s instead of 45 s, different metals can have different optimal plating times. Copper most likely had an earlier peak because it is a more noble metal.

Sliding angles

The sliding angles of water droplets also were collected and examined to study the surface's hydrophobicity in terms of sliding angle. When zinc was treated with only electrodeposition, the sliding angles showed rapid decrease in the beginning and plateaued after 25 s.

When the electrodeposited surfaces were coated with a silicone layer, there was a significant decrease in sliding angle compared to the non-silicone coated surface. Additionally, there was a general decrease in sliding angle over the electroplating time.

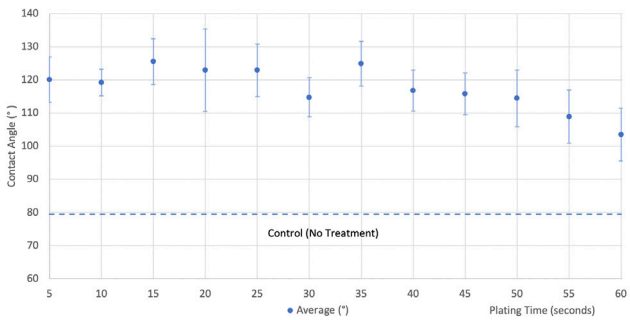

Figure 9: Copper Contact Angles without Silicone. A copper surface was electroplated for a different range of time (5-60 s), and the contact angle measurements were taken in a 5 s interval. The control (contact angle of the non-treated copper surface) is also shown in dotted line (n=5 for both control and treated surface). The error bars represent one standard deviation.

	Contact Angle for Droplets (°)						
Time (s)	1	2	3	4	5	Average (°)	Standard Dev
Control:	91	77	83	75	72	80	7.6
5	114	116	122	129	--	120	5.3
10	114	117	119	124	122	119	3.2
15	136	127	119	127	119	126	5.6
20	130	135	128	103	119	123	10.2
25	127	135	117	119	117	123	6.4
30	119	112	123	111	109	115	4.8
35	128	127	133	115	122	125	5.5
40	115	118	118	107	125	117	5.1
45	112	107	121	119	120	116	5.1
50	117	112	101	120	123	114	7.0
55	115	100	105	104	119	109	6.5
60	104	117	98	100	98	103	6.5

Table 3: The Contact Angle over Electroplating Time of Copper Surface without Silicone Layer.

As plating time increased, the sliding angle without a silicone layer decreased, supporting the hypothesis that the electroplating method enhances hydrophobicity (**Figure 10, Table 4 & 5**). The addition of silicone also enhanced the hydrophobicity and slipperiness of the zinc surface due to the polar repulsion of the silicone. After 25 s of the plated surface without silicone, the surface reached its optimal sliding angle.

DISCUSSION

The data supported the hypothesis that when microbumps are electrodeposited on a metal surface, the surface will develop hydrophobic properties which can be further enhanced by chemical surface treatment. Electrodeposition alone could achieve a contact angle of 129° and a sliding angle of 23°. The sliding angle was further enhanced by the silicone coating to reach 15°.

The electroplating treatment enhances a surface's hydrophobicity comparing the contact angles of the treated surface and that of the control (**Figure 8**). When comparing the values between 5 and 50 s, we concluded that there were no significant changes between each individual 5 s interval. At 55 and 60 s, the contact angles were significantly lower than the preceding contact angles. As a result, electroplating time should be shorter than 55 s to produce better hydrophobicity. Additionally, there is no significant enhancement in hydrophobicity with an addition of a silicone layer. The aid of a silicone layer did not enhance the contact angle since electrodeposition itself had already produced the desired hydrophobicity.

In order to test the electroplating method on different metals, electroplating treatment was performed on copper (**Figure 9**). Comparing the control to the plated surfaces, we concluded that plating also enhances a surface's hydrophobicity on copper surfaces. However, the contact angles between each

	Contact Angle for Droplets (°)						
Time (s)	1	2	3	4	5	Average (°)	Standard Dev
Control:	10	14	15	13	10	12	2.3
5	38	42	41	39	39	40	1.7
10	36	42	29	35	--	36	4.6
15	31	26	36	39	28	32	4.9
20	18	36	37	19	37	29	9.0
25	21	21	23	16	21	20	2.3
30	25	16	27	34	27	26	5.6
35	29	21	18	21	15	21	4.6
40	25	26	23	26	26	25	1.0
45	22	21	28	20	22	23	2.8
50	19	26	25	25	28	25	3.0
55	17	17	23	21	21	20	2.6
60	23	25	21	32	24	25	3.9

Table 4: Sliding Angle of Zinc Surface without Silicone Layer over Plating Time.

	Contact Angle for Droplets (°)						
Time (s)	1	2	3	4	5	Average (°)	Standard Dev
Control:	13	15	12	11	11	12	1.5
5	14	13	20	16	16	16	2.2
10	21	14	23	19	20	19	3.1
15	17	14	17	15	16	16	1.0
20	17	17	13	24	21	18	3.6
25	17	14	16	13	15	15	1.5
30	15	13	14	13	22	15	3.5
35	13	14	11	15	14	13	1.4
40	10	16	19	15	12	14	3.1
45	13	19	20	13	20	17	3.2
50	15	20	19	22	15	18	2.9
55	12	12	16	16	12	13	2.0
60	17	13	14	16	15	15	1.4

Table 5: Sliding Angle over Electroplating Time of Zinc Plated Surfaace with Addition of Silicone Layer.

interval was not significant. Yet, when comparing the change in hydrophobicity between a larger interval (ex. comparing the contact angles at 5 and 60 s), we concluded that there may be a significant change since the range of values do not overlap. Due to the significant difference between these two endpoints, the data shows that shorter electroplating time (5 s) results in better hydrophobicity than a longer electroplating time (60 s).

It was concluded that the plated surface with a silicone layer significantly enhances the surface's hydrophobicity compared to the plated surface without a silicone layer (**Figure 10**). Looking at the 'plating only' data (blue), there was a significant decrease from 5 s to 25 s with no value overlap, showing that hydrophobicity increased significantly during this time period. However, after 25 s, there were no significant changes between each 5 s interval since the values from points 25 to 60 s overlap each other. When comparing the two controls' sliding angles to the two treated surfaces' (with and without silicone) sliding angles, the controls' sliding angle proved to be lower. Additionally, when comparing the 'no treatment' control to the 'only silicone layer' control, the 'no treatment' control was also lower. As a result, the electroplated metals with and without a silicone layer and the 'only silicone layer' controlled surfaces did not contribute to the hydrophobicity of the metal surface in terms of sliding angle. Even though the data showed that hydrophobicity was

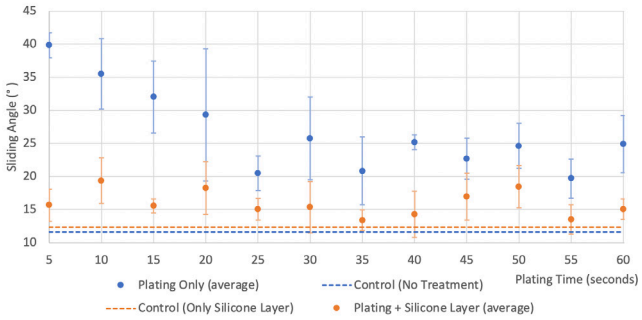

Figure 10: Zinc Sliding Angle vs. Time of Plating. Two groups of zinc surface were electroplated for different lengths of time (5-60 s), and one group of the electroplated sample was coated with a silicone layer after the electrodeposition while another was only electroplated. Measurements were taken for both groups: electroplated with a silicon layer (orange) and electroplated only (blue). The control for both groups is also shown: no treatment control (blue dashed line) and only silicon layer without electrodeposition (orange dashed line) (n = 5 for all four data). Error bars draw the range of one standard deviation.

not improved, we observed that with a silicone coating, there was no water residue left on the surface whereas surfaces without silicone, water residue was present.

For future experimentation regarding electrodeposition, optimal electrodeposition conditions (electrode geometry, current density, electrolyte composite, and temperature) that create uniform hydrophobicity across the metal surface should be collected along with applying microscopy to reveal geometry and dimensions of surface features. For copper metal surfaces, a larger range of electroplating time is needed to determine the optimal plating time. For experiments regarding the silicone coating, different dilutions, solvents, and siloxanes should be experimented with to obtain an optimal polymer coating. Additionally, different industrial metals such as aluminum and steel should be tested so that a program could be developed to predict the optimal plating time for different industrial metals.

Generally, the hydrophobicity increased in terms of contact angle, but the hydrophobicity did not improve in terms of sliding angle. Therefore, depending on the application of the hydrophobic surface, certain methods (electrodeposition, silicone layer, or both) to obtain a hydrophobic surface should be considered.

METHODS

A metal sheet (copper and zinc) was cut into 7.5 cm x 3 cm portions for manageability. All the metal portions were cleaned with acetone and dishwashing soap before experimentation in order to remove contaminants. Using two of the same types of metal strips at a time, one strip was used as an anode while the other strip was used as the cathode. The anode strip was labeled and was attached to the positive end of the battery with an alligator clip. Likewise, the cathode zinc strip was attached to the negative end of the battery using another alligator clip. Once attached to the battery, both metal portions were placed in an aqueous solution containing the metal compound for a given amount of time (**Figure 5**). The aqueous solution used for copper was with a concentration of 84 mM, and the aqueous solution for zinc was $Zn(NO_3)_2$ with a concentration of 106 mM. The rest of the materials and the times were kept constant.

After plating, the cathode strip, where microbumps have been plated by reduction, was placed in the oven (135°C) for about 15 minutes until dry. Then, it was air-dried overnight to remove any remaining liquid. Since electrodeposition is a rapid reaction, the surfaces underwent treatment in 5 s intervals to examine the surface changes in detail. This process was repeated from 5 to 60 s for each metal surface.

In addition to modifying the physical structure of the hydrophobic surface, chemical treatment was also done. Inspired from the nanofibers found on the surface of lotus plants, a polymer chain was deposited on the bumpy surface to decrease the sliding angle. Since silicone can bind with repeating R-groups to form long chains (**Figure 6**), it was used as the polymer for this experiment. Liquid silicone (product from GE Sealants & Adhesives) was dissolved into xylene in a 1:3 g ratio to reduce the silicone's viscosity. This was then sprayed onto the plated surface (**Figure 7**). As the xylene evaporated, the silicone was left behind as a precipitate, forming a layer of silicone chains.

The contact angles for all samples were measured using the ImageJ image analysis program (19). The water droplet was photographed at eye level to get an accurate contact angle. The average and standard deviation was calculated to determine an accurate representation of the data. In order to compare the effectiveness of these methods, the contact angle and sliding angle of zinc and copper without any treatment were measured. Additionally, the contact and sliding angles of zinc surfaces with only a silicone coating were measured. These controls were used as the standard of comparison between the effectiveness of the developed electroplating method and the existing method of spraying hydrophobic chemicals to the surface to create water-repellent surfaces.

ACKNOWLEDGMENTS

We would like to thank Brooklyn Technical High School for allowing us to facilitate our experimentation, Ms. Sirianni for providing us the necessary resources, and the Journal of Emerging Investigators staff for reading over our work.

Received: September 30, 2020
Accepted: November 30, 2020
Published: January 13, 2021

REFERENCES

1. Li, Zongchen, *et al*. "External Surface Cracked Offshore Steel Pipes Reinforced with Composite Repair System Subjected to Cyclic Bending: An Experimental Investigation." *Theoretical and Applied Fracture Mechanics*, vol. 109, 2020, doi:10.1016/j.tafmec.2020.102703.
2. Shirtcliffe, Neil J., *et al*. "Superhydrophobic Copper Tubes with Possible Flow Enhancement and Drag Reduction." *ACS Applied Materials & Interfaces*, vol. 1, no. 6, 2009, pp. 1316–23. doi:10.1021/am9001937.
3. Eseev, Marat, *et al*. "Creation of Superhydrophobic Coatings Based on MWCNTs Xerogel." *Nanomaterials*, vol. 9, no. 11, 2019. doi:10.3390/nano9111584.
4. Sharma, Vipin Kumar, *et al*. "Parametric Study of Aluminium-Rare Earth Based Composites with Improved Hydrophobicity Using Response Surface Method." *Journal of Materials Research and Technology*, vol. 9, no. 3, 2020, pp. 4919–32. doi:10.1016/j.jmrt.2020.03.011.
5. Ding, Yi, *et al*. "Critical Sliding Angle of Water Droplet on Parallel Hydrophobic Grooved Surface." *Colloids and Surfaces A: Physicochemical and Engineering Aspects*, vol. 585, 2020, doi:10.1016/j.colsurfa.2019.124083.
6. Montes Ruiz-Cabello, *et al*. "Fabrication of Superhydrophobic Metal Surfaces for Anti-Icing Applications." *Journal of Visualized Experiments: JoVE*, no. 138, 2018. doi:10.3791/57635.
7. Chen, Huaxin, *et al*. "Review of Ice-Pavement Adhesion Study and Development of Hydrophobic Surface in Pavement Deicing." *Journal of Traffic and Transportation Engineering (English Edition)*, vol. 5, no. 3, 2018, pp. 224–38. doi:10.1016/j.jtte.2018.03.002.
8. V. Oriani, Andrea, *et al*. "Aluminium Electrodeposition from a Novel Hydrophobic Ionic Liquid Tetramethyl Guanidinium-Perfluoro-3-Oxa-4,5 Dichloro-Pentan-Sulphonate." *Journal of Electroanalytical Chemistry*, vol. 793, 2017, pp. 85–92. doi:10.1016/j.jelechem.2016.09.041.

9. Dalvi, Vishwanath H., and Peter J. Rossky. “Molecular Origins of Fluorocarbon Hydrophobicity.” *Proceedings of the National Academy of Sciences of the United States of America*, vol. 107, no. 31, 2010, pp. 13603–07. doi:10.1073/pnas.0915169107.
10. Kwon, Min Ho, *et al*. “Fabrication of a Super-Hydrophobic Surface on Metal Using Laser Ablation and Electrodeposition.” *Applied Surface Science*, vol. 288, 2014, pp. 222–28. doi:10.1016/j.apsusc.2013.10.011.
11. Wang, Daheng, *et al*. “Tomato-Lotus Inspired Edible Superhydrophobic Artificial Lotus Leaf.” *Chemical Engineering Journal*, vol. 400, 2020, doi:10.1016/j.cej.2020.125883.
12. Kim, Woochan, *et al*. “Engineering Lotus Leaf-Inspired Micro- and Nanostructures for the Manipulation of Functional Engineering Platforms.” *Journal of Industrial and Engineering Chemistry*, vol. 61, 2018, pp. 39–52. doi:10.1016/j.jiec.2017.11.045.
13. Ghaffari, Sepehr, *et al*. “Review of Superoleophobic Surfaces: Evaluation, Fabrication Methods, and Industrial Applications.” *Surfaces and Interfaces*, vol. 17, 2019, doi:10.1016/j.surfin.2019.100340.
14. Wae AbdulKadir, Wan Aisyah Fadilah, *et al*. “Biomimetic Hydrophobic Membrane: A Review of Anti-Wetting Properties as a Potential Factor in Membrane Development for Membrane Distillation (MD).” *Journal of Industrial and Engineering Chemistry*, 2020. doi:10.1016/j.jiec.2020.08.005.
15. Shaoxian, Bai, and Wen Shizhu. “Chapter 7 - Vapor-Condensed Gas Lubrication of Face Seals.” *Gas Thermohydrodynamic Lubrication and Seals,* 2019, pp. 143–65. doi:10.1016/B978-0-12-816716-8.00007-3.
16. Dai, Xianming, *et al*. “Slippery Wenzel State.” *ACS Nano*, vol. 9, no. 9, 2015, pp. 9260–67. doi:10.1021/acsnano.5b04151.
17. Burton, Zachary, and Bharat Bhushan. “Surface Characterization and Adhesion and Friction Properties of Hydrophobic Leaf Surfaces.” *Ultramicroscopy*, vol. 106, no. 8, 2006, pp. 709–19. doi:10.1016/j.ultramic.2005.10.007.
18. Giacomello, Alberto, *et al*. “Cassie–Baxter and Wenzel States on a Nanostructured Surface: Phase Diagram, Metastabilities, and Transition Mechanism by Atomistic Free Energy Calculations.” *Langmuir*, vol. 28, no. 29, American Chemical Society, 2012, pp. 10764–72. doi:10.1021/la3018453.
19. Schneider, Caroline, *et al*. “NIH Image to ImageJ: 25 years of image analysis”, *Nature Methods*, vol. 9, no. 7, 2012, pp. 671-675, doi: 10.1038/nmeth.2089.

JOURNAL OF
EMERGING INVESTIGATORS

Article

From Waste to Wealth: Making Millivolts from Microbes!

Hamza Arman Lateef[1]*, Tony Ethan Bright[1]*, Debra Peterman[2]
[1] Charles J. Colgan High School, Manassas, Virginia
[2] Louise A. Benton Middle School, Manassas, Virginia
* Investigators contributed equally.

SUMMARY

Biofuels can reduce our reliance on fossil energy sources while also protecting our environment. A Microbial Fuel Cell (MFC) is a system in which microorganisms produce electricity while performing their normal metabolism. The purpose of this project was to engineer a series of MFCs and manipulate circuit components to optimize voltage production. Each two-chamber MFC was created using creek mud, presumably rich in anaerobic exoelectrogenic bacteria, in the anode chamber and water in the cathode chamber. Four types of MFCs (three in each group) were constructed: 1) Mud in anode and water in cathode chambers; 2) Mud and sucrose in anode and water in cathode chambers; 3) Mud in anode and water and iron filings in cathode chambers; 4) Mud and sucrose in anode and water and iron filings in cathode chambers. Voltage output was recoded over twelve days. MFCs with iron filings (alone or with sucrose) consistently produced more voltage than the MFC with mud alone. Adding iron filings to the cathode chamber increased voltage output by 49%. While sugar alone in the anode chamber did not increase voltage output, the combination of sugar in the anode and iron filings in the cathode chambers did increase voltage output by 69% when compared to the MFC with mud alone. Our experiment demonstrated that MCFs can be optimized by manipulating bacterial substrate and using metal electron acceptors. We must invest in our planet's future by supporting large scale research on MFCs that can produce clean electric energy and purify environmental waste.

INTRODUCTION

Worldwide, human energy use requires over 11 billion tons of non-renewable fuels every year. This rapid consumption of fossil fuels, such as coal, oil, and natural gas, is depleting these non-renewable energy sources and polluting the earth. While there are several greenhouse gases responsible for global warming, carbon dioxide (CO2) is the major contributor, and it is produced by the combustion of fossil fuels in cars, factories, and electricity production facilities (1). Research shows that the earth's population is growing at a fast rate and is anticipated to reach 9.7 billion by 2050 (2), which means the world's energy needs will continue to increase. Renewable clean energy sources are one solution to the current global problem, allowing energy production while respecting the environment and reducing contamination in the atmosphere.

Electricity is a part of nature and one of the most widely used forms of energy. Conductors are materials or elements in which electrons flow easily between atoms (e.g. copper, silver, aluminum). It is this flow of electrons that constitutes an electric current (measured in Amperes), and any opposition to this flow is called the resistance (measured in Ohms). Thus, an electric circuit is a system of conductors and components forming a complete path for current to travel. In a battery, for example, the electrons flow out of the negative side (anode) of the battery, through the circuit, and back to the positive side (cathode) of the battery. The force or pressure that causes the current to flow in a circuit is called the voltage (measured in Volts). In summary, all one needs to generate electricity is a source of electrons and a voltage that causes the electrons to move through a circuit (3).

In the world today, we produce electricity mostly by using primary energy sources, such as coal and natural gas, which are non-renewable and pollute the environment. Solar, wind, and water are examples of clean energy sources that are already in use, while there are others sources that are in various stages of development. One such fascinating possibility is the idea of a microbial fuel cell (MFC) in which microorganisms produce an electric current while performing their metabolic processes. The basic principle of a MFC is that the chemical energy stored in organic matter is converted to electrical energy when the microorganisms metabolize the organic matter (4). All living organisms, including bacteria, undergo cellular respiration, a series of metabolic processes by which the chemical energy in organic matter/food (such as glucose) is broken down to produce energy for the living cells (5). The energy of the substrate is stored in the chemical bonds, or shared electrons, of the organic molecules. As the bonds are broken, and electrons flow through various metabolic reactions, energy is transformed into usable forms by the cells and living organisms. Eventually, the electrons are transferred to an electron acceptor, and when that final acceptor is oxygen, the process is called aerobic respiration. Unlike most living creatures, some bacteria do not require oxygen to survive, and they conduct their cellular respiration without oxygen. Some of these anaerobic bacteria can transfer the electrons obtained during cellular metabolism to a final electron acceptor in the outside environment (6). It is these types of exoelectrogenic bacteria that can be used to create MCFs.

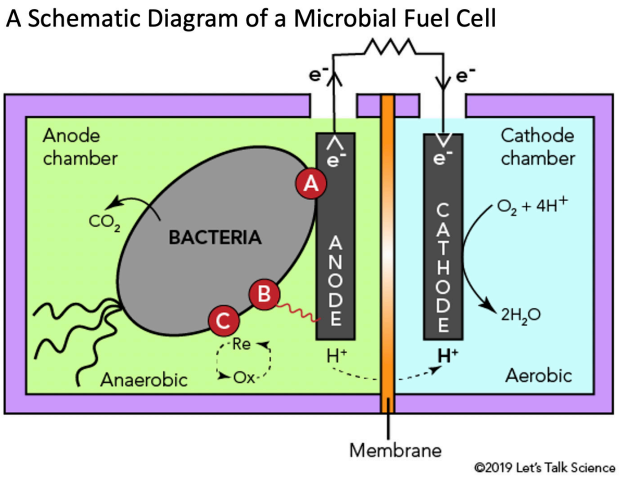

Figure 1: A microbial fuel cell is composed of four basic parts: an anode, a cathode, electrodes and an external load. Electrons can be carried by protein carriers (A), nanowires (B) or mediators (C) (© 2019 used with permission from Let's Talk Science [linkprotect.cudasvc.com]).

A microbial fuel cell is composed of four basic parts: an anode, a cathode, electrodes, and an external load (**Figure 1**) (7). The anode is where the organic matter is present and where the microorganisms grow. It has electron-rich substrate but contains no oxygen or final electron acceptor, hence it is an anaerobic environment. In contrast, the cathode is rich in oxygen, usually contains water, and sometimes has other electron acceptors, such as metals.

To connect the anode and cathode, electrodes and an external load are used. These components make up an electric circuit in which electrons given off by the bacteria travel from the anode compartment to the cathode compartment as an electric current, which can be harnessed or measured through the external load. Lastly, the fuel cell includes a semipermeable connection between the two chambers that allows protons to flow from the anode to the cathode, where they can recombine with electrons and oxygen to form water. This membrane does not allow the passage of electron acceptors from the cathode into the anode, thereby forcing the electrons to travel the circuit and generate current. A salt bridge is commonly used for the semi-permeable membrane connection between the two compartments. The flow of electrons through the circuit creates electricity by producing a potential difference across the two electrodes, and this is the ultimate voltage output of the fuel cell, which can be measured using a voltmeter. Voltage output is directly related to microbial growth and will decrease as the bacteria start to die.

As Rabaey and colleagues have described, MFCs present an exciting opportunity to create clean, renewable energy and have many advantages. First, microorganisms can be found in all environments and easily accessed in soil and wastewater, for example. They are also easy to grow and replenish. Second, by providing microorganisms with organic matter, we can extend the lifespan of these cultures, making this technology sustainable. Third, since oxygen is the final electron acceptor, and water is the byproduct, no harmful chemical waste is produced. Finally, besides producing electricity, MFCs can be used in wastewater treatment for food processing industries and sewage, since this water is rich in organic material. Microorganisms simultaneously break down this organic matter and clean up the water (8). Despite all of these advantages, MFCs are not widely used as they have limited voltage output (9). Much current research focuses on how best to improve efficiency by decreasing loss of energy, boosting the substrate, and decreasing the resistance.

Parameter	Voltage in mV			
	Mud	Mud + Sucrose	Mud + Iron	Mud + Sucrose + Iron
Mean	156.8	163.5	227.9	280.7
Standard Deviation	15.8	17.7	27.9	37.1
Standard Error	4.6	5.1	8.0	10.7
Maximum Voltage	190	188	282	351
Minimum Voltage	121	122	180	205

Table 1: Comparison between the density, faradic capacity, and theoretical voltage of magnesium, aluminum, and zinc (5).

We have therefore designed and constructed a series of fuel cells to determine whether we can improve the performance of the MFC by enhancing the food supply of the bacterial colonies, optimizing the electrical circuit with the addition of iron as an electron acceptor, and combining substrate augmentation and using iron as an electron acceptor. We hypothesized that the addition of sucrose to the anode chamber, iron to the cathode chamber, and the combination of these factors would lead to an increase in voltage output by the MFC. Our results showed that the addition of iron filings in the cathode chamber, with or without sucrose, increased voltage output by 69% or 49% respectively, while sucrose alone did not increase voltage output.

RESULTS

We used a total of 12 MFCs, with 3 MFCs for each group: Mud only, Mud + Sucrose, Mud + Iron, and Mud + Sucrose +

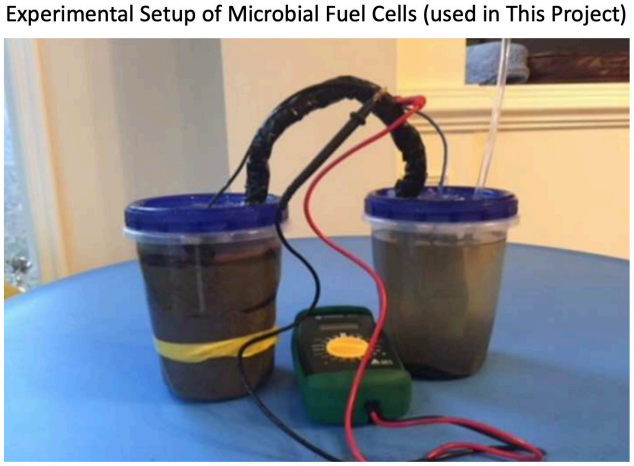

Figure 2: A photograph of one of the MFCs constructed

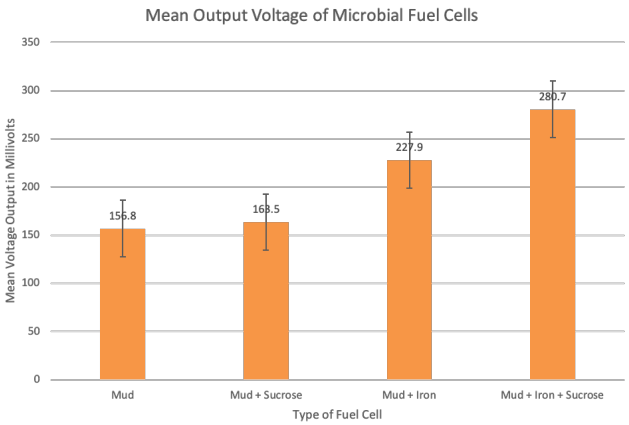

Figure 3: A total of 12 Microbial Fuel Cells were used, with 3 MFCs for each: Mud only, Mud + Sucrose, Mud + Iron and Mud + Sucrose + Iron. The mean voltage output and standard errors for Mud only, Mud + Sucrose, Mud + Iron and Mud + Sucrose + Iron were 121 mV (SE 4.6), 122 mV (SE 5.1), 180 mV (SE 8.0) and 205 mV (SE 10.7) respectively.

Iron. The mean voltage output and standard errors for Mud only, Mud + Sucrose, Mud + Iron, and Mud + Sucrose + Iron were 121 ± 4.6 mV, 122 ± 5.1 mV, 180 ± 8.0 mV, and 205 ± 10.7 mV, respectively (**Table 1** and **Figure 2**). **Figure 3** shows the voltage generated by each type of MFC over a period of 14 days. Maximum voltage was attained with Mud + Iron, and minimum voltage was with Mud alone. There was no significant difference in voltage output with sugar added to the anode chamber compared to mud alone. However, there was a significant increase of 49% in voltage output by adding iron filings to the cathode chamber. While the addition of sugar to the anode chamber did not significantly improve the voltage output, the sugar in combination with the iron filings did cause an increase in voltage output of 69% when compared to the MFC with mud alone. We observed that adding sucrose as a substrate for the bacteria seemed to slightly decrease the rate at which the voltage decreased (**Figure 4**).

We found no significant difference in voltage output with sugar added to the MFC (p = 0.900); however, there was a significant increase in voltage output by adding iron filings (p<0.001) when compared to the MFC with mud alone. While adding sugar to the anode chamber did not significantly improve the voltage output, the sugar in combination with iron filings did cause an increase in voltage output when compared to mud alone (p<0.001) and when compared to the MFC with mud and iron filings (p<0.001) as well.

DISCUSSION

Electricity production and maintaining a clean environment play a vital role in human life; the MFC is a technology that performs both functions by employing microbes in a controlled environment. In our project, we successfully engineered multiple types of MCFs to determine whether we can improve the performance of the MFC by manipulating bacterial substrate and adding a metal electron acceptor. We found that the addition of sucrose did not significantly improve

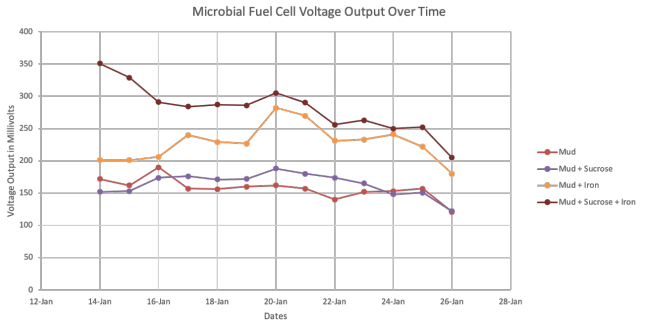

Figure 4: The voltage output of MFC over a period of fourteen days. The MFC with iron and sucrose consistently performed better than the other fuel cells.

the performance of the fuel cell. However, our data showed that the addition of iron filings did significantly enhance the voltage output of the fuel cell. The combination fuel cell with sucrose in the anode and iron in the cathode did much better than the fuel cell with mud alone.

In MFCs, the substrate is regarded as one of the most important factors affecting electricity generation as it can affect the composition and density of the microbial community, which is the electrical charge generator (11). We chose to add sucrose (a polymer of glucose and fructose) to our mud anode chamber as prior research has shown bacteria found within mud can metabolize glucose to successfully produce electricity (9). Unlike Rabaey and colleagues, we did not see any significant improvement in voltage output with this addition (9). It is possible that the specific bacterial composition found in our creek mud differed from that of others. Also, perhaps using the simplest sugar forms, such as glucose or fructose, might have yielded better higher voltage output had the more complex form, sucrose. It is possible that the bacteria lacked the enzymatic reactions necessary to break down this complex sugar.

Electron acceptors receive electrons from the cathode and make a significant contribution to the performance of the MFC. Different electron acceptors exhibit physically and chemically different properties (e.g., oxidation potential) and therefore affect the efficiency of electricity production. Ferric iron can be reduced to ferrous iron in the cathode chamber by accepting electrons. This reversible electron transfer reaction provides several advantages, such as fast reaction, high standard potentials, and biological degradability (12). Our work confirmed prior research (8) that iron can be successfully used as electron acceptors and thus reduced to the less toxic ferrous form.

While the addition of sugar to the anode chamber did not significantly improve the voltage output, the sugar in combination with the iron filings did cause an increase in voltage output when compared to the MFC with iron filings alone, and this closely approached statistical significance (p-value = $1.1102e^{-16}$). To our knowledge, prior research has not looked at substrate manipulation in combination with the addition of electron acceptors. It is possible that in the MFC with sucrose added, the bacterial colonies may have been

able to grow and multiply more robustly, but the electrons produced could not be delivered with any more efficiency to the cathode. Future experiments may be able to evaluate this by measuring bacterial growth in conjunction with voltage output. This indicates that perhaps adding metal conductors to the cathode chamber can have a much larger impact on fuel cell efficiency than simply providing a greater substrate concentration to the bacteria in any given MFC. Future studies should expand the types of substrate used, as well as electron acceptors, to find the combination that yields maximal energy output.

There are many aspects to our experiment that we could not entirely predict. For example, towards the end of two weeks we may have had bacteria growing in the cathode area or even other small organisms, such as fungi. Also, the bacteria may not be able to grow and reproduce under our experimental conditions as well as they would in their natural habitat and associated parameters of light, temperature and other microorganisms.

We successfully constructed our own MFCs from individual components with minimal outside assistance. Our findings with regards to combining substrate and electron acceptor manipulations suggest a potential new strategy to maximize microbial fuel cell efficiency. The size of the fuel cells used and type of electrode components were limited by space and budget limitations. As with prior studies, our MFCs were hindered by relatively low voltage output, which can be attributed to a number of factors, such as high internal resistance, nature of the electrodes, and substrate.

MFC technology must overcome many hurdles before it can be implemented as a form of bioelectricity and wastewater treatment. As with other renewable energy sources it must face challenges of having an extensive infrastructure, including space and installation technologies, to support large scale production. However, our experiment has provided major insight into the creation and potential optimization of MFCs. We must invest in our planet's future by supporting further studies on MFCs, conducted on a larger scale, to produce clean electric energy and purify environmental waste.

MATERIALS AND METHODS

Based on the literature, we engineered a microbial fuel cell and used existing research to optimize the production of electric current. Voltage output is directly related to microbial growth rate, which in turn depends on a supply of food substrate. We included sucrose as a food substrate, to our anode chamber, because sucrose can be broken down to the simple sugars - glucose and fructose. We expected this to increase electricity production since carbohydrates are by far the most abundant group used in prior studies such as the one conducted by Rabaey and colleagues where investigated the power output of an MFC in relation to glucose dosage containing a mixed bacterial culture utilizing glucose as a substrate. They found that electron recovery, in terms of bioelectricity, of up to 89% occurred for glucose as a substrate in the anodic chamber (9).

We decided to use iron as an electron mediator to enhance the performance in the cathode compartment. Ferric iron can be reduced to ferrous iron in the cathode chamber according to equation, $Fe^{3+} + e^- \rightarrow Fe^{2+}$ (10). In terms of electron acceptors used in the cathode compartment, oxygen is the most widely used, due to its high oxidation potential and the fact that it yields a clean product (water) after reduction. However, research suggests that the use of alternative electron acceptors may not only increase the power generation and reduce the operating costs but also expand the potential applications of MFCs (10). Prior work in this area demonstrates that metals such as iron and mercury (8), can also be used as electron acceptors and are reduced to less toxic forms. Thus, electricity generation and wastewater treatment take place simultaneously.

Each two-chamber MFC was created using mud in the anode chamber and water in the cathode chamber (see **Figure 4**). mud was obtained from the bottom of a creek in Laurenwood Estates in Manassas, VA with the assumption that this aquatic source would contain sufficient quantities of anaerobic bacteria, such as *Shewanella oneidensis*. The mud was thoroughly mixed so that each sample contained approximately equal bacterial species. The chambers were constructed from plastic Ziploc containers. On the container lids, we drilled one hole for copper wire, an additional hole for the air pump, and one hole into each lid for the salt bridge. Electrodes made from aluminum mesh were fixed to both chambers and connected via a copper wire to the external resistor or voltmeter. A salt bridge (using rope saturated with salt water) was also constructed, connecting the chambers. All experiments were conducted under room temperature and normal ambient light conditions. We used 750 mL of mud, 1 tablespoon of sucrose, and 1 tablespoon of iron filings per chamber (x6).

A total of 12 MFCs were engineered, with 3 replicates designed to test each of 4 experimental conditions: 1) mud in anode and water in cathode chambers; 2) mud and sucrose in anode and water in cathode chambers; 3) mud in anode and water and iron filings in cathode chambers; and 4) mud and sucrose in anode and water and iron filings in cathode chambers. Voltage output was recoded using a voltmeter twice daily for 12 days. A picture of one of the MFCs constructed shown in **Figure 4**.

From voltage measurements, the mean and standard deviation was computed using Excel. To determine statistical significance, we ran a one-way ANOVA test for our four independent experimental groups and derived an F-statistic of 65.5243 and a *p*-value of $1.1102e^{-16}$. Next, we applied the Tukey HSD post-hoc test to identify which pairs of groups were significantly different from each other.

Received: July 21, 2020
Accepted: October 26, 2020
Published: January 19, 2021

REFERENCES

1. Causes of Global Warming, Human influence is rapidly changing the climate. Accessed at https://www.nationalgeographic.com/environment/global-warming/global-warming-causes/
2. World population projected to reach 9.7 billion by 2050. Accessed at http://www.un.org/en/development/desa/news/population/2015-report.html
3. How do electric circuits work? Accessed at http://discoverykids.com/articles/how-do-electric-circuits-work/
4. Mercer J (2014). *Microbial Fuel Cells: Generating Power from Waste. A review of engineering in everyday life*. Volume XII Issue II Mader S.S .& Windelspecht, M. (©2012) *Human biology* /New York, NY : McGraw-Hill
5. Logan BE, Hamelers B, Rozendal R, Schroder U, Keller J, Freguia S… Rabaey K *et al*. (2006) Microbial Fuel Cells: Methodology and Technology. *Environmental Science and Technology*. VOL. 40, NO. 17
6. Logan BE.(2009). Exoelectrogenic bacteria that power microbial fuel cells. *Nature Reviews Microbiology* 7, 375–381.doi:10.1038/nrmicro2113
7. Wang Z, Lim B, Choi C. (2011). Removal of Hg^{2+} as an electron acceptor coupled with power generation using a microbial fuel cell. *Bioresour Technol*. 102(10):6304-7. doi:10.1016/j.biortech.2011.02.027.
8. Rabaey, K., Lissens, G., Siciliano, S. D., and Verstraete, W. (2003). A microbial fuel cell capable of converting glucose to electricity at high rate and efficiency. *Biotechnol Letters*, 25: 1531–1535.
9. Ucar D, Zhang Y, and Angelidaki I. (2017). An Overview of Electron Acceptors in Microbial Fuel Cells. *Front Microbiol*, 8: 643.doi:10.3389/fmicb.2017.0064z
10. Garba* N.A., Sa'adu L., and Balarabe M.D. (2017). An Overview of the Substrates used in Microbial Fuel Cells. *Greener Journal of Biochemistry and Biotechnology* Vol. 4 (2), pp. 007-026, May 2017.doi: http://doi.org/10.15580/gjbb.2017.2.05151706z
11. Heijne, A., Hamelers, H.V.M., DeWilde, V., Rozendal, R. A., and Buisman, C. J.N. (2006). A Bipolar Membrane Combined with Ferric Iron Reduction as an Efficient Cathode System in Microbial Fuel Cells. *Environ. Sci. Technol*. 40, 5200–5205.doi:10.1021/es0608545
12. The end of fossil fuels. Accessed at https://www.ecotricity.co.uk/our-green-energy/energy-independence/the-end-of-fossil-fuels

JOURNAL OF
EMERGING INVESTIGATORS

Article

High-throughput virtual screening of novel dihydropyrimidine monastrol analogs reveals robust structure-activity relationship to kinesin Eg5 binding thermodynamics

Tyler Shern[1,4], Ansh Rai[1,4], Krithikaa Premnath[2,4], Audrey Kwan[3,4], Ria Kolala[1,4], Ishani Ashok[1,4], Edward Njoo[4]

[1]Mission San Jose High School, Fremont, CA
[2]Dougherty Valley High School, San Ramon, CA
[3]Dublin High School, Dublin, CA
[4]Department of Chemistry, Biochemistry & Physics, Aspiring Scholars Directed Research Program, Fremont, CA

SUMMARY

As cancer continues to take millions of lives worldwide, the need to create effective therapeutics for the disease persists. The kinesin Eg5 assembly motor protein is a promising target for cancer therapeutics as inhibition of this protein leads to cell cycle arrest. Monastrol, a small dihydropyrimidine-based molecule capable of inhibiting the kinesin Eg5 function, has attracted the attention of medicinal chemists with its potency, affinity, and specificity to the highly targeted loop5/α2/α3 allosteric binding pocket. In this work, we employed high-throughput virtual screening (HTVS) to identify potential small molecule Eg5 inhibitors from a designed set of novel dihydropyrimidine analogs structurally similar to monastrol. Density functional theory (DFT) calculations and protein-ligand docking experiments revealed that the analogs with geranyl ester substitutions exhibited the greatest binding affinities to the allosteric binding pocket of kinesin Eg5. In-depth analysis of the binding pocket amino acid residues and calculations of the cLogP value for each compound demonstrated qualitatively and quantitatively that strong hydrophobic interactions of the ester functionality with kinesin Eg5 are of great significance in the improved binding of dihydropyrimidine analogs. This establishment of a quantitative structure-activity relationship to kinesin Eg5 binding thermodynamics using HTVS revealed the discovery of improved dihydropyrimidine-based inhibitors capable of advancing society's progress in the fight against cancer.

INTRODUCTION

In 2019, cancer was responsible for over 600,000 deaths throughout the United States (1). Though cancer is currently the second highest leading cause of death, the mortality rates for this disease have declined by 27% over the past 25 years, and these improvements in survival rates have been attributed mainly to advances in early detection and treatment (2). Many of the successful small molecule therapeutics for cancer have been the product of years of intensive drug discovery research, involving the identification of potential candidates through screening of naturally derived or synthetic compounds.

Kinesin Eg5 is a motor protein involved in the assembly and separation of mitotic spindle fibers in the cell cycle and plays a critical role in the establishment of spindle bipolarity (3, 4). Eg5 is generally not expressed in non-proliferating adult tissues and thus results in diminished toxicity when treated with Eg5-targeted therapies, especially when compared to other modern anti-mitotic therapeutics available on the market (5). Researchers have considered the inhibition of kinesin Eg5 as a high potential avenue for cancer therapy, especially with Eg5 overexpressed in breast carcinogenesis, laryngeal squamous cell carcinoma, astrocytic neoplasm, prostate cancer, bladder cancer, and renal cell carcinoma (6).

In 2000, the Mitchison group reported the discovery of monastrol, a small molecule dihydropyrimidine (DHPM) that allosterically inhibits kinesin Eg5 (Figure 1) (7). Following this revelation, DHPMs have gained significant interest in medicinal chemistry. The synthesis of other DHPMs structurally similar to monastrol has demonstrated great potential in the development of increasingly potent anticancer agents capable of treating aggressive glioma, renal, and breast cancers in past studies (8).

Monastrol binds to the loop5/α2/α3 allosteric site of kinesin Eg5 through hydrophobic interactions and hydrogen bonding, inducing conformational changes in Eg5 and preventing continued mitotic division (9). With kinesin Eg5 expression considered to be generally overexpressed in neoplastic tissue, the high selectivity of monastrol to mitotically active cancer cells suggests strengthened responses and fewer cytotoxic side effects when compared to other anticancer agents (6). As previous in vitro and in vivo studies have concluded that the S-monastrol is a more potent inhibitor of kinesin-Eg5 than the R-enantiomer, this work focuses solely on the former (10). Given the significance of biological activity that monastrol produces, it has been of deep interest to use the DHPM scaffold to create more potent inhibitors of kinesin Eg5.

High-throughput virtual screening (HTVS) provides an efficient computational method to discover the most effective compounds from massive libraries of analogs to a set of finite user-defined conditions. Molecular docking is a technique in which the thermodynamic efficiency of molecular interactions is calculated, shedding time-efficient, detailed insight into the specificity of binding for improved lead optimization. These values can be used in the prediction of the binding thermodynamics and preferred binding poses of small molecule ligands to protein targets (11). In this work, we hypothesize that the binding affinity of such analogs is primarily related to hydrophobic interactions that the ester functionality is engaged in with hydrophobic residues of the reported allosteric binding pocket.

This study focused on the computational screening of systematic modifications of the aromatic and ester constituents of monastrol, as displayed in Figure 2. The analogs presented in this study encompass a variety of aromatic and ester substitutions (Figure 3). We implemented HTVS to establish a robust, quantitative structure-activity relationship (QSAR) between the binding affinities of our novel dihydropyrimidine analogs and kinesin Eg5. We assessed 100 analogs for increased antiproliferative abilities in hopes of discovering improved small molecule cancer therapeutics. The results not only indicated that analogs with geranyl substitutions represent lead compounds that should be synthesized, but also revealed that enhanced kinesin Eg5 binding thermodynamics are attributed greatly to hydrophobic interactions between the ester functionality and Eg5.

RESULTS

The first computational docking software used was Swissdock. Each of the 100 analogs was docked onto the kinesin Eg5 receptor (PDB: 3HQD) with the grid box center having coordinates of (21.738, 26.509, 51.081) and the grid box dimensions being (40, 44, 40). Predicted free energies of binding (ΔG) and the differences in the binding affinities between each analog and the original monastrol molecule are reported in Table 1. As AR12 has the same chemical structure as monastrol, we compared each of the Swissdock binding energies for the other 99 analogs against the control monastrol ΔG value of -7.31 kcal/mol.

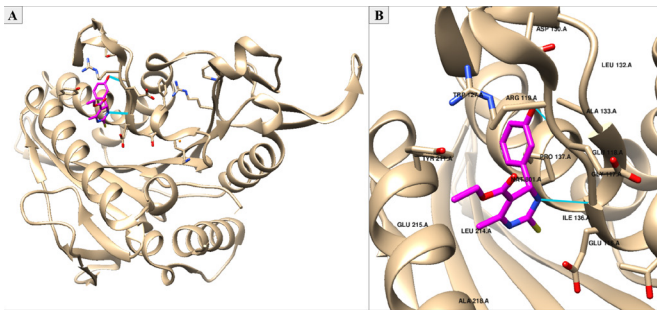

Figure 1: Human kinesin Eg5 motor protein structure. (A) The crystal structure of the human kinesin Eg5 motor protein bound to monastrol in the loop5/α2/α3 allosteric binding pocket. The magenta structure is monastrol, while the gold structure is the kinesin Eg5 protein. We extracted the crystallized protein structure from the Protein Data Bank (PDB: 1X88) and visualized it using UCSF Chimera. (B) A closer visualization of the binding site, with monastrol engaging in several hydrophobic interactions with nearby residues including TRP211, ILE136, PRO137, LEU214, TYR211, ARG119, TRP127, and ALA133. Hydrogen bonding (cyan sticks) occurs between the phenolic oxygen of monastrol and ARG119 as well as between a nitrogen of monastrol and GLY117.

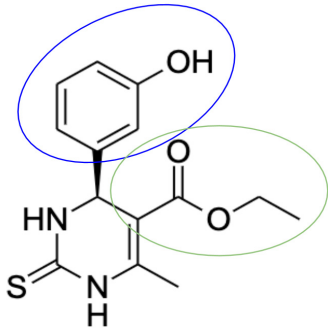

Figure 2: Structure of the S-enantiomer of monastrol, highlighting the 3-hydroxyphenyl aryl (circled in blue) and ethyl ester (circled in green) groups. We modified these circled aryl and ester functionalities during the high throughput virtual screening process to create 100 novel dihydropyrimidine analogs using the molecular editor software Avogadro. We created and edited this chemical structure using ChemDraw.

The best analogs depicted by the Swissdock computations were those with the decyl and geranyl ester substitutions (T1-T20), as indicated by the common trend of ΔG values being less than -8 kcal/mol. As these analogs reported the most negative ΔG values, there were increased amounts of energy released in the exothermic processes, forming comparatively more stable protein-ligand complexes than the other analogs.

Our results also revealed that the analogs R1-R20 consisting of phenoxyethyl and butoxyethyl ester substitutions exhibited relatively high binding affinities too, with the majority of analogs having ΔG values less than -8 kcal/mol. The analogs that had the least binding affinities and resulted in the most positive ΔG values were analogs AR1-AR20, which consisted of methyl and ethyl ester substitutions. With the decyl, geranyl, phenoxyethyl, and butoxyethyl analogs possessing greater amounts of carbon in the ester group than the methyl and ester analogs, the data suggests that the magnitude of ΔG values increases with additional carbons attached to the growing ester chain.

With a ΔG of -8.71 kcal/mol, T18 (which consisted of geranyl ester and 2-nitro aryl substitutions) exhibited the greatest binding affinity to the kinesin Eg5 receptor (Figure 4). When docked to Eg5, T18 presented a binding energy that was 1.40 kcal/mol greater than the control binding affinity of monastrol as computationally determined by Swissdock, a significant difference especially compared to the other analogs with various ester substitutions. The structure-activity relationship of this analog as computed by Swissdock suggests a higher likelihood of exhibiting a greater biological

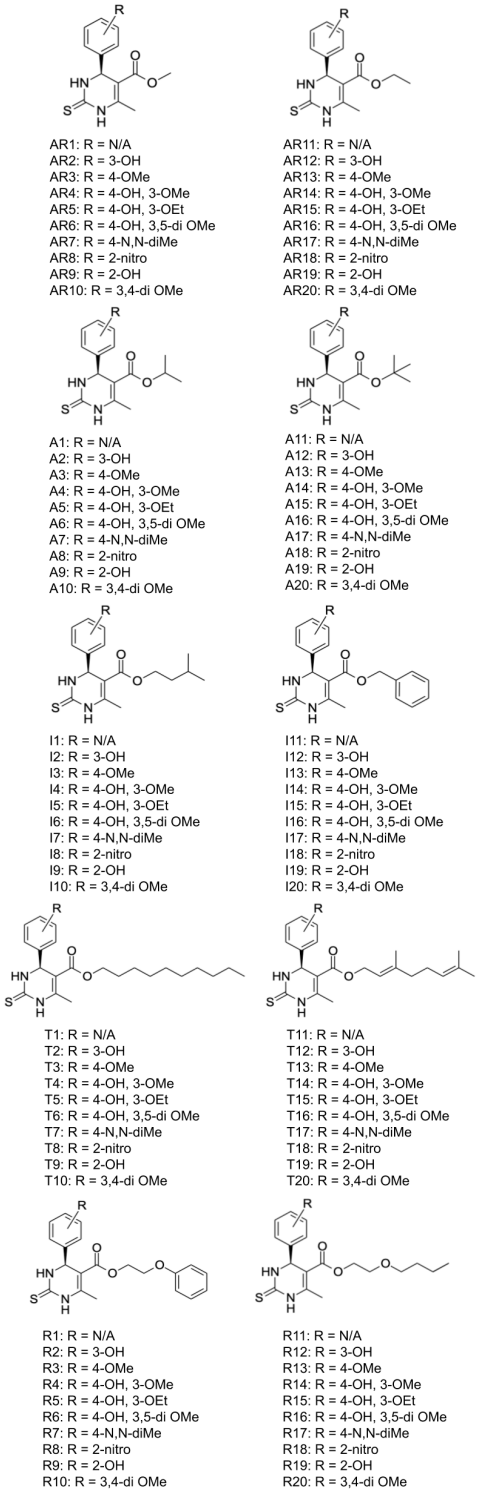

Figure 3: The 100 DHPM analogs with selected ester and aryl substitutions for the S-enantiomer of monastrol. The ester substitutions we made include methyl, ethyl, isopropyl, tert-butyl, isoamyl, benzyl, decyl, geranyl, phenoxyethyl, and butoxyethyl functional groups. The aryl substitutions that we made include phenyl, 3-hydroxy, 4-methoxy, 4-hydroxy-3-methoxy, 4-hydroxy-3-methoxy, 4-hydroxy-3,5-dimethoxy, 4-N,N-dimethylamino, 2-nitro, 2-hydroxy, and 3,4-dimethoxy functional groups. We created the chemical structures and the detailed aryl substitution text using ChemDraw.

potency than the other molecules. Conversely, with methyl ester and phenyl substitutions as well as a ΔG of -6.98 kcal/mol, we discovered that AR1 was the analog with the lowest binding affinity to kinesin Eg5 (Figure 5); when computed by Swissdock, the binding affinity of AR1 was 0.33 kcal/mol less than that of monastrol, indicating an even weaker interaction with kinesin Eg5 than the control.

We then used the Docking Incrementally (DINC) protein ligand docking software to conduct the next series of computational docking experiments. We docked each analog onto the same receptor of kinesin Eg5 using the appropriate grid box coordinates, with the center of the grid box having coordinates of (21.738, 26.509, 51.081) and the grid box dimensions being (40, 44, 40). The thermodynamic results for each analog are documented in Table 1. Again, as AR12 has the same chemical structure as monastrol, we compared each of the DINC binding energies for the other 99 analogs against the control ΔG value of -6.0 kcal/mol.

We color coded each of these values using the same set of ΔG critical values as in the Swissdock experiments. However, the DINC results depicted an overall diminished magnitude of ΔG values in comparison to the Swissdock thermodynamic outputs. Similar to the Swissdock results, analogs T11-20 were the most thermodynamically efficient binders, indicating once again that the analogs with the highest binding affinities were those with the geranyl ester substitutions. In contrast to Swissdock, however, the analogs with decyl ester substitutions (T1-T10) docked with DINC did not reveal substantial binding affinities. The R1-10 analogs containing phenoxyethyl ester substitutions displayed a similar trend of greater ΔG values with DINC in comparison to the other analogs, suggesting that these are also potential lead compounds that should be synthesized and biologically tested. The most unsuccessful binders were overall seen again to be AR1-20, the analogs with methyl and ethyl ester substitutions.

With geranyl ester and 4-hydroxy-3,5-dimethoxy aryl substitutions, we determined T16 as the most thermodynamically effective binder as it exhibited a ΔG value of -8.3 kcal/mol (Figure 6); the binding affinity for T16 was 2.3 kcal/mol greater than the control binding energy of monastrol determined using DINC. This again suggests how the geranyl ester functionality serves a key role in the strengthened binding to kinesin Eg5 and indicates a possible greater biological potency than the other analogs. With a ΔG value of -5.5 kcal/mol, we discovered that AR16 (which consisted of ethyl ester and 4-hydroxy-3,5-dimethoxy aryl substitutions) was the analog with the lowest binding affinity to kinesin Eg5 (Figure 7); the binding affinity of AR16 was 0.4 kcal/mol less than that of monastrol when calculated with DINC, indicating even weaker interactions with kinesin Eg5 than the control.

Following the molecular docking of the analogs using Swissdock and DINC, we employed the OSIRIS Property Explorer to determine the calculated logarithm of the partition coefficient (cLogP) for each analog and evaluate the relative

Analog Name	DINC	DINC: Difference with Monastrol	Swissdock	Swissdock: Difference with Monastrol	cLogP Value	Analog Name	DINC	DINC: Difference with Monastrol	Swissdock	Swissdock: Difference with Monastrol	cLogP Value
AR1	-5.8	0.2	-6.98	0.33	1.66	AR11	-6.1	-0.1	-7.14	0.17	2.07
AR2	-5.8	0.2	-7.37	-0.06	1.32	AR12	-6	0	-7.31	0	1.72
AR3	-5.8	0.2	-7.36	-0.05	1.59	AR13	-5.7	0.3	-7.57	-0.26	2
AR4	-5.8	0.2	-7.29	0.02	1.25	AR14	-6.2	-0.2	-7.78	-0.47	1.65
AR5	-6	0	-7.84	-0.53	1.65	AR15	-6.2	-0.2	-7.56	-0.25	2.34
AR6	-5.6	0.4	-7.42	-0.11	1.18	AR16	-5.5	0.5	-7.66	-0.35	1.58
AR7	-5.7	0.3	-7.4	-0.09	1.56	AR17	-6	0	-7.33	-0.02	1.97
AR8	-6.1	-0.1	-7.56	-0.25	0.74	AR18	-6.1	-0.1	-7.88	-0.57	1.15
AR9	-5.8	0.2	-7.08	0.23	1.32	AR19	-5.9	0.1	-7.05	0.26	2.06
AR10	-5.6	0.4	-7.7	-0.39	0.97	AR20	-5.6	0.4	-7.73	-0.42	1.93
A1	-6	0	-7.14	0.17	2.43	A11	-6.4	-0.4	-7.32	-0.01	2.81
A2	-6.1	-0.1	-7.53	-0.22	2.08	A12	-6.4	-0.4	-7.63	-0.32	2.46
A3	-6.2	-0.2	-7.45	-0.14	2.36	A13	-6.3	-0.3	-7.42	-0.11	2.74
A4	-5.7	0.3	-7.76	-0.45	2.01	A14	-6.2	-0.2	-7.63	-0.32	2.39
A5	-6.1	-0.1	-7.57	-0.26	2.42	A15	-6.5	-0.5	-7.78	-0.47	2.8
A6	-5.8	0.2	-7.57	-0.26	1.94	A16	-5.7	0.3	-8.03	-0.72	2.32
A7	-6.3	-0.3	-7.3	0.01	2.32	A17	-6.4	-0.4	-7.54	-0.23	2.71
A8	-6.3	-0.3	-7.55	-0.24	1.51	A18	-6.7	-0.7	-7.58	-0.27	1.89
A9	-6.3	-0.3	-7.6	-0.29	2.06	A19	-6.5	-0.5	-7.38	-0.07	2.46
A10	-5.7	0.3	-7.76	-0.45	2.29	A20	-5.9	0.1	-7.82	-0.51	2.67
I1	-6.8	-0.8	-7.36	-0.05	3.2	I11	-6.5	-0.5	-7.53	-0.22	3.08
I2	-6.8	-0.8	-7.6	-0.29	2.85	I12	-6.8	-0.8	-7.58	-0.27	2.73
I3	-7	-1	-7.67	-0.36	3.13	I13	-7.3	-1.3	-7.74	-0.43	3.01
I4	-7	-1	-7.78	-0.47	2.78	I14	-6.2	-0.2	-7.59	-0.28	2.67
I5	-7.2	-1.2	-7.86	-0.55	3.19	I15	-6.7	-0.7	-7.75	-0.44	3.07
I6	-6.3	-0.3	-7.91	-0.6	2.71	I16	-6.3	-0.3	-8.03	-0.72	2.59
I7	-6.3	-0.3	-7.84	-0.53	3.09	I17	-6.2	-0.2	-7.88	-0.57	2.98
I8	-7	-1	-8.04	-0.73	2.27	I18	-7.7	-1.7	-7.97	-0.66	2.16
I9	-7.1	-1.1	-7.65	-0.34	2.85	I19	-7.7	-1.7	-7.91	-0.6	2.73
I10	-6.3	-0.3	-8	-0.69	3.06	I20	-6.2	-0.2	-7.84	-0.53	2.94
T1	-7.1	-1.1	-8.3	-0.99	5.7	T11	-7.4	-1.4	-8.29	-0.98	5.5
T2	-6.9	-0.9	-8.25	-0.94	5.36	T12	-7.7	-1.7	-8.23	-0.92	5.16
T3	-6.9	-0.9	-8.35	-1.04	5.63	T13	-8.1	-2.1	-8.29	-0.98	5.43
T4	-6.9	-0.9	-8.11	-0.8	5.29	T14	-7.3	-1.3	-8.41	-1.1	5.09
T5	-6.4	-0.4	-8.12	-0.81	5.69	T15	-8.1	-2.1	-8.62	-1.31	5.49
T6	-6.8	-0.8	-8.63	-1.32	5.22	T16	-8.3	-2.3	-8.46	-1.15	5.02
T7	-6.9	-0.9	-8.17	-0.86	5.6	T17	-8.1	-2.1	-8.31	-1	5.4
T8	-6.8	-0.8	-8.25	-0.94	4.78	T18	-8.1	-2.1	-8.71	-1.4	4.58
T9	-7.1	-1.1	-8.16	-0.85	5.36	T19	-7.5	-1.5	-8.1	-0.79	5.16
T10	-6.7	-0.7	-8.56	-1.25	5.56	T20	-7.6	-1.6	-8.33	-1.02	5.36
R1	-7.4	-1.4	-8.13	-0.82	3.09	R11	-7	-1	-7.8	-0.49	2.89
R2	-7.5	-1.5	-8.09	-0.78	2.74	R12	-7.1	-1.1	-8.08	-0.77	2.54
R3	-7.4	-1.4	-7.87	-0.56	3.02	R13	-6.6	-0.6	-8.1	-0.79	2.82
R4	-7.6	-1.6	-8.07	-0.76	2.67	R14	-7.6	-1.6	-8.22	-0.91	2.47
R5	-7.8	-1.8	-8.36	-1.05	3.08	R15	-7.6	-1.6	-8.4	-1.09	2.88
R6	-7.4	-1.4	-8.43	-1.12	2.6	R16	-6.9	-0.9	-8.23	-0.92	2.4
R7	-7.3	-1.3	-8.69	-1.38	2.96	R17	-6.9	-0.9	-8.1	-0.79	2.78
R8	-8	-2	-8.14	-0.83	2.17	R18	-7.3	-1.3	-7.73	-0.42	1.96
R9	-7.3	-1.3	-7.92	-0.61	2.74	R19	-7.1	-1.1	-8.08	-0.77	2.54
R10	-7.6	-1.6	-8.12	-0.81	2.95	R20	-6.7	-0.7	-8.13	-0.82	2.75

	ΔG less than -8.00 kcal/mol
	ΔG between -7.00 and -7.99 kcal/mol
	ΔG between -6.00 and -6.99 kcal/mol
	ΔG less than -5.99 kcal/mol

Table 1: A heatmap of DINC and Swissdock results color-coded based on the calculated ΔG value. We docked each analog (entitled AR1, AR2, etc.) onto the human kinesin Eg5 protein, with the pose of the most negative binding affinity selected. For each analog, there exists the DINC binding affinity value, the difference in binding affinity (using DINC) between the modeled analog and monastrol, the Swissdock binding affinity value, the difference in binding affinity (using Swissdock) between the modeled analog and monastrol, and the cLogP value for each analog calculated through the OSIRIS Property Explorer. The ΔG values from the DINC results are overall more positive than those attained using Swissdock.

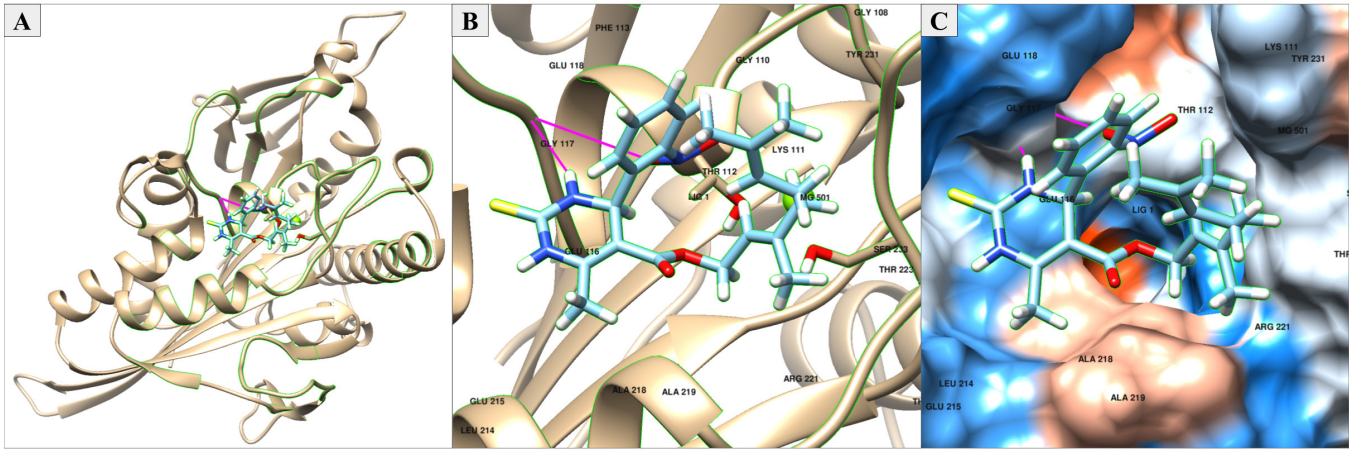

Figure 4: Swissdock results for the T18 analog. (A) The docked structure of the ligand with the highest binding affinity (T18) according to the Swissdock ΔG values obtained using UCSF Chimera, with a ΔG value of -8.71 kcal/mol. The cyan structure is the T18 analog, while the gold structure is the human kinesin Eg5 protein. (B) A detailed visualization of the protein-ligand interaction in the binding pocket, with significant hydrophobic interactions and two hydrogen bonds (magenta) occurring within 4.0 angstroms of the ligand. (C) A hydrophobicity surface model is depicted, with hydrophobic interactions (red), hydrophilic interactions (white), and neutral interactions (white) shown between T18 and the amino acid residues within the loop5/α2/α3 allosteric binding site.

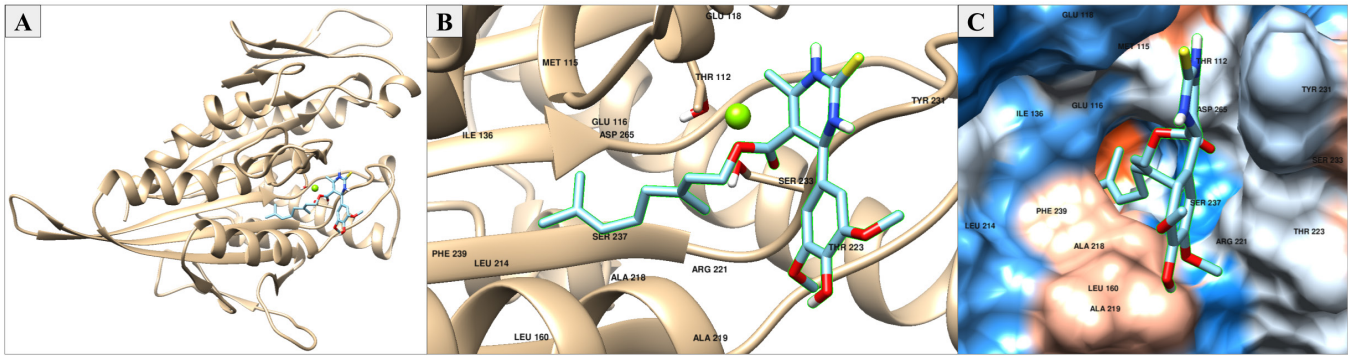

Figure 5: Swissdock results for the AR1 analog. (A) The docked structure of the ligand with the lowest binding affinity (AR1) according to the Swissdock ΔG values obtained using UCSF Chimera, with a ΔG value of -6.98 kcal/mol. The cyan structure is the AR1 analog, while the gold structure is the human kinesin Eg5 protein. (B) A detailed visualization of the protein-ligand interaction in the binding pocket, with hydrophobic interactions, hydrophilic interactions, and hydrogen bonding (magenta) occurring within 4.0 angstroms of the ligand. (C) A hydrophobicity surface model is depicted, with hydrophobic interactions (red), hydrophilic interactions (white), and neutral interactions (white) shown between AR1 and the amino acid residues within the loop5/α2/α3 allosteric binding site.

amount of hydrophobic interactions that each could engage in. We documented the cLogP value for each analog in Table 1. All of the constructed dihydropyrimidine analogs exhibited positive cLogP values, indicating a tendency for these molecules to have hydrophobic cores. We compared these molecules to the control cLogP value (AR12) of 1.72 to indicate the relative extent of hydrophobic interactions occurring in the binding pocket. With cLogP values all greater than 4.58, T1-20 (the decyl and geranyl analogs) exhibited the highest values compared to the other analogs, indicating that these molecules had the most substantial hydrophobicities. T18, the analog with the greatest binding affinity discovered through Swissdock, demonstrated a cLogP value of 4.58, which was greater than that of monastrol by 2.86. Though this factor of 2.86 may not initially resemble a statistically significant difference, it is important to note that the partition coefficients have been logarithmically transformed; thus, an increase in cLogP of 2.86 is actually an increase in hydrophobicity by a magnitude of 102.86. Similarly, we calculated T16, the analog with the greatest binding affinity discovered through DINC, as having a cLogP value of 5.02, which was greater than that of monastrol by 3.30. In the analysis of the molecules with the lowest binding affinities determined by Swissdock and DINC, we discovered that AR1 and AR16 displayed cLogP values of 1.66 and 1.58 respectively, representing diminished potentials to bind hydrophobically with kinesin Eg5 than even monastrol itself. In combination with the corroborating data indicating that the geranyl analogs had the greatest binding affinities, we presumed that improved binding to the receptor of the kinesin Eg5 protein is based on greater inherent abilities for strong hydrophobic interactions to occur between the dihydropyrimidine molecule and the protein.

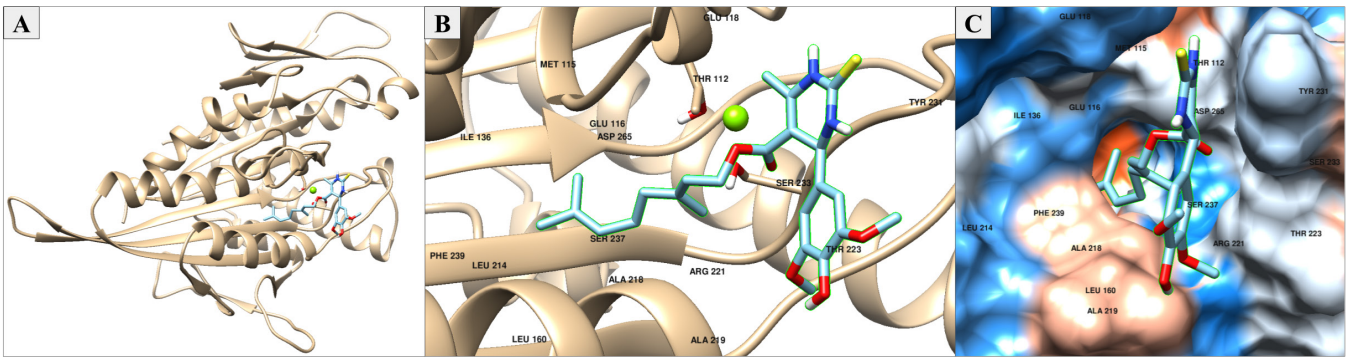

Figure 6: DINC results for the T16 analog. (A) The docked structure of the ligand with the highest binding affinity (T16) according to the DINC ΔG values obtained using UCSF Chimera, with a ΔG value of -8.3 kcal/mol. The cyan structure is the T16 analog, while the gold structure is the human kinesin Eg5 protein. (B) A detailed visualization of the protein-ligand interaction in the binding pocket, with significant hydrophobic interactions occurring within 4.0 angstroms of the ligand. (C) A hydrophobicity surface model is depicted, with hydrophobic interactions (red), hydrophilic interactions (white), and neutral interactions (white) shown between T16 and the amino acid residues within the loop5/α2/α3 allosteric binding site.

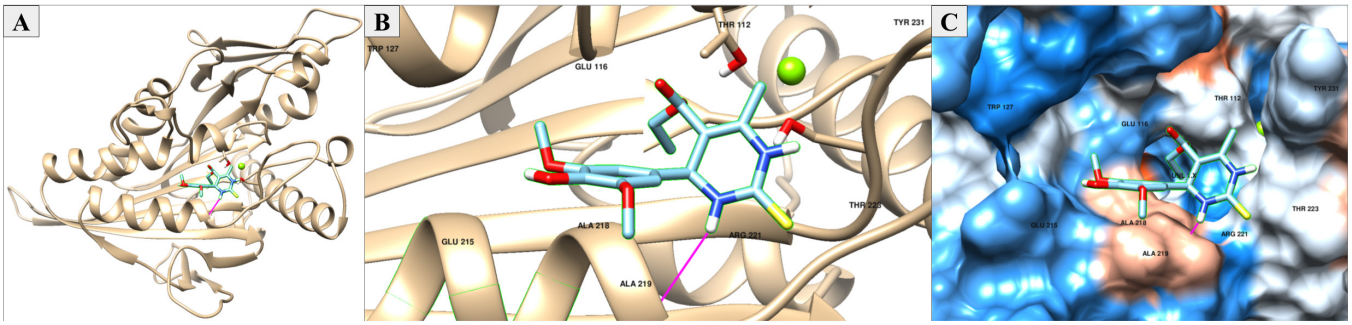

Figure 7: DINC results for the AR16 analog. (A) The docked structure of the ligand with the lowest binding affinity (AR16) according to the DINC ΔG values obtained using UCSF Chimera, with a ΔG value of -5.5 kcal/mol. The cyan structure is the AR16 analog, while the gold structure is the human kinesin Eg5 protein. (B) A detailed visualization of the protein-ligand interaction in the binding pocket, with hydrophilic interactions, hydrophobic interactions and hydrogen bonding (magenta) occurring within 4.0 angstroms of the ligand. (C) A hydrophobicity surface model is depicted, with hydrophobic interactions (red), hydrophilic interactions (white), and neutral interactions (white) shown between AR16 and the amino acid residues within the loop5/α2/α3 allosteric binding site.

DISCUSSION

While the ΔG values given by each docking algorithm were slightly different, a common trend emerged in the role of specific functionalities in binding affinity. As seen from the strongly negative ΔG values calculated by Swissdock and DINC, the geranyl ester substitution analogs were the best binders to kinesin Eg5, likely due to the characteristic ability of nonpolar geranyl groups for increased hydrophobic interactions with the binding pocket. All of the geranyl analogs displayed relatively high cLogP values (all greater than 4.58) when compared to the cLogP values of other analogs with varying ester substitutions; this confirmed the great amount of hydrophobic interactions that the geranyl analogs have the potential to engage in within the binding pocket.

The Swissdock results also indicated that the decyl analogs were particularly effective binders to kinesin Eg5 as they also exhibited strong negative ΔG values. Because of the heightened nonpolar abilities of the decyl group, we presumed that this ester functionality leads to stronger hydrophobic interactions to occur during protein-ligand binding. The specific interactions between the amino acid residues of the receptor and the decyl analogs can again be attributed to strong hydrophobic interactions as suggested by the high cLogP values (all greater than 4.78) calculated for each molecule.

Both Swissdock and DINC results corroborated the methyl and ethyl analogs as the worst binders to kinesin Eg5 as indicated by the least negative ΔG values. With the cLogP values calculated for these analogs relatively low (all less than 2.34) compared to analogs with other ester substitutions, the results suggested that the diminished hydrophobicities of the methyl and ethyl groups correlate with weaker intermolecular interactions during binding.

In the binding pocket analysis of T18, the analog with the greatest binding affinity according to Swissdock, we discovered the molecule engaging in hydrophobic interactions and hydrogen bonding with kinesin Eg5. Given that the aliphatic tail was in close proximity (within 4.0 angstroms) to the hydrophobic LEU214, ALA218, ALA219, GLY110, GLY117, PHE113, and TYR231 residues, it suggested there exists a high level of hydrophobic interactions between the ligand and receptor (Figure 4). Additionally, two hydrogen bonds occurred

between T18 and GLY117, as indicated by the magenta bonds in Figure 4B. The strong hydrophobic interactions (in red) with the aforementioned leucines, alanines, glycines, phenylalanines, and tyrosines in the binding pocket can be visualized in Figure 4C, confirming the high hydrophobicity of T18 denoted by the cLogP value of 4.58.

Though we noticed that AR1 (the analog with the lowest binding affinity according to Swissdock) also engaged in hydrophobic interactions and hydrogen bonding, we discovered substantial hydrophilic interactions in the binding pocket too. While T18 hydrogen bonded with GLY117, a hydrogen bond instead occurred between AR1 and GLU118, as indicated in Figure 5. As the aliphatic tail was verified to be in close proximity to the hydrophobic LEU214, LEU171, GLY117, GLY217, ALA218, ALA219, and TYR231 residues, it established that hydrophobic interactions did occur to a small extent between the ligand and receptor (Figure 5B). However, upon closer examination of the hydrophobicity surface in Figure 5C, we distinguished that a significant number of hydrophilic residues (in blue) of kinesin Eg5 including ARG119, ARG221, TRP127, GLU116, and GLU118 also interacts with the ligand, likely resulting in its decreased binding affinity. The increased amount of visualized hydrophilic interactions confirmed the weakly hydrophobic nature of AR1 implied by the cLogP value of 1.66.

Similar to the analysis of T18, we discovered that T16 (the analog with the greatest binding affinity according to DINC) also engaged in substantial hydrophobic interactions with kinesin Eg5 as the aliphatic tail was in close proximity to the hydrophobic ALA218, ALA219, TYR231, PHE239, LEU160, LEU214, MET115, and ILE136 residues (Figure 6). These strong hydrophobic interactions with the aforementioned amino acids in the binding pocket can be visualized in Figure 6C, confirming the high hydrophobicity indicated by the T16 cLogP value of 5.02.

In the binding pocket analysis of AR16, the analog with the lowest binding affinity according to DINC, we again discovered that although the molecule did engage in hydrophobic interactions, a considerable amount of hydrogen bonding and hydrophilic interactions occurred. As seen in Figure 7, a hydrogen bond was visualized between AR16 and ALA219. Given that the aliphatic tail was in close proximity to the hydrophobic ALA218, ALA219, and TYR231 residues, it suggested that minimal hydrophobic interactions occurred between the ligand and receptor (Figure 7B). However, a detailed inspection of the hydrophobicity surface in Figure 7C revealed a significant number of hydrophilic regions including TRP127, GLU116, GLU215, ARG221, THR112, and THR223 interacting with the ligand, likely causing its decreased binding affinity. These increased amounts of visualized hydrophilic interactions confirmed the diminished hydrophobicity of AR16 as denoted by the cLogP value of 1.58.

A possibility for the inconsistent values between the DINC and Swissdock thermodynamic outputs is the unique computational algorithms implemented by each software in the calculation of binding poses and energies. DINC is generally used for larger ligands, which could explain possible inaccuracies in binding affinities when compared to those outputted by Swissdock. With the algorithms executed by Swissdock generally used for smaller ligands like monastrol, these values are more likely to be accurate and closer to the actual experimentally derived binding affinities. However, the overall trends of binding affinities for the ester substitutions were relatively consistent, particularly with the indication that the geranyl analogs were lead compounds that should be synthesized and biologically screened while the methyl and ethyl analogs should not. Future studies using high-throughput virtual screening could employ the use of alternative molecular docking software packages to examine other binding affinity differences with varying algorithms and computations.

With molecular docking, most of the interactions are entropy-driven as two separate entities of the ligand and the receptor bind together to form a single protein-ligand complex. This previously rotatable and flexible entity is now constrained with the attractions in the binding pocket, resulting in an entropic penalty to occur with fewer microstates. Due to the docking algorithms used per software, we were unable to ascertain the relative entropic and enthalpic contributions; the final configurations are a combination of the two different factors, though the overall binding pose analysis should rely primarily on entropic interactions. Additionally, these simulations can only provide insight into the binding thermodynamics and not the binding kinetics, representing another limitation with this technique.

Further computational experiments that could be performed in the future to verify the importance of the side group modifications on the monastrol analogs include molecular dynamics simulations. These simulations could provide insight into the effects of binding on the time-resolved behavior of the binding site. Particularly, conducting molecular dynamics simulations for the top geranyl compounds discovered could provide further analysis into how binding affects the movement of the active site.

The increased binding affinities and high cLogP values of the geranyl analogs screened in this study suggests that hydrophobic interactions of the ester functionality are key in the binding of dihydropyrimidine monastrol analogs to the allosteric binding pocket of Eg5. These are potential leads in the development of potent Eg5 inhibitors, and the creation of new analogs with these nonpolar functionalities could potentially yield anticancer molecules with greater antiproliferative properties than monastrol itself. Future high-throughput virtual screening studies conducted with monastrol and dihydropyrimidine analogs should focus on the substitution of the ester functionality in favor of other side chains with increased hydrophobic properties. The QSAR uncovered by our high-throughput virtual screening efforts informs the future chemical synthesis of geranyl analogs with greater potency and biological activity. Using high-throughput

virtual screening to design, discover, and analyze effective small molecule Eg5 inhibitors has the potential to advance humanity's efforts in combating cancer and revolutionize the available treatments for this family of deadly diseases.

MATERIALS AND METHODS

Avogadro

Each analog to be screened was constructed virtually on Avogadro (version 1.2.0), an open access three-dimensional molecular editing and visualization software for use in the modeling of molecular compounds (12). Following the construction of each analog, an initial molecular mechanics geometry optimization was performed. This preprocessing step for the ligands allowed for a basic adjustment of human error when constructing the molecules, especially in terms of correcting the bond lengths and bond angles associated with each molecular geometry and bond type.

ORCA

To identify the ideal binding pose, we first determined the most quantum mechanically favorable geometry for each analog using DFT molecular geometry optimizations, which were conducted using ORCA (version 4.2.0), an ab initio quantum mechanical molecular modeling software (13). In order to run these geometric optimization calculations, input files for each structure suited for ORCA were generated by Avogadro. To simulate the aqueous environment in which monastrol binds to kinesin Eg5 in the human body, we used a conductor-like polarizable continuum (CPCM) solvation model. This was an implicit solvation model, which treated the solvent environment as a continuous medium with a particular dielectric and polarizability rather than individual, explicitly defined solvent molecules. A B3LYP hybrid functional and def2-SVP basis set were chosen. The DFT calculations were all conducted on a MacBook Pro with a 2.3 GHz Intel Core i5 processor, 4 cores, 8 GB of RAM, and 512 GB of flash storage, with each calculation running for an estimated 15 minutes. After computing the atomic positions in the most quantum mechanically stable states through submission of the input files into ORCA, the analogs were prepared for protein-ligand docking.

Molecular Docking

Molecular docking was used to predict the binding affinities of ligands bound to particular targets on the basis of specific thermodynamic factors that contribute to and detract from the free energy of interaction between the target and ligand. These factors include noncovalent interactions such as electrostatic attraction and repulsion, pi-stack interactions, hydrophobic interactions, and hydrogen bonding networks. The docking outputs were visualized on UCSF Chimera (version 1.13.1) (14). By observing the binding pocket of monastrol itself to the human motor protein kinesin Eg5 (PDB: 1X88), we were able to determine the appropriate grid box center and dimensions at which to bind the rest of our analogs by calculating the atomic distances between the kinesin protein and monastrol using UCSF Chimera. The center of the grid box was calculated as having coordinates of (21.738, 26.509, 51.081) and the grid box dimensions were determined to be (40, 44, 40), which provided a detailed specification of the proper allosteric binding site for ligand docking. This grid box covered the entirety of the ligand and only the observed allosteric binding pocket of the kinesin Eg5 protein. As we used the crystal structure of the kinesin Eg5 protein (PDB: 3HQD) as determined by X-ray diffraction for the docking of the analogs, no further preprocessing steps beyond the specification of the grid box were required for the protein prior to docking with both Swissdock and DINC (15). The quantum mechanically optimized ligand structures from the DFT calculations were then docked into the processed kinesin Eg5 protein. The docking software used generated a list of binding poses with different binding affinities; for the purpose of this study, we selected the highest calculated binding affinity to be the representative value for each compound, and alternative poses were not factored into the QSAR.

Swissdock

Swissdock, developed by the Swiss Institute of Bioinformatics, is a web-based server for molecular docking that utilizes an algorithm generating binding modes in the vicinity of a localized target cavity (16). Using their potential energies, binding modes with the most favorable energy values are analyzed and clustered, which can be viewed on the server or on other molecular visualization softwares. In this study, we docked each of the novel analogs into the allosteric binding pocket of human kinesin Eg5 (PDB: 3HQD) using the previously determined grid box coordinates to obtain the predicted binding affinities. Swissdock outputted varying conformations of the ligand on the receptor based on different binding modes with the most favorable energies clustered together. The predicted ΔG value of each dihydropyrimidine analog to Eg5 was reported in kcal/mol and represented the binding affinity of the ligand.

Docking Incrementally

Docking Incrementally (DINC), originally developed by the Kavraki Lab, was the second docking software used to computationally dock the analogs (17). DINC (version 2.0) uses a meta-docking algorithm called AutoDock Vina, another docking software which predicts thermodynamically favorable interactions between small molecule ligands and protein targets (17). DINC treated the ligand as a superposition of a rigid body component and a single rotatable component and was chosen to more accurately model the kinesin-ligand system, since many of our analogs had a large number of rotatable bonds. Each single partial solution was overlapped as a fragment until the entire ligand had been reconstructed. In this study, the analogs were docked into the allosteric binding pocket of kinesin Eg5 (PDB: 3HQD) using the aforementioned grid box coordinates to determine the predicted binding

affinities.

OSIRIS Property Explorer - cLogP Calculations

With monastrol known to interact with the allosteric binding pocket through hydrophobic interactions, we also sought to investigate the degree of hydrophobicity of our dihydropyrimidine analogs to provide a QSAR. Using the OSIRIS Property Explorer on the Organic Chemistry Portal, cLogP values, the logarithms of the partition coefficient between water and n-octanol for a given compound, were calculated to provide insight on the hydrophilicity of each analog (18). Negative cLogP values indicated greater hydrophilic properties of the molecule, while positive cLogP values indicated greater hydrophobic properties. Molecules with large, positive cLogP values were considered to have high hydrophobicities and this result indicated a greater affinity of the analog for stronger hydrophobic interactions in the binding pocket. Binding affinities and cLogP values were subsequently analyzed for emerging trends linking hydrophobicity and improved binding to kinesin Eg5. Additionally, we assumed differences in the cLogP values per analog to be solely due to the aliphatic side chain or aromatic substitutions.

Binding Pocket Analysis

Using UCSF Chimera to visualize the molecular docking results, the binding pocket in which the dihydropyrimidine analogs were docked was closely examined and analyzed. With typical hydrogen bonds having a bond distance between 2.4-3.5 angstroms, hydrophobic interactions having a bond distance between 3.3-4.0 angstroms, and pi-stack interactions having a bond distance between 3.3-3.8 angstroms, only amino acid residues specified within 4.0 angstroms of the docked ligand were considered to be taking part in potential non-covalent interactions (19, 20, 21). These amino acid residues were then analyzed for various properties that could have explained the calculated binding affinities on both Swissdock and DINC, with a particular focus on hydrophobic surfaces due to the significant amount of hydrophobic interactions monastrol engages in with kinesin Eg5.

REFERENCES

1. Siegel, Rebecca L., et al. “Cancer Statistics, 2019.” CA: A Cancer Journal for Clinicians, vol. 69, no. 1, 2019, pp. 7–34., doi:10.3322/caac.21551.
2. Simon, Stacy. “Facts & Figures 2019: US Cancer Death Rate Has Dropped 27% in 25 Years.” American Cancer Society, American Cancer Society, 2019, www.cancer.org/latest-news/facts-and-figures-2019.html.
3. Mayer, T. U. “Small Molecule Inhibitor of Mitotic Spindle Bipolarity Identified in a Phenotype-Based Screen.” Science, vol. 286, no. 5441, 1999, pp. 971–974., doi:10.1126/science.286.5441.971.
4. Liu, Min, et al. “Non-Canonical Functions of the Mitotic Kinesin Eg5.” Thoracic Cancer, vol. 9, no. 8, 2018, pp. 904–910., doi:10.1111/1759-7714.12792.
5. Wang, Yufei, et al. “Eg5 Inhibitor YL001 Induces Mitotic Arrest and Inhibits Tumor Proliferation.” Oncotarget, vol. 8, no. 26, 2017, pp. 42510–42524., doi:10.18632/oncotarget.17207.
6. Gonçalves, Itamar Luís, et al. “Effect of N-1 Arylation of Monastrol on Kinesin Eg5 Inhibition in Glioma Cell Lines.” MedChemComm, vol. 9, no. 6, 2018, pp. 995–1010., doi:10.1039/c8md00095f.
7. Kapoor, Tarun M., et al. “Probing Spindle Assembly Mechanisms with Monastrol, a Small Molecule Inhibitor of the Mitotic Kinesin, Eg5.” Journal of Cell Biology, vol. 150, no. 5, 2000, pp. 975–988., doi:10.1083/jcb.150.5.975.
8. Guido, Bruna C, et al. “Impact of Kinesin Eg5 Inhibition by 3,4-Dihydropyrimidin-2(1H)-One Derivatives on Various Breast Cancer Cell Features.” BMC Cancer, vol. 15, no. 1, 2015, doi:10.1186/s12885-015-1274-1.
9. Myers, Stephanie M, and Ian Collins. “Recent Findings and Future Directions for Interpolar Mitotic Kinesin Inhibitors in Cancer Therapy.” Future Medicinal Chemistry, vol. 8, no. 4, 2016, pp. 463–489., doi:10.4155/fmc.16.5.
10. Maliga, Zoltan, et al. “Evidence That Monastrol Is an Allosteric Inhibitor of the Mitotic Kinesin Eg5.” Chemistry & Biology, vol. 9, no. 9, 2002, pp. 989–996., doi:10.1016/s1074-5521(02)00212-0.
11. Pagadala, Nataraj S., et al. “Software for Molecular Docking: a Review.” Biophysical Reviews, vol. 9, no. 2, 2017, pp. 91–102., doi:10.1007/s12551-016-0247-1.
12. Hanwell, Marcus D, et al. “Avogadro: an Advanced Semantic Chemical Editor, Visualization, and Analysis Platform.” Journal of Cheminformatics, vol. 4, no. 1, 2012, doi:10.1186/1758-2946-4-17.
13. Neese, Frank. “The ORCA Program System.” WIREs Computational Molecular Science, vol. 2, no. 1, 2011, pp. 73–78., doi:10.1002/wcms.81.
14. Pettersen, Eric F., et al. “UCSF Chimera? A Visualization System for Exploratory Research and Analysis.” Journal of Computational Chemistry, vol. 25, no. 13, 2004, pp. 1605–1612., doi:10.1002/jcc.20084.
15. Parke, Courtney L., et al. “ATP Hydrolysis in Eg5 Kinesin Involves a Catalytic Two-Water Mechanism.” Journal of Biological Chemistry, vol. 285, no. 8, 2009, pp. 5859–5867., doi:10.1074/jbc.m109.071233.
16. Grosdidier, A., et al. “SwissDock, a Protein-Small Molecule Docking Web Service Based on EADock DSS.” Nucleic Acids Research, vol. 39, 2011, doi:10.1093/nar/gkr366.
17. Antunes, Dinler A., et al. “DINC 2.0: A New Protein–Peptide Docking Webserver Using an Incremental Approach.” Cancer Research, vol. 77, no. 21, 2017, doi:10.1158/0008-5472.can-17-0511.
18. Sander, Thomas. “CLogP Calculation.” Organic Chemistry, www.organic-chemistry.org/prog/peo/cLogP.

html.
19. Berg, Jeremy M., et al. Biochemistry. W.H. Freeman and Co., 2002.
20. Martz, Eric. "Noncovalent Bond Finder." University of Massachusetts, Amherst, 2002, www.umass.edu/microbio/chime/find-ncb/demo_txt.htm.
21. Janiak, Christoph. "A Critical Account on π–π Stacking in Metal Complexes with Aromatic Nitrogen-Containing Ligands." Journal of the Chemical Society, Dalton Transactions, no. 21, 2000, pp. 3885–3896., doi:10.1039/b003010o.

Article submitted: April 22, 2020
Article accepted: September 22, 2020
Article published: December 20, 2020

JOURNAL OF
EMERGING INVESTIGATORS

Article

Evaluation of microplastics in Japanese fish using visual and chemical dissections

Emma Rudy Srebnik, Sarah Urquhart
Yokohama International School, Yokohama, Japan

SUMMARY

Up to 12.7 million tonnes of plastic is estimated to be polluting oceans. Ranking as the fifth-highest plastic using country, Japan has an exceptionally high usage of single wrapped items. Additionally, as an island-nation, fish is vital to everyday life, making up approximately 40% of protein in Japanese diets. Based on these observations, I wondered how the overuse of plastic in Japan poses an ecological risk to marine species and their consumers local to Kanagawa Prefecture. To answer this question, I completed a plastic audit at a convenience store, took qualitative observations of plastic waste at three waterways, and dissected locally sourced fish to characterize ingested plastic. I found 83.4% of the convenience store's items within the recorded sections had plastic wrapping or pieces. Additionally, each waterway observed had both plastic and marine species present. Using visual and chemical dissection, all fish had microplastics present in their gastrointestinal tract, including two species that are typically eaten whole in Japan. Out of the fourteen microplastics found through the chemical digestion method, six were classified as plastic microfibers, four were likely thread plastic, three were see-through pieces of plastic film, and one was a foam pellet. Overall, these results are concerning as previous studies have found that microplastics can carry persistent organic pollutants. Both bioaccumulation and biomagnification result in large levels of contaminants building up at the top of the food chain. It is presumed that the increasing consumption of microplastics will have negative implications on organ systems such as the liver, gut, and hormones.

INTRODUCTION

Plastic contains organic polymers, which allows it to be durable and inexpensive, and results in a wide application of uses. While plastic has been used for hundreds of years, it was not until 1907 that the first completely synthetic plastic was created by Leo Baekeland. Now, over one-hundred years later, plastic is used around the world for thousands of purposes. According to Chemical & Engineering News' (C&EN) data, in 2014, Japan had the second-highest volume of "top 50" plastic producing companies after the United States (1). Approximately one-third of the plastic produced is used for packaging (2).

It is estimated that oceans are filled with up to 12.7 million tonnes of plastic litter, making it the largest area of marine pollution (3). Japan, an island nation, is ranked as the 5th highest plastic-using country, much of which is purely used for aesthetics reasons rather than functional ones (4). The average Japanese shopper uses 300 to 400 single-use plastic bags annually (5), 16 times more than in Britain, also an island-nation (6).

Once plastic is discarded, some of it ends up in recycling centers, but oftentimes a large percentage escapes and makes its way to waterways which leads to the ocean. According to Geyer *et al*., 90.5% of worldwide plastic has never been recycled (7). Additionally, since Japan is on three fault lines, in the case of natural disasters, waste management would halt. This could lead to the release of plastic, as was seen during the March 2011 earthquake.

Marine plastic pollution has been documented as directly impacting 267 species worldwide, including fish, seabirds, and marine mammals (8). Plastic that recently entered the ocean will likely resemble the original design. These large pieces can confuse marine life as it might look like food. Once eaten, larger pieces of plastic can block the organism's gastrointestinal tract since they cannot break it down, eventually causing starvation (8).

At five millimeters or less in length, microplastics are tiny pieces of plastic that can be seemingly non-existent to the eye (9). Microplastics can either be primary or secondary; primary microplastics are originally a small particle size, whereas secondary microplastics are fragments of larger pieces (10). Once larger plastics are exposed to saltwater, UV light, and microbes, they are degraded into these smaller pieces (**Figure 1**).

There are multiple types of microplastics, including microfibers and thread plastic. Microfibers are small pieces of plastic that come off synthetic material, usually during a washing machine cycle. Because microfibers are so small, wastewater treatment centers are unable to filter them out, so the fibers enter the environment. Thread plastic, conversely, often come off nylon ropes or other fishing gear (11). Fishing gear makes up nearly 50% of the Great Pacific Garbage Patch trash, leading thread plastic to be a commonly found microplastic (12).

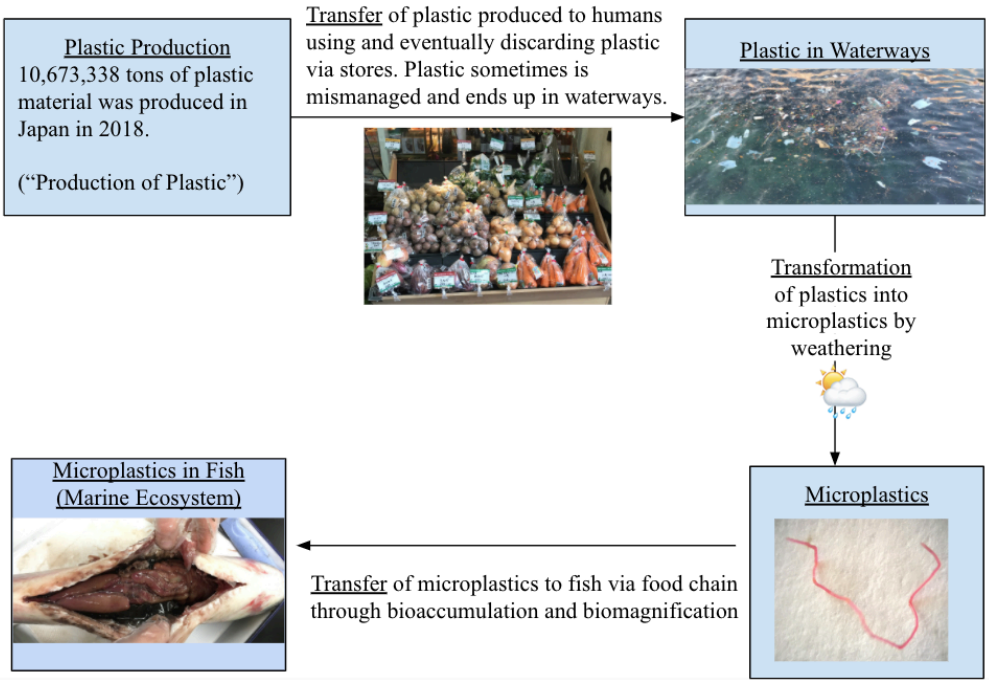

Figure 1. Systems diagram of plastic's movement from production to entrance into marine ecosystems.

Microplastics especially pose a large issue since they can bind to persistent organic pollutants such as pesticides. This binding can increase as microplastics move due to ocean currents (13). If ingested, marine organisms absorb the pollutants which can have a negative impact on their liver, hormones, and gut (11). Both the plastic and pollutants begin bioaccumulating within organisms over time which eventually biomagnifies as it moves up trophic levels. This results in the largest levels of contaminants being present at the top of the food chain.

Ingestion of microplastics often occurs because they resemble plankton, or small organisms that float in the ocean (9). Zooplankton, a primary consumer, were found to accidentally consume microplastics as they are similar in size to phytoplankton. Because zooplankton are near the bottom of the food chain, microplastics accumulate throughout trophic levels until they reach the top of the food chain, where carnivores can be found. This study estimated that humpback whales, which consume 1.5% of their body weight in krill and plankton daily, are ingesting 300,000 microplastic particles every day (14).

Despite humans being estimated at the trophic level 2.2 (out of 5.5) due to an omnivorous diet; we are still predicted to be consuming nearly 2000 microplastic particles weekly. The health implications of this are still unclear (15). However, scientists have found that a certain level of ingested microplastics can cause mild inflammation in the respiratory tract (16).

Fish are a major part of Japanese culinary culture, making up 40% of the protein in their diet. Japanese people eat on average 69.1 kg of fish annually (17). This means the total population (126.8 million people in 2017) consumes about 8.8 million tons of fish annually.

Previous research by Tanaka and Takada (2016) found microplastics present in anchovies from North Tokyo Bay (18). Because the bay is only 55 km away from the center of the Kanagawa Prefecture and connected to the Pacific Ocean, I wondered whether Kanagawa Prefecture residents are at risk of eating contaminated fish. From my background research and Tanaka and Takada's publication, I came up with the research question: how does the overuse of plastic in Japan pose an ecological risk to marine species and their consumers in the Kanagawa Prefecture?

RESULTS

For the first part of my investigation, I recorded visual evidence of the presence of plastic in Japan. To do this, I conducted a convenience store plastic audit and took observations of three local waterways. This allowed me to see how much plastic was available to consumers and whether plastic pollution was present nearby. Next, I dissected locally purchased fish for microplastics. I used two methods of dissection: a visual dissection and a more in-depth chemical digestion. Data in this investigation found all fish dissected to have microplastics present. Additionally, these species of fish are typically eaten whole or raw in Japan, potentially exacerbating the impacts on human consumers.

Plastic items at Aeon, a convenience grocery store

Plastic was most often found in the bread, cereal, and snack section and the to-go food section. 99.1% of items in these sections were sold in plastic. Two snacks were boxed, the other 224 items were plastic-wrapped, primarily because they are not made freshly in the convenience store. All but

Table 1. Amount of plastic items at local Aeon convenience grocery store.

Section of Store	Items with Plastic	Items without Plastic	% of Total Items with Plastic
Frozen	261	3	98.9
Fruits & Vegetables	69	9	88.5
Fish, Poultry, & Meat	172	2	98.9
Drinks & Dairy	312	182	63.2
To-Go Food	116	1	99.1
Health	28	41	40.6
Breads, Cereals, & Snacks	224	2	99.1
Candies	60	10	85.7
TOTAL	**1242**	**250**	**83.2**

one to-go food item was served in plastic, as the purpose was to be convenient for shoppers. The most common type of plastic used for food items was plastic wrappers for snacks and bagging for frozen food. The least amount of plastic was found in the health section, where most of the medicine was in glass jars. However, vitamin squeeze pouches and pill packaging were plastic. 88.5% of fresh produce was wrapped in single-use plastic. Overall, 83.2% of this convenience grocery store's items within the recorded sections had plastic wrapping or pieces. Of the plastic-free items, 80% were alcoholic or health drinks (**Table 1**).

Recording observations on plastic pollution and marine species in waterways

Each waterway observed had both plastic pollution and marine species present (**Table 2**). In many instances, both were present at the same time (**Figure 2**).

Dissections

The purpose of my lab dissections was to look for the presence of plastic within fish. From the first part of investigation, I knew that there was plastic available to consumers in Japan, so I wanted to see if there was also plastic present in the fish people eat. I chose to purchase different species of fish from a variety of locations to allow for a wider application (**Table 3**).

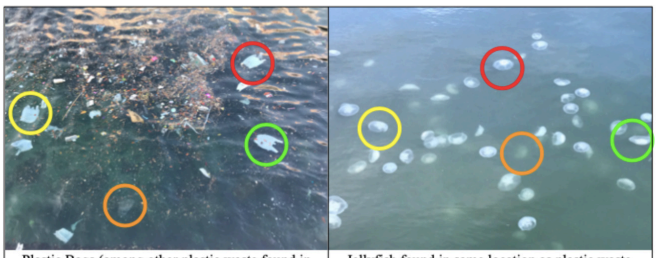

Plastic Bags (among other plastic waste found in Motomachi Canal)

Jellyfish found in same location as plastic waste (different day)

Figure 2. Plastic bags or jellyfish? Two images taken of the same waterway on different days showing instances of plastic pollution and jellyfish.

Table 2. Plastic pollution and marine species found at three waterways.

Location	Examples of Plastic Pollution	Marine Species Example
Yokohama Bay	Plastic bags, plastic food wrappings, plastic bottles	Jellyfish
Motomachi Canal	Plastic bottles, Styrofoam containers, plastic wrappings	Seabird
Yuigahama Beach, Kamakura	Plastic bottles, plastic bags, plastic food wrappings	Various Fish

Table 3. Information on fish used for dissections

English Name (Japanese Romaji Name) *Scientific Name*	Number of Fish Dissected	Fish Origin	Relative Size	Store Type	Purchase Location
Flathead grey mullet (Bora) *Mugil cephalus*	1	Osaka Prefecture	Large	Local fish market	Chinatown, Yokohama
Pacific saury (Sanma) *Cololabis saira*	3	Miyagi Prefecture	Small / Medium	Large grocery and home store	Honmoku, Yokohama
Sweetfish (Ayu) *Plecoglossus altivelis*	1	Aquaculture	Medium	Fish market	Komachi-Dori, Kamakura
Sardines (Iwashi) *Sardinella zunasi* or *Sardinops sagax*	4	Chiba Prefecture	Very Small	Medium grocery	Minatomirai, Yokohama

Visual dissection following CLEAR

For my visual dissections, I followed CLEAR's method. It is aimed towards citizen scientists, meaning it is intended to be accessible to anyone. It had clear directions and illustrations that walked me through the methodology (19). Also, this method has been used in similar contexts, but not within Japan (to my knowledge).

Two species of fish were examined, both of which were found to contain microplastics. The first fish species dissected was the Pacific Saury, a common, inexpensive fish in Japan. Plastic microfibers were recorded in all three Pacific Sauries dissected. The second fish species was the Flathead Grey Mullet. One plastic microfiber was found in this fish.

Chemical digestion using KOH

CLEAR's method lacked in giving complete results since it relied on my eyes to differentiate between microplastics and fish biomass. However, since this method proved plastic being ingested was a relevant issue in the fish local to Kanagawa Prefecture consumers, it allowed me to move forward to a more advanced method. This provided a better representation of the microplastics in each fish (18).

Two different species of species were examined – Sardines and Sweetfish. Using the chemical digestion method, I found a total of 14 microplastics.

The mass of the fish varied from 8.47 to 1626 grams, included four different species, and were all bought from different locations. All the fish I examined contained plastic in some form regardless of size, type, or location purchased.

The most often found microplastic was microfibers (**Figure 3**), and the next most common was thread plastics. Out of the fourteen microplastics found through this chemical digestion method, six were classified as plastic microfibers, due to their thin, flexible structure (**Figure 4**). Four were likely thread plastic, which is stiffer and can evenly fray. Three were see-through pieces of plastic film, likely once a plastic wrapping or bag. The last microplastic found was a white circular plastic, most likely a foam pellet (**Table 4**).

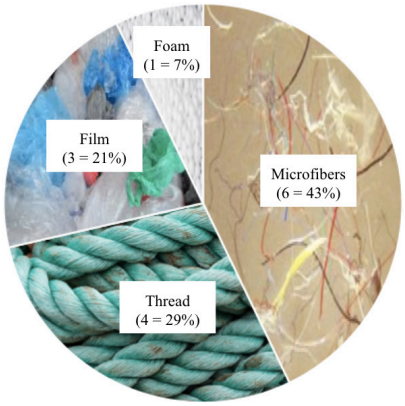

Figure 3. Types of microplastics (microfibers, thread, film, and foam) and their frequencies (measured as percentage of total counted) found in four kinds of dissected fish (flathead grey mullet, Pacific saury, sardines, and sweetfish).

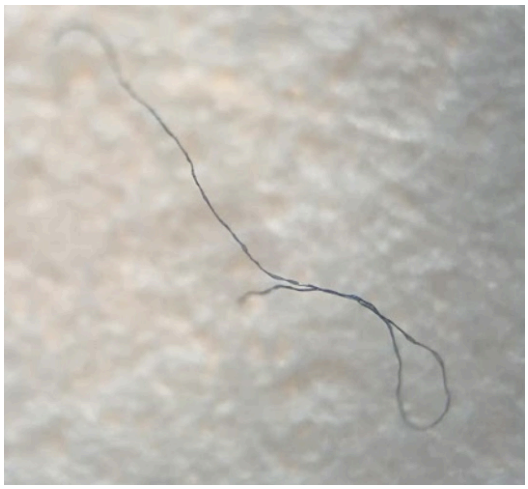

Figure 4. Blue/black plastic microfiber found in the sweetfish.

DISCUSSION

Every year it is estimated that up to 2.5 million tons of microplastics enter the ocean. With Japan being one of the top plastic users and one of the top fish-eating countries, it is not surprising that microplastics were found in all four Japanese-caught fish that I dissected.

It is problematic to humans that both Pacific Saury and Sardines were found to have microplastics because Japanese people tend to eat these fish whole. This means that the microplastics would be directly passed to humans and impact many systems (20).

The presence of microplastics in the Flathead Grey Mullet dissected is supported by a Hong Kong research paper. Cheung *et al.* found 60% of wild Flathead Grey Mullets had ingested microplastics, the most common type being plastic microfibers (21). In Japan, Flathead Grey Mullet is often served raw as sashimi or sushi. This is troublesome because microplastics can carry pollutants which absorb into the flesh of fish, meaning humans are also at risk for ingesting the pollutants.

When buying the Sweetfish, due to a language barrier, I did not know it was created by aquaculture. I chose to analyze it because I thought it would be interesting and applicable as aquaculture still encounters waterways. It was surprising

Table 4. Information on fish used for dissections

Fish Measurements				Plastic Observations	
Fish Type	Weight (g)	Length (cm)	Girth (cm)	Description	~ Length (mm)
Sardine 1	8.39	11.6	0.70	Red thread plastic - likely nylon rope (fishing gear)	5
				White foam plastic (soft pellet)	1
				Black thread plastic	3
Sardine 2	9.95	12.0	0.93	Black plastic microfiber - very thin, had loops	4
				Plastic clear sliver (flexible) - likely bag/wrapping	2
				Plastic clear sliver (flexible) - likely bag/wrapping	2
Sardine 3	8.47	11.9	0.82	Black plastic microfiber	8
				Black thread plastic	2
				Black thread plastic	4
				Plastic film, likely from plastic bag or wrapping	5
Sardine 4	11.0	12.6	1.18	Black plastic microfiber	4
				Black plastic microfiber	5
				Red plastic microfiber	3
Sweetfish	87.7	21.1		Blue/Black plastic microfiber	5

to find a microplastic in the Sweetfish, a fish created by aquaculture (fish farming), because aquaculture fish do not swim in the ocean, where most plastic is found. It shows that other water sources can also be contaminated with plastic. This is worrying as the Sweetfish, or Ayu in Japanese, makes up for around 14% of the total profit earned from freshwater aquaculture in Japan, thus highlighting its importance (22).

Since I do not have the ability to track microplastics' specific movements and origins, I cannot distinctly say a Kanagawa Prefecture residents' plastic is ending up in their local fish. However, while correlation does not equal causation, it is reasonable to believe that if there is more plastic being used there is a higher risk of encountering it in the food chain. Eventually, plastic will end up in a fish. It does not matter whether that fish is in Japan or not, as fish move through currents worldwide and plastic will pose the same threat despite location.

Plastic ingestion is not limited to fish, however. Once the pollution and wildlife share an ecosystem, ingestion is always possible. For example, the plastic bags found in Motomachi Canal resemble the jellyfish that inhabit the bay (**Figure 2**). This can lead to confusion for marine species, such as sea turtles, Brittle sea stars (23), and sea anemone (24) which were found to consume jellyfish in the waters surrounding Japan.

The ecological risk to marine organisms is drastic due to toxic pollutants clinging to the microplastics which can disrupt bodily functions related to hormones and the gut (25). Also, these pollutants can alter population dynamics, specifically trophic levels, as the extent of the problems can be more harmful to certain species, which then changes population levels. Furthermore, the issue only gets worse as you move throughout the trophic levels as both the plastic and toxins accumulate through each level, magnifying the issue at the top.

Despite being in trophic level 2.2, humans are still facing consequences of the bioaccumulation and magnification of plastics and toxins (15). The consequences for humans are still being researched but microplastics are hypothesized to, beyond a certain level of accumulation, inflame the respiratory tract. The persistent pollutants accompanied by the microplastics can also be toxic for humans if ingested (16).

An application that I would be interested to explore would be chemically analyzing microplastics for persistent organic pollutants (POPs). This, along with data collected on the organ health of fish, could highlight the impact of POPs on fish and predict the possible impacts for humans.

While most of the plastic I identified from my dissections was likely from synthetic materials or nylon ropes, Japan's abundance of plastic wrapping is still an issue. The plastic wrapping and packaging found in Japanese convenience stores can break down into microplastics. These types of microplastics were present in my investigation and have been found in fish around the world.

Possible identification methods that could aid further research include Fourier transform infrared (FTIR) and pyrolysis-gas chromatography-mass (Pyr-GC-MS). FTIR can show the specific chemical bonds and weathering of the plastic. Pyr-GC-MS can use thermal degradation to chemically identify microplastics and can be used for trace analysis. Together these methods can shed light on the specific types of plastic present and associated chemicals (12).

In conclusion, I was able to find both inputs and outputs of plastic within Japan's Kanagawa Prefecture (**Figure 1**). All fish dissected had microplastics present and the typical person in Japan consumes a high volume of fish weekly means that it is extremely likely humans are consuming these plastics. While the extent of the negative impacts on humans are currently unknown, it is still evident to a high extent that microplastics have a negative ecological impact overall.

Whether it is Japanese plastic ending up in these fish or not does not matter because the point is that microplastics are ending up in fish around the world. This research coupled with other studies done in North America, Europe, and elsewhere shows that microplastics are a global (and seemingly invisible to the human eye) issue. Because Japanese plastic has already been observed in local waterways, it can be predicted that this plastic will continue to break down into microplastics and be ingested by marine life at some point in the future.

MATERIALS AND METHODS

Counting plastic items in convenience store

People in Japan rely heavily on Convenience Stores for everyday shopping as they are "convenient" being close to train stations and people's homes. To see how much access people have to plastic items, I recorded the number of products that included plastic within the following categories: Frozen, Fruits & Vegetables, Fish & Poultry & Meat, Drinks & Dairy, To-Go Food, Health, Breads & Cereals & Snacks, and Candies. I also recorded qualitative observations to make note of specific trends, such as some items only having a plastic straw, while others had three layers of plastic. I chose to only focus on consumable items due to time constraints. For my results, I calculated the percentage abundance of plastic by dividing the number of products sold containing plastic by the total number of products sold.

Counting plastic pollution and marine species in waterways

I captured photos of both plastic and marine organisms in the following three waterways located in Kanagawa Prefecture (**Figure 5**). This was necessary to show the possibility of the plastic polluting the water being consumed by the marine organisms inhabiting the water. The photos were taken mid-day at the end of summer/beginning of fall.

Visual dissection

I followed Civic Laboratory for Environmental Action Research (CLEAR)'s fish dissection for marine plastic method

Figure 5. The three locations of waterways observed pinpointed on a map of Kanagawa Prefecture, Japan.

and recorded additional information about weight, length, and girth of the fish to highlight the variety of fish dissected (19). This method required me to first cut open the gastrointestinal tract of the fish. Then I placed the opened GI tract onto a coffee filter on a fine mesh strainer and poured distilled water over the contents. This allowed me to visually inspect for plastic. It was a good baseline method as it showed marine plastics were present in the fish. I used CLEAR's "Spotter's Guide" to identify the type of plastic present throughout my dissections.

Chemical digestion and analysis

Looking for a more advanced dissection method, I found Kühn *et al*'s research paper which highlighted the usage of potassium hydroxide (KOH) for isolating microplastics from the marine organisms (26). KOH dissolves organic material (GI) while leaving the plastic in the solution. After reading about KOH, I decided to seek inspiration from Tanaka and Takada's method (18). First, I dissected fish by cutting from anus to mouth, following CLEAR's method. Next, I prepared a 10% KOH solution in test tubes. I put the gastrointestinal tract into 10-20 mL (>3x the volume of the gut) of this solution to digest organic material. Then, I placed the test tubes with the solution and GI tracts in an incubator at 40°C for 10 days, stirring with a stirring rod every 3 days to break up non-digestible material. After 10 days, only non-digestible material was left, allowing me to identify microplastics.

ACKNOWLEDGMENTS

I would like to thank Ms. Urquhart (my research mentor), Kobayashi-san (the lab technician), my other IB teachers, my parents, and the JEI Editors for their helpful support while conducting my research and writing.

Received: June 2, 2020
Accepted: December 20, 2020
Published: January 20, 2021

REFERENCES

1. Tullo, Alexander. "C&EN's Global Top 50 Chemical Companies of 2014." *C&EN*, American Chemical Society, 2014, cen.acs.org/articles/93/i30/Global-Top-50.html. Accessed 15 Oct. 2019.
2. Helmenstine, Anne Marie. "Plastic Definition and Examples in Chemistry." *ThoughtCo*, DotDash, 8 July 2019, www.thoughtco.com/plastic-chemical-composition-608930. Accessed 15 Oct. 2019.
3. Jambeck, J. R., *et al*. "Plastic Waste Inputs from Land into the Ocean." *Science*, vol. 347, no. 6223, 12 Feb. 2015, pp. 768–771, science.sciencemag.org/content/347/6223/768, 10.1126/science.1260352. Accessed 8 Aug. 2019.
4. Dorger, Samanda. "These Countries Produce the Most Plastic Waste." *TheStreet*, TheStreet, 27 Feb. 2019, www.thestreet.com/world/countries-most-plastic-waste-14878534. Accessed 5 Sept. 2019.
5. "Time for Japan to Lose Its Plastic Dependency and Save the Oceans." *The Asahi Shimbun*, The Asahi Shimbun Company, 20 Oct. 2018, www.asahi.com/ajw/articles/AJ201810200027.html. Accessed 8 Aug. 2019.
6. Jowit, Juliette. "Drop in Plastic Bags Littering British Seas Linked to Introduction of 5p Charge." *The Guardian*, The Guardian, 5 Apr. 2018, www.theguardian.com/environment/2018/apr/05/drop-in-plastic-bags-littering-british-seas-linked-to-introduction-of-5p-charge. Accessed 8 Aug. 2019.
7. Geyer, Roland, *et al*. "Production, Use, and Fate of All Plastics Ever Made." *Science Advances*, vol. 3, no. 7, July 2017, p. E1700782, plasticoceans.org/wp-content/uploads/2018/05/Production_use_and_fate_of_all_plastics_ever_made.pdf, 10.1126/sciadv.1700782. Accessed 7 October 2019.
8. Laist, David W. "Impacts of Marine Debris: Entanglement of Marine Life in Marine Debris Including a Comprehensive List of Species with Entanglement and Ingestion Records". *Marine Debris Sources, Impacts, and Solutions,* edited by James M. Coe and Donald Rogers, Springer-Verlag New York Inc. New York, NY, 1997, pp. 99–139, www.researchgate.net/profile/David_Laist/publication/235768493_Impacts_of_Marine_Debris_Entanglement_of_Marine_Life_in_Marine_Debris_Including_a_Comprehensive_List_of_Species_with_Entanglement_and_IngestiOn_Records/links/02bfe5136037d75c73000000.pdf. Accessed 15 Oct.

2019.

9. Gewert, Berit, *et al*. "Pathways for Degradation of Plastic Polymers Floating in the Marine Environment." *Environmental Science: Processes & Impacts*, vol. 17, no. 9, 2015, pp. 1513–1521, pubs.rsc.org/en/content/articlelanding/2015/EM/C5EM00207A#!divAbstract,10.1039/c5em00207a. Accessed 8 Sept. 2019.
10. Kataoka, Tomoya, *et al*. "Assessment of the Sources and Inflow Processes of Microplastics in the River Environments of Japan." *Environmental Pollution*, vol. 244, 26 Oct. 2018, pp. 958–965. *ScienceDirect*, www.sciencedirect.com/science/article/pii/S0269749118338028, 10.1016/j.envpol.2018.10.111. Accessed 16 Oct. 2019.
11. Lebreton, L., *et al*. "Evidence That the Great Pacific Garbage Patch Is Rapidly Accumulating Plastic." *Scientific Reports*, vol. 8, no. 1, 22 Mar. 2018. *Scientific Reports*, www.nature.com/articles/s41598-018-22939-w, 10.1038/s41598-018-22939-w. Accessed 9 Oct. 2019.
12. Wang, Wenfeng, and Jun Wang. "Investigation of Microplastics in Aquatic Environments: An Overview of the Methods Used, from Field Sampling to Laboratory Analysis." *TrAC Trends in Analytical Chemistry*, vol. 108, 11 Sept. 2018, pp. 195–202, www.jlakes.org/uploadfile/news_images/hpkx/2018-11-09/1-s2.0-S0165993618303686-main.pdf, 10.1016/j.trac.2018.08.026. Accessed 12 Sept. 2019.
13. "The Problem of Marine Plastic Pollution." *Clean Water Action*, Clean Water Action, 20 Dec. 2017, www.cleanwater.org/problem-marine-plastic-pollution. Accessed 8 Aug. 2019.
14. Valentine, Katie. "Zooplankton Are Eating Plastic, And That's Bad News for Ocean Life." *ThinkProgress*, 14 July 2015, thinkprogress.org/zooplankton-are-eating-plastic-and-thats-bad-news-for-ocean-life-dbe31be8ae2b/. Accessed 8 Sept. 2019.
15. Bonhommeau, Sylvain, *et al*. "Eating up the World's Food Web and the Human Trophic Level." *Proceedings of the National Academy of Sciences*, vol. 110, no. 51, 2 Dec. 2013, pp. 20617–20620. *Proceedings of the National Academy of Sciences of the United States of America*, www.pnas.org/content/110/51/20617, 10.1073/pnas.1305827110. Accessed 19 Oct. 2020.
16. de Wit, Wijnand, *et al*. "No Plastic in Nature: Assessing Plastic Ingestion from Nature to People." World Wide Fund for Nature, June 2019. Accessed 7 October 2019.
17. Renton, Alex. "One in Ten Fish Is Eaten in Japan. So Why Don't They Know There's a Shortage?" *The Guardian*, The Guardian, 10 Apr. 2005, www.theguardian.com/world/2005/apr/10/japan.foodanddrink. Accessed 8 Aug. 2019.
18. Tanaka, Kosuke, and Hideshige Takada. "Microplastic Fragments and Microbeads in Digestive Tracts of Planktivorous Fish from Urban Coastal Waters." *Scientific Reports*, vol. 6, no. 1, 30 Sept. 2016, www.nature.com/articles/srep34351, 10.1038/srep34351. Accessed 8 Aug. 2019.
19. Civic Laboratory for Environmental Action Research. "Marine Plastics in Fish: A Citizen Science Dissection & Analysis Protocol." Accessed 7 October 2019.
20. Itoh, Makiko. "Autumn Is Peak Season for 'Sanma,' a Once-Common Fish That's Playing Hard to Catch | The Japan Times." *The Japan Times*, 14 Oct.2017, www.japantimes.co.jp/life/2017/10/14/food/autumn-peak-season-sanma-common-fish-become-hard-find/#.XW-xCJMzbBI. Accessed 4 Sept. 2019.
21. Cheung, Lewis, Ching Lui, and Lincoln Fok. "Microplastic Contamination of Wild and Captive Flathead Grey Mullet (Mugil Cephalus)." *International Journal of Environmental Research and Public Health* 15.4 (2018): 597. *Crossref*. Web. Accessed 7 October 2019.
22. Makino, M. "FAO Fisheries & Aquaculture National Aquaculture Sector Overview (NASO)." Food and Agriculture Organization of the United Nations, 11 July 2017, www.fao.org/fishery/countrysector/naso_japan/en. Accessed 11 Sept. 2019.
23. Miyake, Hiroshi, *et al*. "Scyphomedusa Aurelia Limbata (Brandt, 1838) Found in Deep Waters off Kushiro, Hokkaido, Northern Japan." *Plankton Biology and Ecology*, vol. 49, no. 1, 2002, pp. 44–46. *The Plankton Society of Japan*, www.plankton.jp/PBE/issue/vol49_1/vol49_1_044.pdf. Accessed 15 Oct. 2019.
24. Yamamoto, Jun, *et al*. "Transportation of Organic Matter to the Sea Floor by Carrion Falls of the Giant Jellyfish Nemopilema Nomurai in the Sea of Japan." *Marine Biology*, vol. 153, no. 3, 29 Sept. 2007, pp. 311–317. *ResearchGate*, www.researchgate.net/publication/225326725_Transportation_of_organic_matter_to_the_sea_floor_by_carrion_falls_of_the_giant_jellyfish_Nemopilema_nomurai_in_the_Sea_of_Japan, 10.1007/s00227-007-0807-9. Accessed 15 Oct. 2019.
25. Boucher, Julien, and Damien Friot. "Primary Microplastics in the Oceans: A Global Evaluation of Sources." *IUCN*, 21 Feb. 2017, pp. 1–43, storyofstuff.org/wp-content/uploads/2017/02/IUCN-report-Primary-microplastics-in-the-oceans.pdf, 10.2305/iucn.ch.2017.01.en. Accessed 8 Sept. 2019.
26. Kühn, Susanne, *et al*. "The Use of Potassium Hydroxide (KOH) Solution as a Suitable Approach to Isolate Plastics Ingested by Marine Organisms." *Marine Pollution Bulletin*, vol. 115, no. 1–2, Feb. 2017, pp. 86–90, www.sciencedirect.com/science/article/pii/S0025326X16309547, 10.1016/j.marpolbul.2016.11.034. Accessed 8 Aug. 2019.

JOURNAL OF
EMERGING INVESTIGATORS

Article

Long Range Radio Communication for Urban Sensor Networks

Molly Cantillon[1], Kevin A. Kam[2], Ioannis Kymissis[2]
[1] Newark Academy, Livingston, NJ
[2] Columbia University, Department of Electrical Engineering, New York, NY

SUMMARY

Society's technological landscape is growing rapidly. In the era of smart cities, wireless technologies and their novel applications have begun to permeate almost every aspect of urban life. From controlling traffic signals to monitoring air quality, the Internet of Things (IoT) has emerged as a field with much potential, but some challenges. Being a relatively new field of research, there is much more to discover about IoT. Before developing proposed applications of the technology in smart cities, it is imperative to fully understand how IoT-based technologies work, including Long-Range Radio Communication (LoRa). This study aimed to test the feasibility of LoRa devices in the bustling, urban environment of New York City to identify limitations in the technology. Using a testbed containing two LoRa radio modules and a monopole antenna, we determined the relationship between the distance of the radios and received signal strength to be inversely proportional. We hypothesized that Received Signal Strength Index values from the transmissions could be used to determine the maximum range. Our results supported this hypothesis by determining the maximum range to be 250 meters. In addition, we found that the relationship followed an exponential decay curve. These findings will help future researchers further understand the limitations of LoRa in urban sensor networks and ultimately create stronger IoT smart city applications.

INTRODUCTION

As technology in society rapidly advances, the applications for new innovations become more widespread. Network communication technology, which allows devices to communicate independently with each other, has become vital to modern-day life, especially in cities where new technological devices are used daily. In fact, the Internet of Things (IoT) has emerged as a way of conceptualizing the digitally connected universe of billions of physical devices that collect, process, and share data with each other (1). Wireless Sensor Networks (WSNs) are a subset of IoT that use many self-controlled nodes to process and send information to a central unit (2).

Within the concept of IoT, Long Range Radio Communication (LoRa) technology has been implemented in devices to streamline the transmitting and receiving of messages. LoRa was found to be extremely well suited for IoT applications due to its wide coverage, long range, and low battery consumption (3). Therefore, it has increasingly garnered attention, especially for uses in urban environments where life is much more crowded and densely-populated. As a result, a multitude of applications have been proposed for LoRa-based WSNs in urban settings. For example, LoRa-based technology has been proposed in smart street lighting systems to detect faults instantly and more accurately, reducing the high costs of manually maintaining street lighting (4). It has also been proposed for monitoring real-time Particulate Matter (PM) concentration for air quality indications in urban areas (5).

Along with other proposed uses in home sensors, vehicular systems, climate sensors, and water sensors, LoRa-based technology is just now being recognized for its potential to improve the quality of life in cities. What is still missing to fully implement the technology, however, is the extensive testing of LoRa-based WSNs as a new, interdisciplinary field (6). A characterization of LoRa's capabilities would help bring these ambitious proposals into perspective by providing an accurate sense of the maximum possible range in controlled urban environments.

In this project, an urban wireless testbed was developed on Columbia University's Morningside Heights campus in New York City (NYC), one of the world's biggest hotspots for LoRa-based applications due to its densely populated environment. This testbed featured two LoRa radios, operating at the US LoRa standardized frequency of 915 MHz. The radios sent packages from the transmitter to a receiver while simultaneously collecting the Received Signal Strength Index (RSSI) value, a standard indicator in the field of wireless communication of the power level received from a transmitted signal. We hypothesized that the RSSI values could be used to determine the maximum range of the technology in urban sensor networks, which found to be approximately 250 meters. These findings will inform how proposed solutions of LoRa applications in urban settings should be designed, leading to a holistically stronger understanding in the field of urban sensor networks.

RESULTS

In order to test the feasibility of LoRa radios, we hypothesized that range would be one of the most crucial components to understand. We tested LoRa radios in New York City, a densely populated urban environment where the need for adaptable LoRa-based IoT technology is strong. To determine the true maximum range, the LoRa radios were tested in a near ideal path: a direct line of sight on Columbia University's campus. The test began with the receiver and transmitter right next to each other, where the signal connection was maximized and the RSSI value was around 0 decibels per milliwatt (dBm). A RSSI value at 0

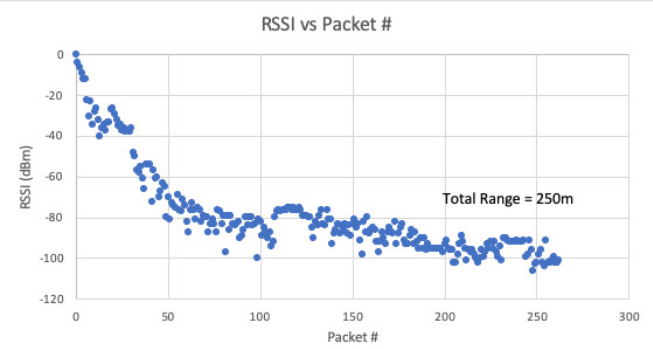

Figure 1: Inverse Relationship of Packet # versus RSSI values

dBm is the strongest connection, with a power level of 1 mW, meaning no antenna or power loss occurred during the transmission. Decibels per milliwatt represents the ratio of the power level from the transmitted signal, which decreases as the signal weakens. As the range between the transmitter and receiver radios consistently widened with the increasing packet number marking the current transmission number, the corresponding RSSI values were recorded. We deemed the final range when the receiver could no longer detect a signal from the transmitter and the RSSI value neared -110 dBm, the threshold often associated with no signal (7).

In total, 263 packets were transferred from the transmitter to the receiver. Those packets were graphed against their corresponding RSSI values (**Figure 1**), where the points resemble an exponential decay function ($y = ae^{-t}$) in which the first few RSSI values were the highest and decreased throughout the test. Bearing the assumption that the receiver was moving at a constant speed throughout the trial, the packet number is directly proportional to the distance between the two radios. In other words, as distance between the transmitter and receiver increases, the signal strength decreases because the signal gets more diluted by space and other interferences in the path. Thus, this indicates an inverse relationship between distance and signal strength.

The natural log of the points (ln(y) vs -t) were graphed to model the exponential decay function (**Figure 2**). The linearized exponential decay produced points clustered around the trendline y = 0.4318x + 2.3231, resulting in a strong exponential decay correlation ($R^2 = 0.8524$) between signal strength, packet number, and distance.

The standard deviations of the RSSI values at each point differed dramatically in different parts of the graph; for example, the points at the 100th packet were widely scattered but became a tight cluster around the 110th packet. The final range for the 915 MHz LoRa Radio Modules, recorded at the point where the RSSI value reached -110dBm, we determined to be around 250 meters through a GPS-tracking map of the path (**Figure 3**).

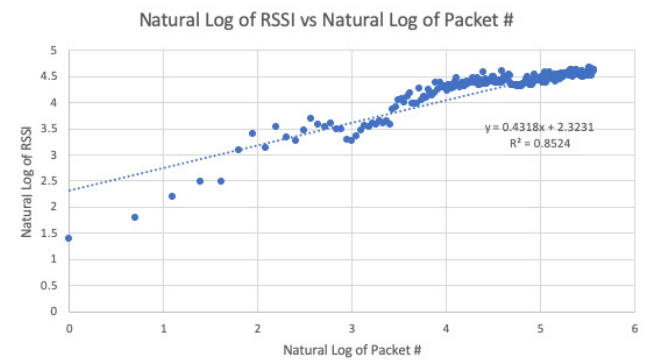

Figure 2: Linearized Exponential Decay Curve (ln(y) vs. x)

DISCUSSION

The packet number, resembling distance in meters, was graphed versus RSSI (**Figure 1**). Supporting the hypothesis, the maximum possible range of LoRa radio transmission was determined from the graph to be about 250 meters. While the points generally follow an inversely proportional shape, there are large deviations in the RSSI values especially around packet 100 and 225. In both cases, the values after these large spreads seemed to be very precise and stronger than it had been, suggesting some sort of recalibration internally from the radio.

While this project revealed the feasibility and relationship of components in LoRa technology, a series of limitations encountered in the experiment may have impacted the results and the experiment's reproducibility. One limitation occurred with the monopole antenna, a simple stripped wire, which was effective but not ideal for transmitting over long ranges. Another limitation was the public testing environment which was not completely in a clear line of sight and affected by people walking in between the signal's path, restricting the full potential of the maximum range obtained.

In future studies, using active impedance matching antennas, which have been shown to perform well in changing environments (8), might help obtain more accurate results. Using a better radio frequency (RF) module may have increased the wireless communication's efficiency. Additionally, setting a higher power to those devices would increase signal strength and maximum range.

Overall, this analysis of LoRa's feasibility in an urban environment is important as it highlights the flaws within LoRa technology, leading future researchers to better understand how proposed LoRa applications should be designed using

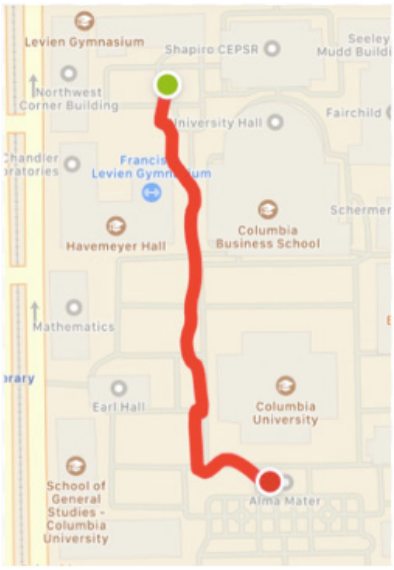

Figure 3: GPS-Tracked Path of Transmitter on Columbia University's Morningside Heights campus in New York City

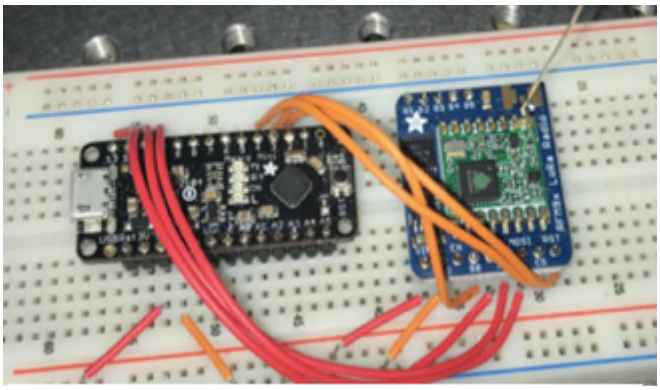

Figure 4: Photograph of Transmitter/Receiver Mechanism containing microprocessor Metro Mini and LoRa Radio on a Breadboard

stronger matched antennas and RF modules. Ultimately, the findings impact not only the field of LoRa communication, but also IoT Wireless Sensor Networks which rely on LoRa implementation in smart city devices.

METHODS

Hardware Configuration

To measure LoRa technology's feasibility in urban settings, a unique testbed containing two LoRa RFM 9x 915 MHz Radio Modules and two Metro Mini microcontrollers was created. The chips were soldered onto headers and placed on a breadboard (**Figure 4**). A monopole antenna was designed using the following equation to calculate wavelength from frequency (9):

$$\lambda = c/f$$

$$\lambda = (3.00 * 10^8)\frac{m}{s}/(9.15 * 10^8)Hz$$

$$\lambda = .328\ m = 32.8\ cm$$

$$\frac{\lambda}{4} = 8.20\ cm$$

The simple monopole antenna, *λ/4* or 8.20 cm long, was soldered onto a conductive ground plane similar to the design in **Figure 5**. The signal pin from the antenna was then used to transfer and receive signals from the radios. The radio's ground (GND), power (VIN), and Serial Peripheral Interface (SPI) logic pins were connected to the Metro Mini to analyze the obtained information. Although the physical setup of the two configurations was the same, the code sent to the radios was differentiated between the receiver and the transmitter.

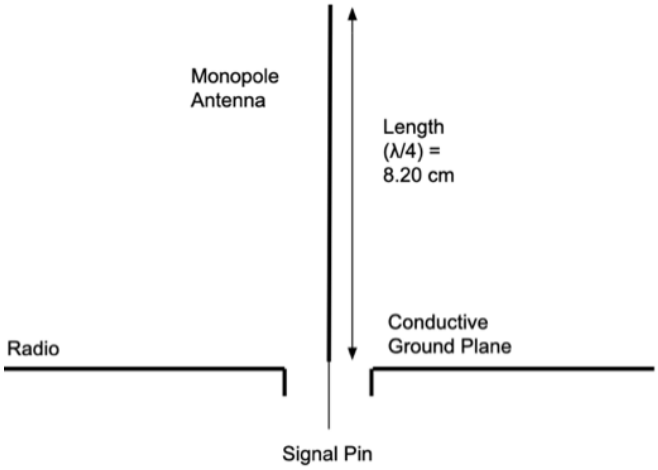

Figure 5: Design of the Monopole Antenna with Length *λ/4* for Packet Transmission

Algorithm

Arduino IDE Software was used to program the Metro Mini. Shown in the block diagram, the transmitter code loads necessary packages, defines the proper ports, and resets the radio before checking if it is fully initialized (**Figure 6**). Once fully initialized, the loop of the program is entered where the radio first creates a packet that contains the message "Hello World" along with the nth iteration of the loop. It sends the packet, waits for acknowledgement that it was received, and searches for a reply message from the receiver. Once a reply message is received, the message is sent through an RS232 serial connection to the device running the program, printing the message and the corresponding RSSI value of the transfer. RSSI values start at 0 dBm being the strongest signal and decrease as the signal becomes weaker. A paper analyzing smart home WiFi signals determined that the RSSI values for WiFi connections can fluctuate anywhere between -60 and -80 dBm (10). These actions repeat continuously approximately every five seconds while the number in the "Hello World" packet will increase by one, accompanied by a new RSSI value on the Serial Monitor.

The receiver code has the same general structure of initializing the radio at the start of each experimental run, but in the main loop of the program, the order of the commands is reversed with the radio first searching for a packet and then sending a reply. The transmitter and receiver codes run simultaneously to ensure a complete and accurate test.

Procedure

This experiment was carried out on Columbia University's Morningside Heights campus in NYC. The packets were transmitted at a frequency of 915 MHz, the standard for the radios. After the configuration was assembled and the code was uploaded to both radios, the radios were carried, walking

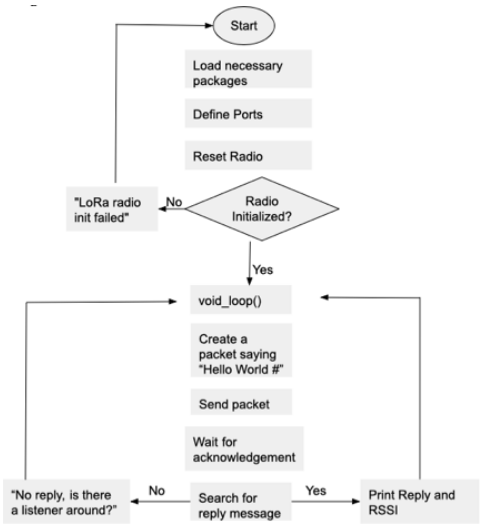

Figure 6: Overall Flowchart Block Diagram of Transmitter Radio Code

on foot at a constant speed until the signal could no longer be detected. The test was repeated two times although only the last test was used for data processing. In total, each trial lasted around four minutes.

ACKNOWLEDGEMENTS

We would like to thank the NYU GSTEM program for supporting us and connecting us with each other.

Received: July 1, 2020
Accepted: December 20, 2020
Published: January 26, 2021

REFERENCES

1. Jorke, Pascal, *et al*. "Urban Channel Models for Smart City IoT-Networks Based on Empirical Measurements of LoRa-Links at 433 and 868 MHz." *2017 IEEE 28th Annual International Symposium on Personal, Indoor, and Mobile Radio Communications (PIMRC)*, 2017, doi:10.1109/pimrc.2017.8292708.
2. Jais, Ilman, *et al*. "Received Signal Strength Indication (RSSI) Code Assessment for Wireless Sensors Network (WSN) Deployed Raspberry-Pi." *2016 International Conference on Robotics,* Automation and Sciences (ICORAS), 2016, doi:10.1109/icoras.2016.7872618.
3. Ouanounou, Emmanuel, *et al*. "LoRaWAN & MQTT: What to Know When Securing Your IoT Network." Security Boulevard, 15 Oct. 2020, securityboulevard.com/2020/10/lorawan-mqtt-what-to-know-when-securing-your-iot-network/.
4. Bingol, Ezgi, *et al*. "A LoRa-Based Smart Streetlighting System for Smart Cities." *2019 7th International Istanbul Smart Grids and Cities Congress and Fair (ICSG)*, 2019, doi:10.1109/sgcf.2019.8782413.
5. Yun, Jaeseok, *et al*. "Real-Time PM Monitoring System Based on oneM2M IoT Platform and LoRa Networks." *2019 IEEE Sensors*, 2019, doi:10.1109/sensors43011.2019.8956570.
6. Fernandes, Rui, *et al*. "On the Real Capacity of LoRa Networks: The Impact of Non-Destructive Communications." *IEEE Communications Letters*, vol. 23, no. 12, 2019, pp. 2437–2441., doi:10.1109/lcomm.2019.2941476.
7. Mammen, S. "Making Sense of Signal Strength/Signal Quality Readings for Cellular Modems," *Industrial Networking Solution Tips & Tricks*, blog.industrialnetworking.com/2014/04/making-sense-of-signal-strengthsignal.html
8. Laxpati, S., and R. Mittra. "Antenna Impedance Matching By Means Of Active Networks." *Electrical Engineering Research Laboratory University of Illinois,* Jan. 1962, doi:10.21236/ad0291766.
9. Albarracín, Ricardo, *et al*. "On the Use of Monopole Antennas for Determining the Effect of the Enclosure of a Power Transformer Tank in Partial Discharges Electromagnetic Propagation." *Sensors*, vol. 16, no. 2, 2016, p. 148., doi:10.3390/s16020148.
10. Jiang, H, *et al*. "Smart Home Based on WiFi Sensing: A Survey." *IEEE Access*, 7 Mar. 2018, p. 2., doi:10.1109/ACCESS.2018.2812887.

JOURNAL OF
EMERGING INVESTIGATORS

Article

Predicting Orbital Resonance of 2867 Šteins Using the Yarkovsky Effect

Will Rosenberg[1], Esteban Herrera-Vendrell[1]*, Raymond Nucuta[1]*, Karsen Wahal[1]*, Sarthak Bhardwaj[1], William Bryce Gallie[1], Paul McClernon[1]

[1] BASIS Scottsdale, Scottsdale, Arizona; * These authors contributed equally

SUMMARY

While gravitational forces have the largest impact on asteroid orbit determination, thermal forces such as the Yarkovsky and YORP effects also perturb asteroid orbits. We analyzed the impact of these thermal effects on the orbit of asteroid 2867 Šteins, an E-type asteroid measuring five kilometers in diameter. The orbit of Šteins lies within the range of a Kirkwood Gap, a region devoid of asteroids because of Jupiter's gravitational pull. Given that thermal effects can perturb asteroids of similar properties, we sought to determine whether the Yarkovsky effect would push Šteins into a Kirkwood Gap within 50,000 years. Based on Šteins' location and size, we hypothesized that the Yarkovsky effect will push Šteins into a Kirkwood gap. We computationally generated a thermal map of Šteins to approximate the Yarkovsky force and YORP torque. Analysis of the thermal map yielded an average Yarkovsky force parallel to velocity of -0.714 N and acceleration of -5.22×10^{-15} m/s^2. The torque parallel to the angular velocity due to the YORP effect was 4.680 N m, with an angular acceleration of 1.217×10^{-20} rad/s^2. We inputted the calculated Yarkovsky force into NASA's GMAT to model the resulting change to Šteins' orbit and found that the Yarkovsky force decays the semi-major axis of Šteins by 16.4 km in 242.2 years, and up to 5,365 km in 50,000 years within 95% confidence. This perturbation is unlikely to transfer Šteins into a Kirkwood Gap.

INTRODUCTION

In recent decades, scientists have increasingly focused on the motion of asteroids. Many people fear the risks of an asteroid hitting Earth, with NASA scientists warning of a potential collision in 2068 (1). While it was originally believed that asteroids were primarily affected by gravitational forces, recent research revealed that other forces due to the Yarkovsky effect play a role in an asteroid's trajectory. Discovered by Polish engineer Ivan Yarkovsky, the Yarkovsky effect is a force caused by the asymmetrical emission of electromagnetic radiation due to thermal radiation from rotating bodies in space (2). As the asteroid rotates, the Sun heats it, and the radiation absorbed by the asteroid is re-emitted in a different direction because of the delay between absorption and re-emission (2). This re-emission generates a recoil force in the opposite direction of the emission of electromagnetic radiation (2). Although the Yarkovsky effect exists in all astronomical bodies, it is typically observed most prominently in asteroids because asteroids have the highest surface area to mass ratios in regard to natural astronomical bodies (3).

Existing literature indicates that the Yarkovsky effect can perturb the orbit of an asteroid over long periods of time. However, research on the Yarkovsky effect remains small-scale; this study applied this effect to 2867 Šteins. 2867 Šteins is an E-type, non-family, inner belt asteroid that orbits the Sun with a semi-major axis of 2.3633 AU and an orbital period of 1327 days (4). We hoped to answer the question: will the Yarkovsky effect push 2867 Šteins into a Kirkwood Gap within 50,000 years? We investigated whether the Yarkovsky effect will push 2867 Šteins into a Kirkwood Gap within a 50000-year timespan through the use of computer modeling. We hypothesized that 2867 Šteins will be pushed into a Kirkwood gap because Šteins falls into the range of asteroid sizes significantly impacted by the Yarkovsky effect. Šteins is close to a Kirkwood Gap, which is a region of the asteroid belt largely devoid of asteroids. These gaps exist at 2.06 AU, 2.5 AU, 2.82 AU, 2.95 AU, and 3.27 AU from the Sun. Bodies with semi-major axes that reside within Kirkwood Gaps are in orbital resonance with Jupiter, resulting in a gravity assist from Jupiter that eventually propels the body out of the asteroid belt and potentially into the inner solar system (5). Due to 2867 Šteins' retrograde rotation, the Yarkovsky effect will cause it to spiral inwards towards the Sun. Therefore, the closest Kirkwood Gap inwards is considered. The distance from 2867 Šteins to this Kirkwood gap is 0.30 AU. In this study, we determined the effect of the Yarkovsky effect on pushing Šteins into a Kirkwood gap by simulating the asteroid's orbit. We concluded that the Yarkovsky effect does perturb the orbit of Šteins, but the asteroid does not enter a Kirkwood Gap.

RESULTS

To test whether or not 2867 Šteins entered a Kirkwood gap within 50,000 years, we generated a thermal map based on the Simple Thermal Model outlined by Rozitis and Green (6), assuming thermal properties from the Rosetta flyby. We implemented the model at six different positions along the orbit, calculating a force vector and torque vector from each thermal map. We modeled the resulting thermal map of one of the positions for 2867 Šteins (**Figure 1**).

The torque parallel to the angular velocity was represented by τ_P. Each force vector was broken into three directions: tangent to the velocity (F_T), perpendicular to the orbital plane (F_P), and perpendicular to the velocity and in the orbital plane (F_O). These three directions created a new coordinate axis that the force is defined on. The new coordinate axis accounted for the changing position in the orbit by defining the force vector relative to the velocity vector. Using this coordinate

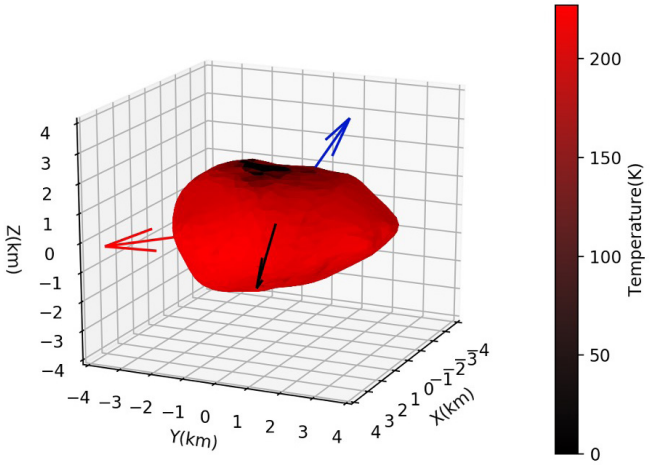

Figure 1: Thermal Map of 2867 Šteins. The thermal map of 2867 Šteins at its position on June 15, 2015 is represented. The temperature of each facet is represented through a linear color gradient. The black vector points towards the Sun, the red vector represents the direction of the velocity of the asteroid, and the blue vector displays the direction of the final Yarkovsky force vector. The off-center locations of the hottest facets shift the Yarkovsky force vector off-center against the asteroid's direction of motion.

axis, we simulated each force for one-sixth of 2867 Šteins' orbit for 242.2 years. The Yarkovsky force and torque results for each respective date were documented (**Table 1**).

The magnitude and direction of each position's tangential force relative to the other positions were plotted to visualize the calculated forces (**Figure 2**). Using the data from each position, the average tangential Yarkovsky force was calculated as -0.714 N, and the average tangential acceleration was -5.22 x 10^{-15} m/s^2. The average torque in the direction of angular momentum was 4.680 N m, and the average angular acceleration was 1.217 x 10^{-20} rad/s^2.

The results from NASA's GMAT vR2020a Orbital Determination software (7) revealed that 2867 Šteins' semi-major axis decays 16.4 km in 242.2 years (**Figure 3A**). This shift is not significant enough to push Šteins' into a Kirkwood Gap. NASA's GMAT orbital determination software (7) also revealed that 2867 Šteins' orbital inclination decays 2.35 x 10^{-9} in 242.2 years (**Figure 3B**) and 2867 Šteins' change in orbital eccentricity has a fluctuation with an amplitude greater than the average value, making the average change

Date	Position Relative to the Sun (*AU*)	Force (*N*)	τ_P (*N·m*)	F_T (*N*)	F_P (*N*)	F_O (*N*)
March 30, 2014	x = -0.530 y = 2.593 z = 0.334	x = 0.306 y = 1.236 z = 1.086	-0.056	-0.344	0.992	1.304
November 6, 2014	x = -2.226 y = 1.412 z = 0.461	x = -0.643 y = 1.060 z = 1.221	-15.027	-0.636	1.008	1.269
June 15, 2015	x = -2.290 y = -0.758 z = 0.255	x = -1.670 y = 0.200 z = 1.025	12.153	-1.050	0.753	1.487
January 22, 2016	x = -0.2421 y = -2.069 z = -0.171	x = -1.199 y = -2.217 z = -0.641	4.637	-1.063	-0.584	2.301
August 30, 2016	x = 1.959 y = -0.580 z = -0.340	x = 1.987 y = -1.583 z = -1.592	3.227	-0.812	-1.131	2.656
April 8, 2017	x = 1.520 y = 1.855 z = -0.034	x = 1.515 y = 0.797 z = 0.237	23.145	-0.377	0.371	1.646

Table 1: Yarkovsky Force and Torque vectors. The Yarkovsky force and torque vectors at each of the six simulated positions in the orbit. All position data is represented on a Heliocentric coordinate system in AU.

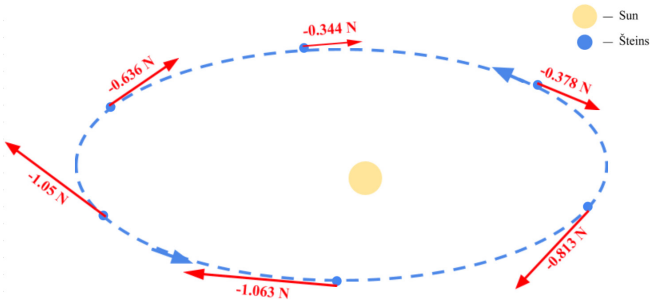

Figure 2: 2867 Šteins' Orbit Diagram. The magnitude and direction of the tangential Yarkovsky force at each simulated position in Šteins' orbit. The orbit is projected onto the XY plane and is therefore distorted to look more elliptical. Šteins is orbiting counterclockwise around the sun. The length of each arrow matches the magnitude of the tangential Yarkovsky force. This figure is not to scale.

in eccentricity over 242.2 years insignificant (**Figure 3C**).

The change in the semi-major axis, inclination, and eccentricity was forecasted for 5 time intervals with 95% confidence intervals (**Table 2**). The results from the forecasted data reveals that the maximum magnitude change in the semi-major axis over 50,000 years is 5,365 km with 95% confidence, the maximum magnitude change in the inclination over 50,000 years is -5.02 x 10^{-7}° with 95% confidence, and the maximum magnitude change in the eccentricity over 50,000 years is 6.34 x 10^{-6} with 95% confidence.

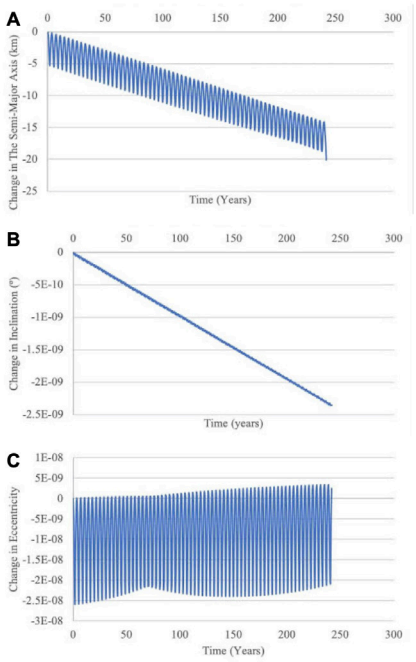

Figure 3: Orbital Elements Versus Time Graphs. Graphs of the changes in Šteins' semi-major axis, inclination, and eccentricity over the documented time period of 242.2 years during the GMAT simulation. **A)** Change in the Semi-Major Axis Vs. Time: A graph of the change in Šteins' semi-major axis (km) versus time (years) during the orbital GMAT simulation for 242.2 years. **B)** Change in the Inclination Vs. Time: A graph of the change in Šteins' inclination (°) versus time (years) during the orbital GMAT simulation for 242.2 years. **C)** Change in Eccentricity Vs. Time: A graph of the change in Šteins' eccentricity (unitless) versus time (years) during the orbital GMAT simulation for 242.2 years.

Time (years)	Change in the semi-major axis (km)	95% Confidence Radius	Change in Inclination (°)	95% Confidence Radius	Change in Eccentricity	95% Confidence Radius
250	-17.01	0.31	-2.4E-09	3.1E-12	3.3E-09	7.1E-10
500	-34.8	2.1	-4.8E-09	2.2E-11	4.6E-09	4.9E-09
1000	-59.9	6.3	-9.7E-09	6.3E-11	-7.5E-09	1.5E-08
10000	-595	214	-9.7E-08	2.0E-09	1.5E-07	5.0E-07
50000	-2950	2415	-4.8E-07	2.2E-08	7.4E-07	5.6E-06

Table 2: Orbital results of The Yarkovsky Effect. Using a forecast function and exponential smoothing, the changes in the semi-major axis, inclination, and eccentricity are forecasted over longer time spans with a 95% confidence interval documented. The three orbital elements are forecasted for five points, ending at 50,000 years.

DISCUSSION

The results indicated, with 95% confidence that 2867 Šteins will not enter a Kirkwood Gap within 50,000 years. After 50,000 years, Šteins was predicted to move 0.0065% of the 0.3033 AU necessary to enter a Kirkwood Gap. If Šteins follows the confidence interval's lower bound, Šteins will move 0.012% of the 0.3033 AU to enter a Kirkwood Gap. Thus, the minimal change in Šteins' semi-major axis provides evidence that the Yarkovsky effect does not exert a force strong enough to push e asteroids with sizes comparable to Šteins into a Kirkwood Gap. However, the Yarkovsky force does have a significant effect on the orbit of Šteins, decaying its semi-major axis by 16.4 km after 242.2 years and by up to 5,365 km in 50,000 years. This reinforced the notion that the Yarkovsky effect needs to be considered for asteroids in the sub ~20 km mean diameter range (3). However, the Yarkovsky effect can be highly dependent on the shape of the asteroid. Although the Yarkovsky effect affects the orbit of 2867 Šteins, it was not a significant force on the orbit of Šteins unless considered in the scale of orbital maneuvers. Therefore, we rejected our hypothesis that the Yarkovsky effect will push 2867 Šteins into a Kirkwood gap within 50,000 years. Future studies can analyze the seasonal effect and include more specific factors that affect the Yarkovsky force, such as the scattering and reabsorption of light. The exclusion of these factors created a source of error due to the simplification of the system to create a computer simulation, but the results from the simulation still provided insight on the magnitude and effect of the Yarkovsky effect on 2867 Šteins.

The resulting direction of the tangential force at each position matched the hypothesized direction, against the motion of the asteroid. However, the tangential force's magnitude varied between positions, with a range of 0.719 N. We hypothesized that this variation was due to variation in the asteroid's position in the z-direction, distance from the Sun, and shape. More investigation is necessary to analyze the precise causes of this variation.

METHODS

In this study, pressure from solar radiation was ignored as previous research revealed that it does not significantly alter the semi-major axis of an asteroid's orbit when considered with the Yarkovsky effect (8). Equation (1) represents the Yarkovsky force over the surface of the asteroid (9):

$$\vec{f} = -\frac{2\sigma}{3c}\oint \varepsilon T^4 \vec{n}\, ds \quad (1)$$

where c was the speed of light, σ was the Stefan-Boltzmann constant, ε was the emissivity of the surface, T was the temperature of the surface, n was the normal vector to the surface, and ds was the differential area element.

YORP, or the Yarkovsky–O'Keefe–Radzievskii–Paddack effect, is the torque that the Yarkovsky effect creates (2). When the Yarkovsky effect acts on asymmetrical bodies, it generates a net torque, causing the body to accelerate about an axis (2). This spin continuously changes the Yarkovsky force, as the rotational state (axis of rotation, period of rotation, etc.) largely determines the direction and magnitude of the Yarkovsky force (2). Equation (2) represents the YORP torque generated over the surface of the asteroid (9):

$$\vec{T} = -\frac{2\sigma}{3c}\oint \varepsilon T^4 \vec{x} \times \vec{n}\, ds \quad (2)$$

where x was the vector from the center of the body's mass to the surface. The YORP torque was not considered in the simulation of the Yarkovsky force for simplification. The results indicate that the YORP torque can reasonably be ignored because even over the time span of one gigayear, the change in angular velocity will be less than 10^{-4} percent, assuming a constant YORP torque. However, more investigation is needed to prove the insignificance of the YORP effect on 2867 Šteins.

The surface temperature of 2867 Šteins was required to quantify the Yarkovsky effect. As a result, the first step was to create a thermal map of the asteroid. The methods and equations used to compute the thermal map are modeled off of the Simple Thermal Model described by Rozitis and Green (6). The specific methods are detailed throughout the section. A stereolithography (STL) file of Šteins is made up of 1500 triangular facets, representing the surface of Šteins (**Figure 4**). The thermal map was partitioned into 50 depth-steps per facet and 400 time-steps per rotation. As Rozitis and Green demonstrate, the 50 depth-steps equally divide the depth from the surface to $2l_{2\pi}$, defined in Equation (3).

$$l_{2\pi} = \sqrt{\frac{4\pi P k}{\rho C}} \quad (3)$$

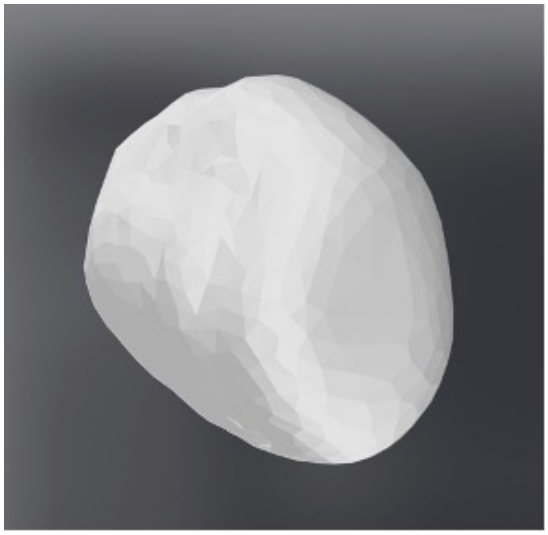

Figure 4: 3D model of 2867 Šteins. An image of the STL file of 2867 Šteins partitioned into 1500 triangular facets.

$l_{2\pi}$ was the thermal skin depth, the depth where the internal temperature lags by 2π and the amplitude of the temperature decreases by a factor of $e^{-2\pi}$ (6). The 400 time-steps equally divide P_{ROT}, or the rotation period of the asteroid.

The goal of the thermal model was to determine the temperature of each facet at any given point in the rotation. For simplicity, only 1-D heat conduction was considered, similar to Rozitis and Green (6). The thermal map was created based upon the surface boundary condition imposed by conservation of energy,

$$\left(1-A_B\right)\left(\left[S(\tau)\right]\psi(\tau)F_{SUN}\right)+\frac{\Gamma}{\sqrt{4\pi P_{ROT}}}\left(\frac{\partial T}{\partial z}\right)_{z=0}-\varepsilon\sigma T^4{}_{z=0}=0 \quad (4)$$

where A_B was the Bond albedo, $S(\tau)$ indicates whether the facet was shadowed with a 0 or a 1, Γ represents the thermal inertia, ψ(τ) returns the cosine of the Sun illumination angle, and F_{SUN} was the integrated solar flux (10) at the distance of the object, which was given by $(1367/r^2)W/m^2$ where r was the heliocentric distance of the planetary body in AU. Unlike Rozitis and Green (6), F_{SCAT} and F_{RAD} are ignored because Šteins was primarily convex, so the intensity of the light reflected and reabsorbed by the asteroid was significantly smaller than the light from the Sun. z was the unitless normalized depth variable given by

$$z=\frac{x}{\iota_{2\pi}} \quad (5)$$

and τ is the unitless normalized time variable, given by

$$\tau=\frac{t}{P_{ROT}} \quad (6)$$

Based on these relationships, the initial mean surface temperature of each facet was found using Equation (7).

$$\left\langle T_{z=0}\right\rangle_1=\left(\frac{\left(1-A_B\right)}{\varepsilon\sigma}\right)^{1/4}\frac{\int_{\tau=0}^{1}\left(\left[1-S(\tau)\right]\psi(\tau)F_{SUN}\right)^{1/4}d\tau}{\int_{\tau=0}^{1}d\tau} \quad (7)$$

S(τ) determines which facets receive light by determining whether any other facets block light from reaching it. To calculate $\psi(\tau)$, the scalar product of the vector normal to each facet and the vector representing the Sun's ray was used to find $cos(\theta)$. The solutions for $<T_{z=0}>_1$ give the mean surface temperature of each facet over one period, which was equated to the temperatures of each respective facet and its depth steps at τ = 0. After recalculating the surface temperature at τ = 0 using Equation (4) and the value from $<T_{z=0}>_1$, the temperature at τ = 0 was calculated at each depth step. The equation

$$T_{i,j+1}=T_{i,j}+\frac{1}{4\pi}\frac{\delta\tau}{(\delta z)^2}\left[T_{i+1,j}-2T_{i,j}+T_{i-1,j}\right] \quad (8)$$

was used where i = 1 to n depth-steps and j = 1 to m time-steps. δτ represents the length of the normalized time steps, and δz represents the length of the normalized depth steps. Equation (8) is a difference equation developed to locally approximate the differential equation for 1-D heat conduction, given by:

$$\frac{\partial T}{\partial \tau}=\frac{1}{4\pi}\frac{\partial^2 T}{\partial z^2} \quad (9)$$

The last depth step is set equal to the second-to-last depth step in order to satisfy the internal boundary condition

$$\left(\frac{\partial T}{\partial z}\right)_{z\to\infty}\to 0 \quad 10)$$

This process of iterating from the surface to the last depth-step, calculating the temperature of each depth-step for the next time-step, was repeated for at least ten full rotations and until the change in the surface temperature for the same time position was less than 0.01 to ensure that the thermal map comes to a steady state. After testing, 0.01 was chosen as the limit because it appeared the most computationally feasible, while maintaining a high level of accuracy.

The thermal map was used to calculate the Yarkovsky effect. We simulated this force within NASA's GMAT vR2020a Orbital Determination software to determine the resulting change in the orbit of Šteins (7).

We wrote all code in Python 3.6 using a class-based subsumption architecture structure. The basic structure of the code was as follows: using physical properties of 2867 Šteins, the code outputs a thermal map that generates a Yarkovsky vector that we inputted into NASA's GMAT orbital simulation software (7).

The asteroid radius, Bond albedo, density, mass, thermal conductivity, thermal inertia, position, rotation period, and spin are major factors in determining the Yarkovsky effect on 2867 Šteins. The physical parameters of Šteins are well-known and documented (**Table 3**). However, some values, such as mass and thermal conductivity, are not explicitly documented. The thermal conductivity of Šteins was estimated based on the similarity of its surface composition to enstatite (11). Given that enstatite has a thermal conductivity of approximately 4.5 W m/K (12), the thermal conductivity of Šteins was approximated as 4.5 W m/K. The mass was found by multiplying the recorded density and volume of Šteins.

A *Rays* class representing vectors of sunlight hitting the asteroid was created first. To determine which facets are shadowed, we created the class *Shadowing* with two conditions. First, all facets that faced directly away from the Sun were shadowed. We found this comparing the normal vector of each facet to the vectors of sunlight. Second, shadowing was detected in the remaining facets by determining which facets the rays intersect. This was found by calculating the signed volume of various tetrahedrons. These tetrahedrons have 5 points, including the 3 vertices of the facet and 2 random points on the ray. Once it was determined which rays intersect which facets, the code then determined which facet was intersected first using the parametric equation for the ray. If a ray of light intersected one facet before another, then the other facet that would have been hit by that ray of light was

Property	Value
Mean Radius (13)	2.7 km
Bond albedo (12)	0.24
Density (13)	1800 kg/m^3
Mass (13)	$1.368\cdot10^{14}$ kg
Thermal Conductivity (14)	4.5 W·m/K
Thermal Inertia (15)	110 J/m^2·K·s$^{1/2}$
Emissivity (15)	0.73
Position (15)	N/A
Rotation Period (15)	6.0468 hours
Spin (11)	(250.0°, −89.0°) in ecliptic coordinates

Table 3. Physical Properties of the Asteroid 2867 Šteins. The physical properties of 2867 Šteins used in the simulation of the thermal map.

"shadowed."

One addition to the shadowing class was the angle functions *phi()* and *orient()*. *phi()* returned the cosine of the angles between the normal vectors of each facet and the rays from the Sun by dividing the dot product of the normal vectors and the Sun rays by the product of the lengths of both vectors. *orient()* oriented the asteroid's north and south poles in the STL file in the direction that they are oriented in 3-D space, taking the XY-axis as the ecliptic plane. These methods were implemented in the shadowing, angle, and thermal map code. The thermal map code imported the *Rays* and *Shadowing* classes. The methods described were used to determine the temperature of each facet at different times.

Each point in an asteroid's orbit had a unique Yarkovsky and YORP vector assigned to it, based on its distance from and orientation to the Sun. To determine the Yarkovsky force vector, the thermal map of Šteins was imported, and the force due to thermal emission on the asteroid is evaluated at each time step using the approach outlined in Equation (1). The surface integral represented the net force on the asteroid at a single time step. Iterating over the entire rotation and averaging these values yielded the representative Yarkovsky force vector for that position in space. A similar approach was taken for the YORP vector, using Equation (2). The torques for all facets were taken with respect to the center of mass of the asteroid, which is given in the mass properties of the STL file. These processes were repeated for six locations to simulate the variation in the force throughout the orbit, resulting in six different vectors.

To determine the change to 2867 Šteins' orbit, NASA's GMAT software was used (7). The asteroid was simulated as a spacecraft with the Yarkovsky vector as the thrust vector. Each of the six different vectors was inputted at their respective locations. We ran the simulation for 242.2 years, using the integrator RungeKutta89 and an initial step size of 10. Microsoft Excel's FORECAST.ETS function was used on the resulting data to extrapolate the results to longer periods of time. Then, Excel's FORECAST.ETS.CONFINT was used to calculate the 95% confidence interval for the forecasted value. All astronomical measurements were taken and determined in heliocentric ecliptic cartesian coordinates.

All code for this paper can be found here: https://github.com/rnucuta/orbitalResonanceResearch.

ACKNOWLEDGEMENTS

The theory behind the Yarkovsky effect in this study was aided by the guidance of Dr. Simon Green of the Open University. We deeply appreciate the guidance of Dr. Green and the JEI editorial staff.

Received: June 12, 2020
Accepted: November 23, 2020
Published: January 26, 2021

REFERENCES

1. Whitwam, Ryan. "NASA: Asteroid Could Still Hit Earth in 2068." ExtremeTech, 28 Oct. 2020, www.extremetech.com/extreme/316690-nasa-asteroid-could-still-hit-earth-in-2068.
2. Vokrouhlicky, David, and William F. Bottke. "Yarkovsky and YORP Effects." Scholarpedia, 2012, www.scholarpedia.org/article/Yarkovsky_and_YORP_effects.
3. Bottke, William F., *et al.* "THE YARKOVSKY AND YORP EFFECTS: Implications for Asteroid Dynamics." Annual Review of Earth and Planetary Sciences, vol. 34, no. 1, 16 Jan. 2006, pp. 157–191., doi:10.1146/annurev.earth.34.031405.125154.
4. "ASTEROID (2867) Šteins." ESA Science & Technology - Asteroid (2867) Šteins, European Space Agency, 1 Sept. 2019, sci.esa.int/web/rosetta/-/43356-2867-Šteins.
5. "Kirkwood Gap: Facts, Information, History & Definition." The Nine Planets, 5 Mar. 2020, nineplanets.org/kirkwood-gap/.
6. Rozitis, B., and S. F. Green. "Directional Characteristics of Thermal-Infrared Beaming from Atmosphereless Planetary Surfaces - a New Thermophysical Model." Monthly Notices of the Royal Astronomical Society, vol. 415, no. 3, June 2011, pp. 2042–2062., doi:10.1111/j.1365-2966.2011.18718.x.
7. General Mission Analysis Tool (Version R2020a) [Computer software]. (2020, April 29). Retrieved from https://gmat.atlassian.net/wiki/spaces/GW/overview?mode=global.
8. Deo, S.n., and B.s. Kushvah. "Yarkovsky Effect and Solar Radiation Pressure on the Orbital Dynamics of the Asteroid (101955) Bennu." Astronomy and Computing, vol. 20, 2017, pp. 97–104., doi:10.1016/j.ascom.2017.07.002.
9. Pelaez, Jesus, *et al.* "A New Approach on the Long Term Dynamics of NEO's Under Yarkovsky Effect." Advances in the Astronautical Sciences , vol. 140, no. 11-440, Dec. 2011, doi: 2011AdAnS.140..440P.
10. Kopp, Greg, and Judith L. Lean. "A New, Lower Value of Total Solar Irradiance: Evidence and Climate Significance." Geophysical Research Letters, vol. 38, no. 1, 2011, doi:10.1029/2010gl045777.
11. Barucci, M. A., *et al.* "Asteroids 2867 Šteins and 21 Lutetia: Surface Composition from Far Infrared Observations with the Spitzer Space Telescope." Astronomy & Astrophysics, vol. 477, no. 2, Dec. 2007, pp. 665–670., doi:10.1051/0004-6361:20078085.
12. Sj, C. P. Opeil, *et al.* "Stony Meteorite Thermal Properties and Their Relationship with Meteorite Chemical and Physical States." Meteoritics & Planetary Science, vol. 47, no. 3, 2012, pp. 319–329., doi:10.1111/j.1945-5100.2012.01331.x.
13. Spjuth, S., *et al.* "Disk-Resolved Photometry of Asteroid (2867) Šteins." Icarus, vol. 221, no. 2, Nov. 2012, pp. 1101–1118., doi:10.1016/j.icarus.2012.06.021.
14. Leyrat, C., *et al.* "Thermal Properties of the Asteroid (2867) Šteins as Observed by VIRTIS/Rosetta." Astronomy & Astrophysics, vol. 531, 1 May 2011, doi:10.1051/0004-6361/201116529.
15. Park, Ryan, and Alan Chamberlin., "HORIZONS Web-Interface." JPL's Horizon system. 3 May 2020.

JOURNAL OF
EMERGING INVESTIGATORS

Article

Analysis of patterns in the harmonics of a string with artificially enforced nodes

Armaan Jain[1], Curtis Broadbent[2]
[1]Good Shepherd International School, Tamil Nadu, India
[2]Eisco Scientific North America, Victor, New York

SUMMARY

This study examines the higher harmonics in an oscillating string by analyzing the sound produced by a guitar with a spectrum analyzer. Higher harmonics of a string are simultaneously oscillating modes which have frequencies that are integer multiples of the fundamental frequency of the string. These harmonics can be viewed on an audio spectrum analyzer. They are always present in an oscillating string and contribute to its timbre and tonal quality. Specific higher harmonics can be produced directly by placing nodes (points where the string cannot oscillate) at different lengths along a string. The tone thus produced lacks the fundamental frequency but also has a very different harmonic structure. In a guitar string, for example, it is this harmonic structure which gives rise to the very different tonal quality of a plucked harmonic as compared to the directly excited pitch of the same frequency. We mathematically hypothesized that the higher harmonics in the series of the directly excited 2nd harmonic contain the alternate frequencies of the fundamental series, the higher harmonics of the directly excited 3rd harmonic series contain every third frequency of fundamental series, and so on. We also verify a simple mathematical relationship between two different harmonic series arising from two different boundary conditions that feature the same fundamental mode. To test our hypotheses, we enforced artificial nodes to excite the 2nd, 3rd, and 4th harmonics directly, and analyzed the resulting spectrum to verify the mathematical hypothesis. The data analysis corroborates both hypotheses.

INTRODUCTION

When we pluck a string in tension, a series of frequencies greater than the fundamental frequency is observed. Here the fundamental frequency is calculated using the string's wave speed and the string length. Theoretically, however, exciting the fundamental mode (the lowest or the "true" frequency) of a string in tension should not produce overtones (any higher frequency standing waves). In practice a range of overtones are produced, from which the non-resonant modes (frequencies that are not an integer multiple of the fundamental mode) decay quickly, while the fundamental mode and the harmonic overtones (frequencies that are part of the harmonic series i.e., are integer multiples of the fundamental mode) persist.

The modes whose frequencies are multiples of the fundamental frequency are called the higher harmonics. When we calculate the wave frequency using wave speed and wavelength, the result is only the fundamental frequency. However, in a string with closed ends, this is not a complete representation of the frequencies that can be supported. For the complete picture, the fundamental frequency can be used to find the higher harmonic frequencies. This is done by multiplying the fundamental mode by consecutive integers. This paper explores patterns existing in these higher harmonics of standing waves that can help us predict the resonant frequencies in a given system. This knowledge can be essential in many engineering applications from electrical power systems (1) to acoustics.

First, we derive a relationship between the frequency of the fundamental mode and its harmonics and then experimentally test that hypothesis. **Figure 1A** represents the fundamental mode of the open guitar string. The wavelength is twice the length of the oscillating string. **Figure 1B**, **1C** and **1D** show the 2nd, 3rd, and 4th harmonics of this string. The 2nd harmonic has a wavelength that is equal to half of the wavelength of the fundamental. The 3rd harmonic has a wavelength that is a third of the wavelength of the fundamental, and this pattern repeats for higher-order harmonics.

In this way, the wavelength of the n^{th} harmonic in the series is given by $\lambda_n = 1/n \times \lambda$. Here, λ is the wavelength of the fundamental excited mode. Using the general relationship between wavelength, frequency, and the constant velocity of the string wave $v = \lambda_n f_n$, we can calculate the frequency for all the higher harmonics on this string using Equation 1,

$$f_n = nv/\lambda = nf. \quad (1)$$

Using this method, we see that the frequencies of the harmonics are multiples of the fundamental frequency, as n is an integer. This is consistent with the idea that the frequency of higher harmonics of a string are the whole number multiples of the fundamental frequency.

If we examine the two nodes in **Figure 1A** we see they are placed such that every other wave has its nodes at these points. Therefore, all the three waves (part B, C and D) may

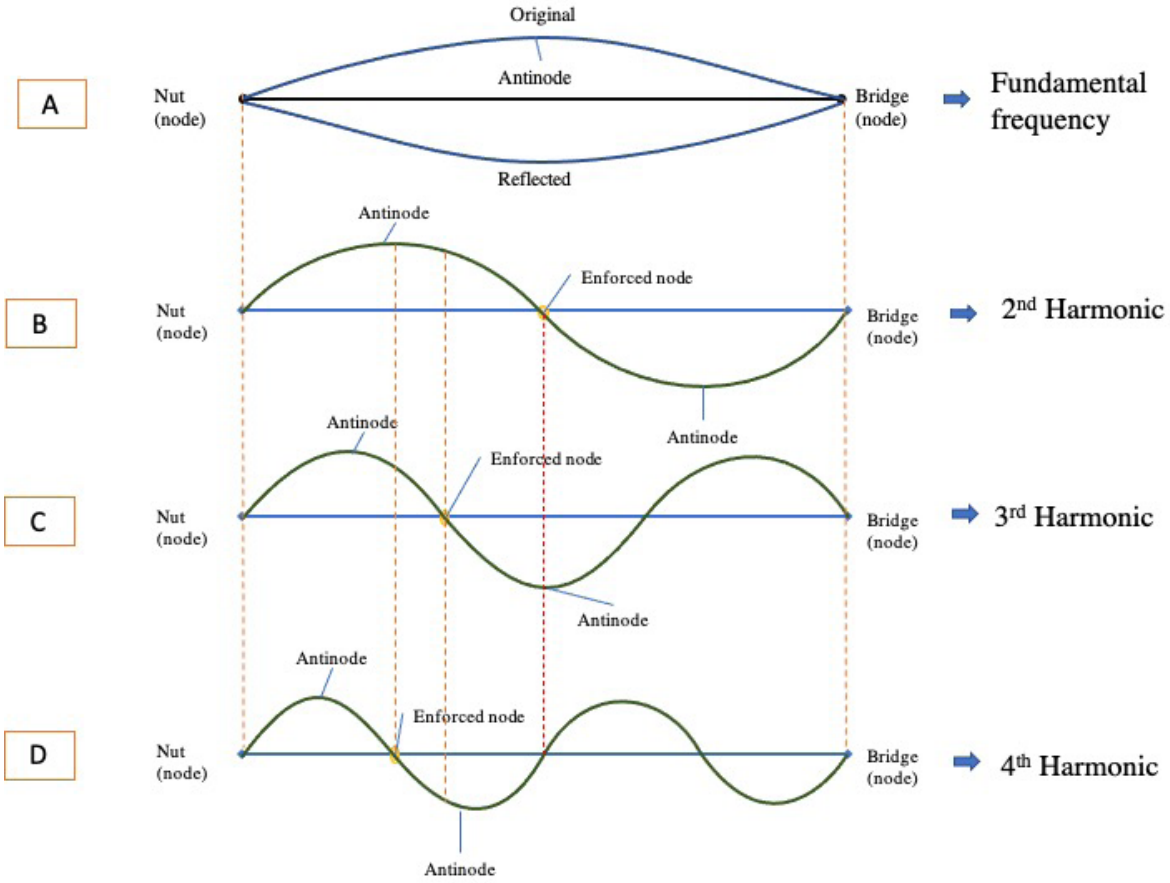

Figure 1. Schematic of the string of a guitar clamped on both ends (neck and bridge) without any artificially enforced nodes. These ends offer no lateral movement of the string, enforcing fixed nodes and providing the boundary conditions for the lowest frequency in the study. Part A, B, C and D are the 1st, 2nd , 3rd, and 4th harmonics respectively. The point labelled "enforced node" shows the point where the artificial node was enforced. This is half the length of the string from the neck for the 2nd harmonic, one third the length of the string for the 3rd harmonic, and one fourth the length of the string for the 4th harmonic. The dotted line is a projection of the nodes onto the other modes. When an enforced node of one mode lines up with a node of another mode, the modes can co-exist when the node is enforced. When this is not the case, the modes cannot co-exist when the node is enforced.

propagate without any destructive interference from nodes of the fundamental frequency in **Figure 1**.

Now, consider the 2nd and 3rd harmonics. In addition to appearing when the fundamental mode is excited, the 2nd and 3rd harmonics can be excited by enforcing a "node" at the locations given. However, enforcing an artificial node can cause problems for other modes in the system. The point labeled "enforced node" in the 2nd harmonic's graph is at the antinode of the 3rd harmonic (**Figure 1**). When the 2nd harmonic is produced, the artificial node does not permit the antinode to form at that point for the 3rd harmonic. Meanwhile, the node for the 4th harmonic is in line with the enforced node of the 2nd harmonic; thus, the 4th harmonic propagates without any restrictions from the enforced node of the 2nd harmonic.

In terms of integers, when we enforce the node for the 2nd harmonic, the 4th harmonic is also present in the series, while the 3rd harmonic is not. We can extrapolate this principle to higher order modes, as shown in **Table 1**, which shows that when the 2nd harmonic is excited using an enforced node, the harmonic frequencies and the alternate frequencies of the higher harmonics of the fundamental mode are the same.

We can derive these relationships mathematically from the fundamental properties of waves. Before doing so, it is important to define the terms that we will use. Modes refer to solutions of the wave equation on a string with specific boundary conditions. The fundamental mode of a guitar string is the lowest frequency mode of a string that is clamped at two ends. The higher-order modes are solutions to the wave equation with the same boundary conditions. When another node is enforced somewhere on the string, this additional boundary condition would result in a different set of solutions for the wave equation, even though they might have the same frequency as harmonics of the string with no enforced node. Therefore, in the following text, we will refer to harmonics of the excited mode as the series with the additional boundary condition to distinguish between these different sets of solutions.

Consider when an enforced node is used to excite the 3rd harmonic of the base mode with a frequency of 300 Hz. Integer multiples of the frequency would be 300 Hz, 600 Hz,

Table 1. Hypothetical harmonic series to explain the hypothesis.

Fundamental frequency 100 Hz	Fundamental frequency 200 Hz
100 Hz	
200 Hz	200 Hz
300 Hz	
400 Hz	400 Hz
500 Hz	
600 Hz	600 Hz
700 Hz	
800 Hz	800 Hz
900 Hz	
1000 Hz	1000 Hz

Note: Summary of data collected compared to the theoretically derived frequencies. Three sets of trials were conducted for each boundary condition, and each frequency value given in this table is the average of these three trials. The frequencies are the peak values discussed in ***Figure 3*** *and are the overtones for each boundary condition. The data has been placed alongside the theoretically predicted values in such a way that a frequency value in the empirical data that is close to or the same as the theoretically predicted value are in the same row.*

900 Hz, and so on. These are all 3rd multiples of the higher harmonic frequencies of the fundamental or base mode of 100 Hz. This can be generalized as follows: the relationship of the harmonics arising from different excited modes to a related fundamental mode can be found for two different boundary conditions, where the frequency of the fundamental mode from one set of boundary conditions is divisible by the frequency of the fundamental mode of another set of boundary conditions by a factor of n. In this case, the harmonic series with the higher fundamental frequency will contain harmonics which are every n^{th} multiple of the lower frequency.

For example, enforcing a node in the center of the string gives a fundamental excited mode with a frequency of 200 Hz. The second harmonic of the excited mode has a frequency of 400 Hz. With no enforced node, the fundamental excited frequency is 100 Hz, with the 2nd and 4th harmonics having frequencies of 200 Hz and 400 Hz, respectively. Thus, the fundamental frequency with the added boundary condition, which is twice the fundamental frequency in the original string, has a harmonic series comprising every second (or every alternate) frequency of the harmonic series of the original string.

We will now explore how the harmonics of the string with no enforced node are related to the harmonics of the same string with an enforced node. The relationship between the harmonics arising from different excited modes can be explained as follows: for any fundamental frequency, f, the frequency of the n^{th} harmonic of the m^{th} mode excited using an enforced node for the m^{th} mode is the same as the m^{th} harmonic of the n^{th} mode excited using an enforced node for the n^{th} node. A mathematical derivation is shown in Equations 2-4. For the fundamental or base mode, f_1, the frequency, f_n, of its n^{th} harmonic is

$$f_n = f_1 n. \quad (2)$$

If we excite the n^{th} harmonic directly by using an artificially enforced node, then the frequency, f_{mn}, of the m^{th} harmonic of that n^{th} mode excited using an enforced node is

$$f_{mn} = f_n m. \quad (3)$$

Now, substituting f_n in the equation we get

$$f_{mn} = f_1 nm. \quad (4)$$

Notice that for the multiplication of f_1, the numbers n and m can be switched without making a difference to the product. This means that $f_{mn} = f_{nm}$. As a result, we may say, for example, that the frequency of the 2nd harmonic of the fundamental mode excited with an enforced node at the position of a node of the 3rd harmonic of the string's fundamental mode (with no enforced nodes) is the same as the 3rd harmonic of the fundamental mode excited with an enforced node at the position of a node of the 2nd harmonic of the string's fundamental mode. Through data analysis of the harmonic series produced using a guitar string, we found that both these theoretical patterns are valid in scenarios where the wave equation applies, and therefore can be used to predict the resonant frequencies in other systems.

RESULTS

We performed an experiment to validate the hypothesis derived above. The data was collected with a guitar and a phone-based frequency spectrum analyzer.

To verify the presence of the alternating pattern, we excited the harmonics directly, using the frets of a guitar as markers. Frets are metal bars on the guitar fingerboard used to control pitch. First, the high E string was tuned to a base mode of 330 Hz. The 2nd harmonic was produced by enforcing a node on the 12th fret, halfway through the string. This did not allow the string to oscillate at that point. The 3rd harmonic was produced by enforcing a node at the 9th fret, one-third of the string length. The 4th harmonic was produced by enforcing a node at the 7th fret, a quarter of the length of the string. The frequencies at which there were peaks in the graph were recorded in three separate trials. **Table 2** shows the average of these three trials to the nearest whole number. The theoretical values in **Table 2** were computed using the following calculation. The measured length of the string between the two ends was 0.648 m, and the speed of the wave is given by $v = \lambda f$. λ here was twice the distance between the two ends of the string 1.296 m. The wave speed was therefore equal to 427.68 ms^{-1}. The speed of a wave on a string is dependent only on the tension and linear density of the string (2). Since both of these parameters are constant, the wave speed is constant for all harmonic frequencies. We can then determine the wavelength of each wave by using the wave speed.

Figure 2 is a screenshot of the spectrum analyzer from the phone, showing a graph of frequency (Hz) on the x-axis

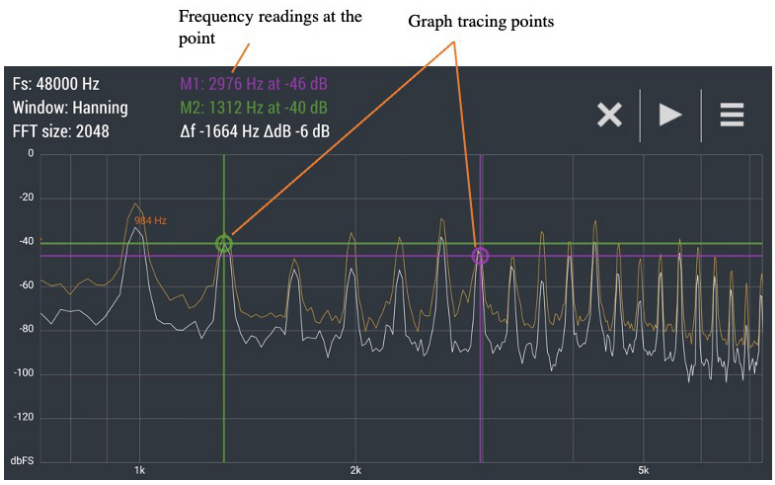

Figure 2. Graph of frequency against loudness for a standing wave as given by the spectrum analyzer app, showing how the data in Table 2 was collected. Each peak here is the overtone of the respective harmonic series, and we used a graph tracing feature to determine the frequency at these peaks. The 'peak hold' records initial graph as the sound fades away with time. This was used as a guiding graph to trace. The pause button allowed us to stop the application from collecting further samples, giving enough time to record the peak frequencies accurately.

Table 2. Summary of data collected compared to the theoretically derived frequencies.

Theoretical	Fundamental frequency peak frequency average	2nd Harmonic peak frequency average	3rd Harmonic peak frequency average	4th harmonic peak frequency average
330	328			
660	658	659		
990	990		989	
1320	1318	1318		1321
1650	1647			
1980	1976	1977	1979	
2310	2303			
2640	2633	2639		2638
2970	2964		2970	
3300	3296	3300		
3630	3625			
3960	3964	3961	3958	3963
4290	4285			
4620	4620	4623		
4950	4959		4963	
5280	5283	5282		5286
5610	5613			
5940	5947	5948	5948	
6270	6270			
6600	6602	6610		
6930	6931		6949	
7260	7258	7263		
7590	7608			
7920	7926	7939		
8250	8269			
8580	8589	8597		
8910	8937			
9240	9253	9275		
9570	9608			

Note: Three sets of trials were conducted for each boundary condition, and each frequency value given in this table is the average of these three trials. The frequencies are the peak values discussed in ***Figure 2*** *and are the overtones for each boundary condition. The data has been placed alongside the theoretically predicted values so that a frequency value in the empirical data that is close to or the same as the theoretically predicted value is in the same row.*

against loudness (dB) on the y-axis. A tracking feature was used to manually find the loudest frequency, corresponding to the peak. The frequency at these 'peaks' were recorded.

The spectrum in **Figure 2** has peaks at frequencies greater than 330 Hz. This verifies the presence of higher harmonics in a vibrating string. **Table 2** summarizes the data collected (loudest frequencies), including the theoretical values and the average values for fundamental, 2nd, 3rd and 4th harmonic series, placed such that the same frequency is in the same row. The empirical frequencies were entered into the chart in the row that had the closest theoretical harmonic frequency.

With this approach, we can see that every other box in the 2nd harmonic column is filled, every third box in the 3rd harmonic column is filled, and every fourth box in the 4th harmonic column is filled. This agrees with the results of our theoretical analysis. Moreover, if we consider the common frequencies, the frequency of the 3rd harmonic (row 6) in the 2nd harmonic peak frequency column is the same value as the 2nd harmonic in the 3rd harmonic peak frequency column. This example corroborates the hypothesis that $f_{mn} = f_{nm}$.

DISCUSSION

Our data analysis verifies the presence of higher harmonics generated by a plucked string. It also shows that there is a pattern in different harmonic series, provided they stem from the same fundamental series.

The deviation from the theoretical values increased at higher frequencies because the amplitude of the harmonics was much lower. As a result, background noise lead to measurement errors for these frequencies. To avoid this error, the background noise spectrum was initially noted, and once the spectra approached the loudness of the background noise, the peak frequencies were not recorded. Since the plot was analyzed for the peaks over time, the background noise was too soft to affect the peaks at lower frequencies. Furthermore, the limitations posed by the phone's microphone and operating system (OS) would enhance this uncertainty. Most smartphone microphones and OS's are optimized for human voice and features like automatic gain control aim to reduce any deviations from a normal human voice. Therefore, the higher frequencies, which were not in a normal person's vocal range, may be altered by the operating system or may not be captured accurately by the microphone, since they lay beyond its required standards (3).

For the discrepancies in the peaks, a source for this could be the plot tracing technique, which was manual and not computerized, leaving scope for human error. Another potential source is the tuning of the string. While the instrument was tuned, and the sound was analyzed using the same device to prevent differences in the hardware, the device's scope for inaccuracy in both the hardware and the two applications – the tuning app and the spectrum analyzing app – could have resulted in these errors.

There were two ways of considering the error propagation: the error in theoretical values and the error in the measured values. The uncertainty in a theoretical fundamental frequency (A) of ΔA can be propagated for harmonic frequency f, where $f = kA$, as $\Delta f = k \times \Delta A$.

Here, k is an integer that takes the value of the harmonic. (for example, for the 3rd harmonic $k = 3$).

This way, if the first harmonic had an uncertainty of 1 Hz, the second would be predicted to have an uncertainty of 2 Hz, the third would be predicted to have an uncertainty of 3 Hz, and so on for the theoretical values. In this way, the theoretical model predicts higher uncertainty at higher frequencies.

The theoretical value was based on the idea that the guitar tuner tunes the instrument to 330 Hz. The uncertainty in this value could not be determined. However, if we considered the uncertainty in the fundamental frequency of the first data set, we could get a decent approximation of the margin of error of this 330 Hz fundamental value. The three values for the fundamental frequency were measured as 328 Hz, 331 Hz and 328 Hz. This gave a mean value of 329 Hz with a standard deviation of 1.73 Hz – this was the uncertainty. This uncertainty was used to predict the uncertainty of the 29th harmonic using equation 5. We calculated an uncertainty of 50.17 Hz, which can be taken as the approximate uncertainty in the theoretical frequency value of the 29th harmonic (9570 Hz). Consequently, the theoretically calculated frequency is 9570 ± 25.09 Hz, and the measured frequency is 9608 ± 10.21 Hz. Thus, the mean measured value is very close to what was predicted. The remaining discrepancy might be attributable to nonlinearities of the physical string, but this is outside the scope of the present study.

The uncertainty in the peak width needs consideration as well. The peaks were not exactly sharp, but instead showed a short flat region when zoomed in. The approximate middle of these peaks was taken, and the corresponding frequency was noted, leading to additional error that is not directly assessed in the calculation above.

While the methodology focused on string harmonics, instrument strings are not the only application of higher harmonics. In practice, standing waves occur almost everywhere, from electrical systems to wind blowing through a narrow tunnel. Being able to predict all resonant frequencies, which can potentially harm an electronic device or the structure of a tunnel, is key to successful engineering. As for music, musicians capitalize on higher harmonics for better, more varied tones, which can be utilized to create dynamic songs.

METHODS AND MATERIALS

Node enforcer

To ensure consistency in the excited mode created by enforcing a node, we designed a node-enforcer. The node enforcer uses the concept of dampening strings to enforce points where oscillation is restricted.

The enforcer (see **Figure 3**) was 3D printed in Acrylonitrile butadiene styrene (ABS) plastic. After this, the side with the central cut was covered in paper tape. The cut in the base

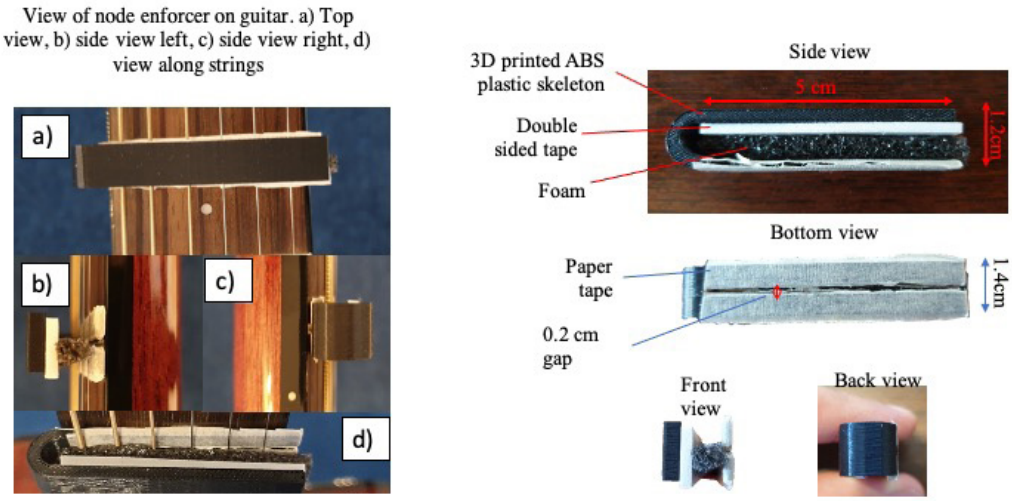

Figure 3. Dimensions of the node enforcer. The node enforcer that was used to enforce the artificial nodes for the study and was designed to fit the guitar used.

allowed it to be clipped onto a fret without any change in the height of the string (and thus maintain constant length, tension, and wave speed). Then, a thin piece of foam was stuck to the other upper end, such that it reached the lower end. The foam acted as a dampener and prevented any oscillation at the point of contact by absorbing the energy at that point, enforcing a node.

Spectrum analyzer

We found the loudest frequencies in the spectrum by 'pausing' the sampling of the spectrum in time and then using the inbuilt tracing feature to trace the plot and determine the individual frequencies for each peak manually.

The spectrum analyzer used was the *Advanced Spectrum analyzer PRO by Vuche.* This FFT (Fast Fourier transform) software, with the input samples set at 16384, the averaging factor at 3, and the sampling frequency at 48000 Hz, converted sound into a logarithmic scale graph. The app had "peak hold" and "graph tracing" features, which allowed for both identifying and quantitively obtaining the loudest frequencies - the higher harmonics.

Guitar

The sound was produced using a mahogany body guitar with a 25.5-inch-long scale (scale is the string length), walnut fingerboard, stainless steel frets, walnut bridge, and a crème plastic nut (4). The string used was a bronze string with a gauge size of 0.10 (diameter of 2.542 mm). The manufacturer states that these bronze strings were formed by wrapping an 80% copper and 20% zinc wire around hex shaped, brass plated steel core wire (5). The high E string was played using a Duralin, 1.00 mm thick plectrum. The frequencies were recorded with relative loudness, as loudness is subject to how hard one plucks the string, and this varies from human to human. Moreover, the exact position of the node is subject to error, thus repetitions were performed to minimize this random error.

In summary, the method to record harmonic peaks was as follows: 1) note the background noise, 2) enable peak hold, 3) play a note, 4) pause the spectrum, and 5) use the tracer to find the frequencies of the peaks (loudest) in the spectrum. This was performed thrice for each boundary condition, and the average of these was taken for **Table 2** and the standard deviation of these three values was the uncertainty in the measurement.

Received: October 9, 2020
Accepted: January 20, 2021
Published: January 28, 2021

REFERENCES

1. "Detect and Eliminate Harmonics: Why?" *Electrical Installation Guide*, 20 Dec. 2019, www.electrical-installation.org/enwiki/Detect_and_eliminate_harmonics:_why%3F. Accessed 23 Aug. 2020.
2. OpenStax. "16.4: Wave Speed on a Stretched String." *Physics LibreTexts*, 2016, phys.libretexts.org/Bookshelves/University_Physics/Book%3A_University_Physics_(OpenStax)/Map%3A_University_Physics_I_-_Mechanics_Sound_Oscillations_and_Waves_(OpenStax)/16%3A_Waves/16.04%3A_Wave_Speed_on_a_Stretched_String. Accessed 12 Sept. 2020.
3. Faber, Benjamin M. "Acoustical Measurements with Smartphones: Possibilities and Limitations." *Acoustics Today (Volume 13, issue 2)*, 2017, pp. 10-16.
4. Fender Guitars. "CD-60SCE Dreadnought, All-Mahogany." *Shop Fender | Electric Guitars, Acoustics, Bass, Amps and More*, shop.fender.com/en-US/acoustic-guitars/dreadnought/cd-60sce-dreadnought-all-mahogany/0970113022.html. Accessed 13 July 2020.

5. Ernie ball. “Earthwood 80/20 Bronze Acoustic Guitar Strings.” *Ernie Ball Acoustic Guitar Strings*, www.ernieball.com/guitar-strings/acoustic-guitar-strings/earthwood-8020-bronze-acoustic-guitar-strings#P02008. Accessed 13 July 2020.

JOURNAL OF
EMERGING INVESTIGATORS

Article

Can Green Tea Alleviate the Effects of Stress Related to Learning and Long-Term Memory in the Great Pond Snail (Lymnaea stagnalis)?

Madison Elias[1], Janine Cupo[1]
[1]Seaford High School, Seaford, New York

SUMMARY

Stress and anxiety have become more prevalent issues in recent years and teenagers are especially at high risk. Recent studies show that experiencing stress while learning can impair brain-cell communication, thus inhibiting learning. Green tea is believed to have the opposite effect, aiding in learning and memory retention. *Lymnaea stagnalis* is a pond snail with a simple nervous system and easily observable behaviors, making it an excellent model organism for human neurobiology. In this study, we used *L. stagnalis* to explore the relationship between green tea and a stressor that impairs memory formation to determine the effects of both green tea and stress on the snails' ability to learn, form, and retain memories. Memory was assessed using a conditioning procedure known as conditioned taste aversion (CTA), where snails are exposed to a sweet substance followed by a bitter taste with the number of biting responses being recorded. For the CTA groups, a total of 33 snails in 3 separate cohorts (Control (i.e. no stress), stressed, and stressed with green tea) was used in the trainings. Our results indicated that the best learning and memory occurred in the combination stressed with green tea group, specifically for long-term memory, although snails displayed good learning and memory during the short-term and intermediate trials. Stress was shown to be harmful to snail learning and memory for short-term, intermediate, and long-term memory. Thus, green tea not only alleviated the effects of stress, but also improved the snails' ability to learn and remember compared to their control counterparts (not stressed) group.

INTRODUCTION

In an ever more complex world, people are experiencing increased stress and anxiety. According to a 2017 survey conducted by The National Institute of Mental Health, over 40 million Americans were diagnosed with Generalized Anxiety Disorder (GAD), ranking GAD as 86% of all diagnosed mental health illnesses in the United States (1). The increase in stress and anxiety not only negatively affects adults but also the younger generation. In a 2014 American Psychological Association (APA) survey for stress, teens reported worse mental health and higher levels of anxiety and depression than all other age groups (2). In the annual survey, in 2013 teens first began to report higher levels of stress than adults – a trend that has since continued. In another survey, 61% of teens reported that they feel a lot of pressure to get good grades, 29% feel pressure to look good, 28% feel pressure to fit in socially, and 21% feel pressure to excel in sports (3). The pressures students face today have increased their anxiety levels and could potentially interfere with their ability to learn.

There are several natural remedies used to alleviate stress and anxiety. Green tea, made from the leaves of Camellia sinensis, has been consumed and applauded for its health benefits for thousands of years. It was explicitly used as a medicine during the Tang Dynasty (618-907 AD) in China (4). Recently, green tea was studied for its health benefits including prevention of cardiovascular disease, cancer, and cognitive dysfunction. It was shown that the consumption of green tea improved memory and attention in subjects with mild cognitive impairments (5). In a study at the University of Basel in Switzerland, researchers found that green tea extract enhances cognition in healthy subjects, specifically their working memory (6). Working memory, as defined by British cognitive psychologists Alan D. Baddeley and Graham J. Hitch, refers to "the short-term maintenance and manipulation of information necessary for performing complex cognitive tasks such as learning, reasoning, and comprehension".

Green tea contains flavonoids, a group of plant molecules believed to be responsible for the health benefits through cell signaling pathways and their antioxidant effects. It is made from leaves that have not undergone oxidation and therefore contains more antioxidants than other teas (7). The health benefits of green tea have been mainly attributed to a group of antioxidants called catechins. Catechins have previously been found to help improve memory and learning (8).

The Great Pond Snail, *Lymnaea stagnalis*, is a freshwater gastropod found in the Holarctic region (**Figure 1**). The snail possesses a N-methyl-D-aspartate (NMDA) receptor, which enhances the strength of synaptic connections in the nervous system and plays a vital role in memory and certain kinds of learning; this receptor is also found in the mammalian brain. Strengthening the synaptic connections due to activation of NMDA receptors is critical for learning in the pond snail as well as in humans (9). For this reason, the snail is widely used to research human learning and memory because of the similarity in nervous system structures and processes. Snails are also used because they are easy to train through conditioned learning, have easily observable behaviors linked to memory, and have large neurons. All these factors make the snail an excellent model organism to study neurobiology.

Audesirk et al. concluded that the best way to train *L. stagnalis* was by using Conditioned Taste Aversion (CTA) (10). CTA is an operant conditioning procedure achieved by

exposing an organism to a sweet taste (conditioned stimulus), which evokes a feeding response, followed by a bitter taste (unconditional stimulus), which evokes a withdrawal response. The goal of CTA is to have the organism associate the two tastes, so that when presented with the sweet taste in the future, the snail will avoid it, remembering its training. Retention of a training behavior is considered memory. Short-term memory only lasts minutes, while intermediate memory lasts 1–2 hours, and long-term memory lasts longer than 18 hours.

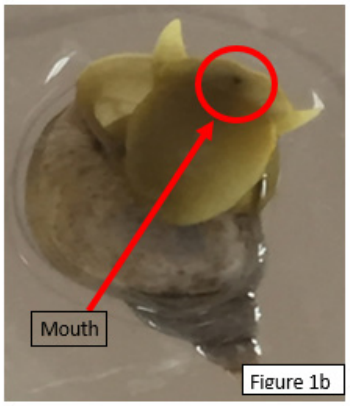

Figure 1: (a) Lymnaea stagnalis is approximately 2 cm in length with a very simple nervous system. (b) The underside of the snail observed by a mirror. The mouth is labeled to indicate how biting is observed to assess learning and memory.

Scientists have tested the effects of several memory-improving flavonoids and other substances to determine which chemical compounds could improve snail memory. A flavonoid called epicatechin, which is found in green tea, cocoa, red wine, and blueberries, was found to help improve memory and learning in *L. stagnalis* (11). The reason this specific flavonoid was studied was because medical researchers had discovered the many health benefits of green tea in humans, such as memory improvement. The beneficial impact on memory that green tea causes is most likely due to the flavonoids and phytochemicals improving the cognitive functions of the nervous system (12). A 2012 study tested the effect of chocolate, known to contain memory-improving flavonoids, on the memory of the snails (13). The results showed that the snails exposed to chocolate demonstrated better learning and memory than those not exposed.

Recent studies have also used pond snails to study stress and anxiety. Understanding how stress and anxiety affects snails may help researchers to better understand green tea's effect on humans. There are several factors that can cause enough stress to impact memory and learning in snails. In one study, scientists exposed snails to the predatory scent of crayfish. After the exposure, snails were unable to learn and form memories (14). A different study found that when pond water was depleted of calcium- essential for shell strength and rebuilding- stressed snails were unable to learn and form memories (15). A quick and simple way to stress snails is by overcrowding 15 to 20 individuals in 100 mL of pond water for 1 hour prior to training. Under these conditions, snails also lose their ability to learn and remember (16, 17). By training snails and observing their behaviors following exposure to stressful situations, it is evident that the stressful event resulted in some impairment of memory or prevented any memories from forming.

The significance behind training these snails and observing their learning and memory patterns is that the results from such studies can be related to human neurology. The purpose of this study was to determine if green tea could improve the memory of the snail, if stress interferes with learning and memory of the snail, and if green tea could alleviate the effects of stress on learning and memory in the snail. We hypothesized that green tea would improve learning and memory, stress would inhibit learning and memory, and green tea would be able to reverse the stress-induced learning and memory deficits in the snails.

RESULTS

In this study, memory was assessed using a conditioning procedure known as conditioned taste aversion (CTA), where snails are exposed to a sweet substance followed by a bitter taste with the number of biting responses being recorded. For the CTA groups, a total of 33 snails in 3 separate cohorts (Control (i.e. no stress), stressed, and stressed with green tea) was used in the trainings. Our results indicated that the best learning and memory occurred in the combination stressed with green tea group, specifically for long-term memory, although snails displayed good learning and memory during the short-term and intermediate trials. Stress was shown to be harmful to snail learning and memory for short-term, intermediate, and long-term memory. Thus, green tea not only alleviated the effects of stress, but also improved the snails' ability to learn and remember compared to their control counterparts (not stressed) group, suggesting green tea is effective in alleviating the effects of stress.

Effect of Green Tea on Learning and Memory

First, we studied the effect of green tea on short-term, intermediate-term, and long-term memory formation in *L. stagnalis*. We trained and compared two groups of 20 snails: one group trained only in pond water and the other group trained in a 1:4 ratio of green tea to pond water. One-way ANOVA analysis indicated for the pond water group that there was no significant difference among the groups ($F_{3,76}$ =

2.27, $p = 0.0877$). The ANOVA results for the green tea group indicated that a post-hoc Tukey Test should be conducted ($F_{3,76} = 76.87$, $p < 0.0001$). The results from the post-hoc Tukey Test indicated that there was significant difference between the pre-test and 10-minute post-test ($p = 0.001$), the pre-test and 1 hour post-test ($p = 0.001$), and the pretest and 24 hour post-test ($p = 0.001$). We defined good learning and memory as the snails taking less bites during the post-test than the pre-test. We defined poor learning and memory as snails who experienced no change or an increase in number of bites. We found that 80% of the snails trained in pond water displayed good short-term (ST) memory, 55% displayed good intermediate (IM) memory, and only 45% displayed good long-term (LT) memory. We found that 100% of the snails trained in green tea displayed good ST memory, IM memory, LT memory **(Figure 2)**.

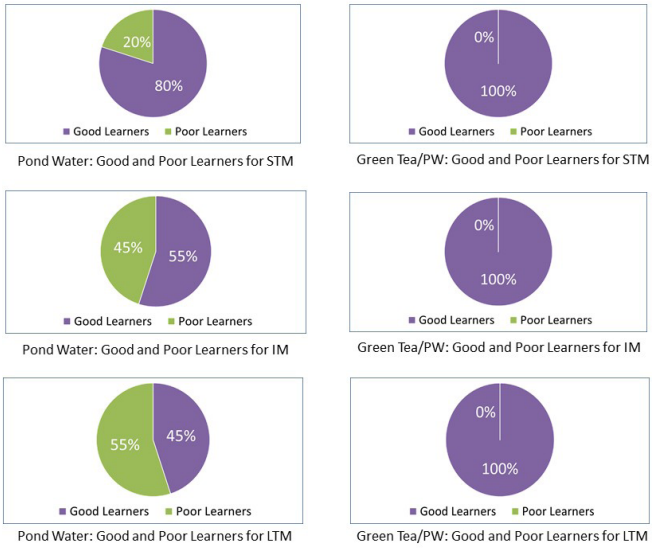

Figure 2: Effect of Green Tea on Learning and Memory. Percent of Good vs. Poor Learners of snail CTA training in pond water and pond water/green tea. The number of bites post CTA training for each snail group (n=15) was used to determine percent of good learners (snails that retained memory/showed a decrease in number of bites) and percent of poor learners (snails that didn't retain memory/showed an increase or no change in number of bites). All snails trained in pond water/green tea learned and retained the CTA training memory.

Effect of Stress and Stress with Green Tea on Learning and Memory

The mean number of bites for each test group was measured as a readout for stress **(Figure 3).** When the snails were first trained in pond water, most of them displayed good ST memory, but not LT **(Figure 3)**, which was expected since *L. stagnalis* does not naturally have good LT memory (15). However, after being stressed, most snails were not able to remember the training at all and took many bites during post-tests. The stressed snails exposed to green tea showed improved ST, IM, and LT memory, taking very few bites of sucrose in one minute.

Green Tea and Stress without CTA training

We conducted a one-way ANOVA on the number of bites in each trial for both the green tea group without CTA training and stress group without CTA training data. The ANOVA results for the green tea group indicate that there was no significant difference among the groups ($F_{3,56} = 0.717$, $p = 0.546$). The ANOVA results for the stress group indicated that there was no significant difference among the groups ($F_{3,56} = 0.698$, $p = 0.557$). The results from the green tea test and stress test indicate that neither green tea nor stress had a significant effect on the feeding response of the snails.

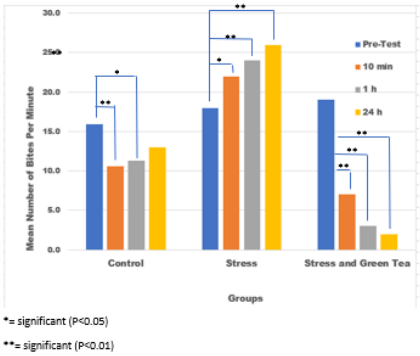

Figure 3: Effect of stress and stress with green tea on learning and memory. Mean number of bites for each group. Each cluster of bars represent a treatment group (n=33), while the smaller bars represent the individual trial [blue: pre-test, orange: 10 min (ST memory), grey: 1 h (IM memory), yellow: 24 h (LT memory)]. Asterisks highlight where the differences lied among the groups according to the Tukey Tests. These results show that stress negatively effected snail memory

Pond Water CTA results

We conducted a one-way ANOVA on the number of bites in the four trials in the pond water group **(Table 1).** The ANOVA results for the group indicated that there was no significant difference among the groups ($F_{3,128} = 4.57$, $p = 0.0045$). In the pond water trials, there was a significant decrease in the number of bites for the 10-minute post-test as compared to the pre-test ($p < 0.01$, **Table 2**), indicating that these snails displayed excellent short-term memory. They retained that memory for the 1-hour post-test ($p < 0.05$, **Table 2)**, but displayed an increase in the number of bites during the 24-hour post-test, indicating a gradual loss of memory **(Figure 3)**. Seventy-six percent of the snails displayed good ST memory, sixty-nine percent displayed good IM memory, and only fifty-five percent displayed good LT memory.

Group	p-value	F-value
Pond Water	0.0045	F(3,128) = 4.57
Stress	9.50E-07	F(3,128) = 11.55
Stress and Tea	1.11E-16	F(3,128) = 122.24

Table1: ANOVA *p*-values and *f*-values. One-way ANOVA test results comparing the pond water, stressed, and combination stress with green tea water groups. The results indicate that a significant difference exists within each of the three groups.

Stress CTA results

We conducted a one-way ANOVA on the CTA training with stress group **(Table 1)**. The ANOVA results for the data indicated that there was a significant difference among the groups and that a post-hoc Tukey Test should be conducted ($F_{3,128}$ = 11.55, p < 0.0001). The results from the post-hoc Tukey Test **(Table 2)** indicated that there was significant difference between the pre-test and 10-minute post-test (p = 0.05), between the pre-test and 1-hour post-test (p = 0.001), and between the pre-test and 24-hour post-test (p = 0.001). Eighteen percent of the snails displayed good ST memory, eighteen percent of the snails displayed good IM memory, and only three percent of the snails displayed good LT memory. Stress was detrimental to the snails' learning and memory, as the mean number of bites post-training showed a statistically significant increase **(Figure 3)**.

Comparison	Pond Water	Stress	Green Tea
Pre-Test vs 10 min	0.0051**	0.0143*	0.0010**
Pre-Test vs 1 h	0.0190*	0.0010**	0.0010**
Pre-Test vs 24 h	0.2556 (ns)	0.0010**	0.0010**
10 min vs 1 h	0.0899 (ns)	0.6938 (ns)	0.0034 (ns)
10 vs 24 h	0.4196 (ns)	0.0456*	0.0010**
1 h vs 24 h	0.6637 (ns)	0.3929 (ns)	0.6688 (ns)

Table 2: Tukey Pairwise Comparisons. Tukey Test results comparing the pond water, stressed, and combination stress with green tea water groups. We used Post-hoc Tukey Test results to generate pairwise comparisons to determine the significant differences in the trials. *= p<0.05; **= p<0.01; ns= nonsignificant.

Green Tea/Stress CTA results

We conducted a one-way ANOVA on the number of bites in green tea post stress group. The ANOVA results for the data indicated that there was a significant difference among the groups and that a post-hoc Tukey Test should be conducted ($F_{3,128}$ = 122.24, p < 0.0001). The results from the post-hoc Tukey Test indicated that there was significant difference between the number of bites taken pre-test and 10-minute post-test (p = 0.001), the pre-test and 1-hour post-test (p = 0.001), and the pre-test and 24-hour post-test (p = 0.001). Ninety-seven percent of the snails displayed good ST memory, ninety-seven percent of the snails displayed good IM memory, and one-hundred percent of the snails displayed good LT memory. The mean number of bites post training had a statistically significant decrease indicating that the training was successful **(Figure 3)**.

DISCUSSION

The recent increase in stress and anxiety levels and our attempts to alleviate and remedy with the use of ancient holistic herbs and medicines, such as green tea, led us to investigate whether green tea can alleviate the negative impact stress has on learning and memory formation. The simple nervous system of *L. stagnalis*, combined with the ease of training and observing learned behaviors, make *L. stagnalis* an excellent model organism to study neurobiology. The purpose of this study was to determine if green tea could improve the memory of the snail, if stress interferes with learning and memory of the snail, and if green tea could alleviate the effects of stress on learning and memory in the snail.

From the results of our first experiment examining the effect of green tea on memory and learning, we concluded that green tea was effective in enhancing learning and memory formation in *L. stagnalis*. Once that was determined, our second experiment examined if green tea would be able to reverse the effects of stress on learning and memory. Before any CTA training, the effects stress and green tea would have on the snails' appetite needed to be determined. The stress and green tea controls were conducted to ensure two factors — that green tea did not act as an appetite suppressant and that exposure to stress did not cause the snails to 'stress-eat'. The stress and green tea controls indicated that there was no measurable effect of green tea or stress on snail appetite. The results here indicate that green tea significantly improved the snails' ability to retain training. Therefore, the main goal was to determine how stress would impact learning and memory and if green tea would be able to alleviate the effects of stress. The pond water group in our second experiment confirmed that the one-trial training was effective, and the snails could be conditioned. The goal of the stress CTA trials was to confirm that stress would affect the snails' ability to learn and remember the CTA. Since the snails displayed an increase in number of bites post-training, stress appeared to have interfered with the snails' ability to learn and remember. The results of the stressed snails exposed to green tea indicate that green tea was able to alleviate the effects of stress and reverse the stress-imposed learning/memory deficit in the snails. All the snails were good learners in the stress with green tea trials with the greatest improvement in their long-term memory. These results indicate that green tea can reverse the effects of stress on learning and memory. To counter the effects of stress, consumption of green tea could reverse stress-induced learning or memory deficits.

The data supports the hypothesis that not only does green tea improve learning and memory, but it can also alleviate the detrimental effects of stress on learning and memory in *L. stagnalis*. The greatest improvement, however, was seen in the long-term memory, suggesting that green tea has the strongest effects on long-term memory. Since the neurobehavioral processes in *L. stagnalis* have been shown to be like those in humans (10), the conclusions from our research can be applied to human neurology. Green tea may have the greatest effects on human long-term memory instead of short-term. In this study, stress was shown to negatively impact learning and memory in *L. stagnalis*, while green tea seemed to reverse that effect and aid in learning and memory. Since *L. stagnalis* is widely used in neuroscience research, we believe that they can be especially helpful in research on learning and memory formation.

Besides the green tea, stress also played a major factor

in the findings of this study. Stress caused the snails to take a dramatic increase in the number of bites and a high percentage of stressed snails were poor learners, as they showed an increase in number of bite post-training. Stress was detrimental to the snails' learning and memory. This supports the theories that stress is very harmful to human learning and memory. High stress levels in adolescents have a direct correlation with lower grades and poor learning and memory, so much so that it can lead to memory and learning deficits if stress levels are kept high (3). To decrease stress levels and reverse the learning/memory deficit, green tea was extremely effective. Green tea is a natural way to reduce stress levels and prevent deficits. A natural way to improve memory has been something scientists have been searching for and based on our results green tea shows the ability to increase learning and memory in snails under stress.

MATERIALS AND METHODS

Care and Maintenance of *L. stagnalis*

L. stagnalis snails (obtained from Patsy Dickinson and Stephan Hauptman, Bowdoin College) were kept in a 10-gallon tank; with 50% of the water being Poland Springs water and 50% pond water (1.8 g of Instant Ocean/1 gallon of deionized water). The water was replaced every week and the waste was taken out of the tank every other day. Snails were fed organic romaine lettuce three times a week. The tank temperature was maintained between 18° and 22°C. To maintain calcium levels, oyster shells were crushed and added to the water. The average size of the snails was 2 cm. The age of the snails cannot be determined due to varying lab conditions affecting the rate of growth.

Conditioned Taste Aversion (CTA)

Snails were deprived of food for 24 hours prior to training. This was important because during training, the number of bites the snail took was being measured, so food deprivation ensured that the snails were hungry and would take bites of the solution. As it is known that *L. stagnalis* feeding behaviors undergo both appetitive and aversive classical conditioning (10), the number of bites taken per minute was chosen as an indicator of memory formation.

The first step of CTA was the pre-test. During the pre-test, the snail was placed in a petri dish elevated above a mirror (used to observe the snail bites). Next, the snail was exposed to 5 mL of a 0.5% sucrose solution. A timer was set for one minute, and the number of bites of sucrose the snail took was recorded. Counting the number of bites is an easily observable technique used in previous studies (16). The contents of the dish were then emptied, and the pond water was replenished **(Figure 4)**.

Ten minutes after the pre-test, the snail was exposed to the sucrose solution again for only 15 seconds. After the 15 seconds, the contents of the dish were emptied, and the pond water was replenished. Five seconds later, the snail was exposed to 5 mL of a 0.5 % bitter KCl solution. The KCl was left in the petri dish for 15 seconds, then the contents of the dish were emptied, and the pond water was replenished.

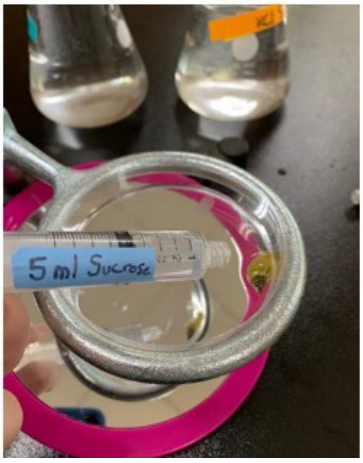

Figure 4: CTA used for all experiments. The conditioned taste aversion procedure (first step). The snail was given 5 mL of a 0.5% sucrose solution (conditional stimulus; shown) followed by 5 mL of a 0.5% KCl solution (unconditional stimulus; not shown). If snails demonstrated good learning, they would avoid biting the sucrose. However, if the snails were poor learners, they would not show any aversion to the sucrose.

Ten minutes later, the first post-test was conducted. The procedure of the post-test was identical to that of the pre-test. For the 10-minute post-test, the snail was exposed to the 5 mL of sucrose solution again. A timer was set for one minute and the number of bites was observed and recorded using a mirror. Two more post-tests were conducted to reach a total of three post-tests per snail. The three post-tests were conducted 10 minutes, 1 hour, and 24 hours after conditioning.

Green Tea Control and Green Tea CTA

In order to ensure that the green tea had no effect on the snails' appetite, 15 snails were deprived of food for 24 hours and then exposed to 5 mL of 0.5% sucrose solution. A timer was set for one minute, and the number of bites of sucrose the snail took was recorded. Then, the contents of the dish were emptied, and the pond water was replenished.

The snails were then placed in a 1:4 dilution of green tea to pond water and once again exposed to 5 mL sucrose solution with the number of bites taken recorded for 1 minute. This was followed by the 10-minute, 1-hour, and 24-hour post-tests. This specific concentration of green tea was previously used and found to be effective (14).

Thirty-three snails underwent CTA training in green tea to determine the effect of green tea on memory and learning. The CTA in green tea training followed the same procedure as above, apart from the snails being placed in a 1:4 dilution of green tea to pond water during the training. Lipton decaffeinated green tea was used to ensure that the caffeine itself did not affect the snails' appetite. There is no evidence that the other components of green tea affect appetite.

Stress Control and Stress CTA Procedure

To determine if stress influenced the snails' appetite, 15 snails were exposed to 5 mL of 0.5% sucrose solution. A timer was set for one minute and the number of bites of sucrose the snail took was recorded, then the contents of the dish were emptied, and the pond water was replenished. The snails were then stressed by crowding 15–20 snails in 100 mL of pond water for 1 hour **(Figure 5)** and then once again exposed to 5 mL of 0.5% sucrose solution with the number of bites taken recorded for 1 minute.

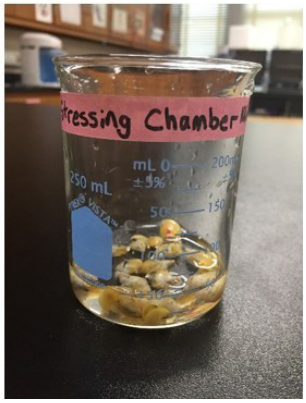

Figure 5: Stressing Chamber used for all experiments. Snails were stressed prior to training by overcrowding 20 snails in a beaker with only 100 mL of pond water for 1 hour.

Prior to any further tests, in order to ensure that the snails used in the trials did not retain any memory of a previous CTA training, the snail's memory was assessed in a pre-test in addition to allowing 3–5 days to pass before any additional trials. If a snail had a lower number of bites/minute as compared to previous pre-test results, then they would not be used that day. After the pre-test, the snails were stressed. To stress the snails, 15– 20 of them were crowded in 100 mL of pond water in a beaker for 1 hour **(Figure 5).** After stressing for one hour, the snails were trained using the CTA procedure, omitting the pre-test, since it was conducted prior to stressing the snails. Once again, post-tests were conducted 10 minutes, 1 hour, and 24 hours after conditioning.

Stress and Green Tea Procedure

After the snails were no longer stressed and forgot their conditioning once more (3–5 days later), they were given another pre-test. This pre-test was crucial since it once again evaluated if the snails had forgotten their training or not. Snails that had not forgotten previous training were placed back into their tank and another snail was chosen. Ten minutes after the pre-test, the snails were stressed using the stressing procedure above. After being stressed, the snails were trained using the CTA procedure, but instead of being trained in pond water, they were trained in a 1:4 dilution of green tea to pond water. After being trained in the green tea, the normal post-tests followed. Between 15–20 snails had to be in the stressing chamber to induce stress by crowding. Since 20 snails could not be trained all at once, some snails were used as placeholders.

Statistical Analysis

Data are expressed as the mean number of bites per minute. Statistical significance ($p < 0.05$) was determined using a one-way analysis of variance test (ANOVA) to determine if there was a significant difference the two treatment groups and the control group. Once it was determined that there was a significant difference, a Tukey Pairwise Comparison was used to determine where the differences lie among the groups.

ACKNOWLEDGEMENTS

We would like to thank Mary Simons, Richard Kurtz, Dr. Ken Lukowiak, and the JEI editors for their mentorship and guidance through the duration of this process. Their contributions were greatly appreciated.

Received: August 21, 2020
Accepted: November 5, 2020
Published: January 30, 2021

REFERENCES

1. "Mental Illness." *The National Institute of Mental Health*, 2017. nimh.nih.gov/health/statistics/mental-illness.shtml
2. Bethune, S. "Teen Stress Rivals That of Adults." *American Psychological Association,* vol. 4, no. 4, 2014. doi: 10.1037/e508692014-007.
3. Graf, N. and Horowitz, J. "Most U.S. teens see anxiety and depression as a major problem among their peers." *Pew Research Center*, 2019. www.pewsocialtrends.org/2019/02/20/most-u-s-teens-see-anxiety-and-depression-as-a-major-problem-among-their-peers/
4. Yang, Chung S., et al. "Recent Scientific Studies of a Traditional Chinese Medicine, Tea, on Prevention of Chronic Diseases." *Journal of Traditional and Complementary Medicine*, vol. 4, no. 1, 2014, pp. 17–23., doi:10.4103/2225-4110.124326.
5. Deka, A. and Vita, J. "Tea and cardiovascular disease." *Pharmacological Research*, 2011. doi: 10.1016/j.phrs.2011.03.009
6. Schmidt, A., et al. "Green tea extract enhances parieto-frontal connectivity during working memory processing." *Psychopharmacology*, 2014. doi: 10.1007/s00213-014-3526-1
7. "What are the health benefits of green tea?" Medical News Today, 2017.
8. Gottumukkala, R., Nadimpalli, N., Sukala, K., Subbaraju, G. "Determination of catechin and epicatechin content in chocolates by high-performance liquid chromatography." *International Scholarly Research Notices*, 2014. doi: 10.1155/2014/628196
9. Mayford, M., Siegelbaum, S., Kandel, E. "Synapses and

memory storage." *Cold Spring Harbor Perspectives in Biology,* 2012. doi: 10.1101/cshperspect.a005751
10. Audesirk, G., Audesirk, T., Alexander, J. "One-trial reward learning in the snail *Lymnaea stagnalis*." *The Journal of Neurobiology*, vol. 15, 1984, pp. 67-72. doi: 10.1002/neu.480150107
11. Knezevic, B., Kotamatsuzaki, Y., Freitas, E., Lukowiak, K. "A flavonoid component of chocolate quickly reverses an imposed memory deficit." *The Company of Biologists*, vol. 219, 2016, pp. 816-823. doi: 10.1242/jeb.130765
12. Whiteman, H. "Green tea may boost working memory." *Medical News Today*, 2017
13. Fruson, L., Dalesman, S., Lukowiak, K. "A flavanol present in cocoa [(-)epicatechin] enhances snail memory." *The Journal of Experimental Biology*, vol 215, 2012, pp. 3566-3576. doi: 10.12421/jeb.070300
14. Hughes, E., Shymansky, T., Swinton, E., Lukowiak, K., Swinton, C., Sunada, H., et al. "Strain-specific differences of the effects of stress on memory in *Lymnaea*." *The Company of Biologists*, vol. 220, 2017, pp. 891-899. doi: 10.1242/jeb.149161
15. Lukowiak, K., Sunada, H., Teskey, M., Dalesman, S. "Environmentally relevant stressors alter memory formation in the pond snail *Lymnaea*." *The Journal of Experimental Biology,* vol. 217, 2014, pp. 76-83. doi: 10.1242/jeb.089441
16. Dalesman, S. and Lukowiak, K. "How stress alters memory in 'smart' snails" PLoS ONE, 2012. doi:10.1371/journal.pone.0032334
17. Dalesman, S. and Sunada, H. "Combining stressors that individually impede long-term memory." *PLoS ONE*, vol. 8, 2013. doi: 10.1371/journal.pone.0079561

Sponsorship

Editor's Circle $10,000+

ALLOY THERAPEUTICS

Patron $5,000+

NEW ENGLAND BioLabs® Inc.
enabling technologies in the life sciences

PORTFOLIOS WITH PURPOSE®

Institutional Supporters

HARVARD UNIVERSITY

HARVARD MEDICAL SCHOOL

Tufts UNIVERSITY

Charitable Contributions

We need your help to provide mentorship to young scientists everywhere.

JEI is supported by an entirely volunteer staff, and over 90% of our funds go towards providing educational experiences for students. Our costs include manuscript management fees, web hosting, creation of STEM education resources for teachers, and local outreach programs at our affiliate universities. We provide these services to students and teachers entirely free of any cost, and rely on generous benefactors to support our programs.

A donation of $30 will sponsor one student's scientific mentorship, peer review and publication, a six month scientific experience that in one student's words, 're-energized my curiosity towards science', and 'gave me confidence that I could take an idea I had and turn it into something that I could put out into the world'. **If you would like to donate to JEI, please visit https://emerginginvestigators.org/support, or contact us at questions@emerginginvestigators.org.** Thank you for supporting the next generation of scientists!

'Journal of Emerging Investigators, Inc. is a Section 501(c)(3) public charity organization (EIN: 45-2206379). Your donation to JEI is tax-deductible. '

emerginginvestigators.org